Structure Formation of Polymeric Building Blocks: Complex Polymer Architectures

Kurt Binder, Hans-Jürgen Butt, George Floudas, Holger Frey, Hsiao-Ping Hsu, Katharina Landfester, Ute Kolb, Angelika Kühnle, Michael Maskos, Klaus Müllen, Wolfgang Paul, Manfred Schmidt, Hans Wolfgang Spiess, and Peter Virnau

Abstract This chapter describes macromolecules with a complex structure, their defined aggregation in solution, their adsorption to surfaces, and their possible aggregation on surfaces. The term "complex structure" implies that the macromolecules show different, distinct structural elements or building blocks on a supra-atomic length scale. Key to understanding the complex structure of macromolecules, their aggregation, and adsorption to surfaces are intra- and intermolecular interactions such as van der Waals, electrostatic, π–π interactions, and hydrogen bonds.

Keywords Biopolymers · Conformation · Copolymers · Cylindrical brush · Dendrimer · Liquid crystal · NMR spectroscopy · Organic electronics · Polyelectrolyte · Polymer · Self-assembly

K. Binder, H.-P. Hsu, and P. Virnau
Institute of Physics, Johannes Gutenberg University, Mainz 55099, Germany

H.-J. Butt (✉), K. Landfester, K. Müllen, and H.W. Spiess
Max Planck Institute for Polymer Research, Ackermannweg 10, Mainz 55128, Germany
e-mail: butt@mpip-mainz.mpg.de

G. Floudas
Department of Physics, University of Ioannina, Ioannina 45110, Greece

H. Frey
Institute of Organic Chemistry, Johannes Gutenberg University, Mainz 55099, Germany

U. Kolb, A. Kühnle, and M. Schmidt
Institute for Physical Chemistry, Johannes Gutenberg University, Mainz 55099, Germany

M. Maskos
Institute for Physical Chemistry, Johannes Gutenberg University, Mainz 55099, Germany

Institut für Mikrotechnik Mainz IMM, Carl-Zeiss-Strasse 18-20, Mainz 55129, Germany

W. Paul
Institute for Physics, Martin Luther Universität, Halle 06120, Germany

Contents

Abbreviations

α	Degree of dissociation
δ	Shell thickness of nanocapsule
ε	Energy of interaction between monomers
λ	Wave length
η	Viscosity
ν	Exponent characterizing end-to-end distance

ρ	Density of polymers or particles in solution
σ	Grafting density of side chains to backbone
χ	Flory–Huggins interaction parameter
λ_B	Bjerrum length
σ_{calc}	Calculated conductivity
σ_{DC}	DC-conductivity of an ion-containing medium
σ_{exp}	Measured DC-conductivity
D_+, D_-	Calculated diffusion coefficient of the free cation/anion
D_+^{exp}, D_-^{exp}	Diffusion coefficient as measured by NMR
$<z_b>$	Average distance of a backbone monomer of an adsorbed bottle brush from the surface
AFM	Atomic force microscopy
$\vec{l}_s$	Bond vectors are grafted to the backbone
BPCPPCA	2-(4-Bromophenyl)-6-(4-chlorophenyl)pyridine-4-carboxylic acid
BPDCA	Biphenyl-4,4′-dicarboxylic acid
BTA	Benzene-1,3,5-tricarboxamides
d	Exponent describing kinetics of aggregation
D	Diameter of drop
D_0	Diffusion coefficient of the neutral complex
DCBA	2,5-Dichloro benzoic acid
DEER	Double electron–electron resonance
D_{exp}	Experimental diffusion coefficient
DIBA	2,5-Diiodo benzoic acid
DISA	3,5-Diiodo salicylic acid
DLS	Dynamic light scattering
DMF	N,N-Dimethylformamide
DQNMR	Double-quantum nuclear magnetic resonance spectroscopy
DS	Dielectric spectroscopy
DSC	Differential scanning calorimetry
$\vec{e}$	Elementary charge
$\vec{R}_{e,b}$	End-to-end vector of the backbone
$\vec{R}_e$	End-to-end vector of side chain
$\vec{l}_b$	Effective bond vectors of main chain
E_C	Coulomb attractive energy
EPR	Electron paramagnetic resonance
E_σ	Activation energy for ion transport
FCS	Fluorescence correlation spectroscopy
HBC	Hexa-peri-hexabenzocoronenes
I	Scattering intensity
IBA	4-Iodo benzoic acid
k_B	Boltzmann constant
L	Contour length
L_0	Thickness of block copolymer lamellar
LC	Liquid crystalline

l_d	Domain size
LED	Light emitting diode
l_k	Kuhn length
l_m	Length per repeat unit of the main chain
l_p	Persistence length
M_0	Molar mass of one repeat unit in the main chain
MAO	Methylaluminoxanes
MAS	Magic angle spinning
MFA	Methyl formamide
M_L	Molar mass per length of main chain
M_n^{sc}	Number-average side chain molar mass
M^{sc}	Side chain molar mass
N	Degree of polymerization
N_b	Number of effective monomers in main chain
NICS	Nucleus independent chemical shift
NMR	Nuclear magnetic resonance
NOE	Nuclear Overhauser effect
N_s	Number of effective monomers in side chain
OPBA	Oligo(p-benzamides)
P	Main chain degree of polymerization
PAH	Polycyclic aromatic hydrocarbons
PAMAM	Poly(amido amine)
PBI	Perylene bisdiimide
PBLG	Poly(γ-benzyl-L-glutamate)
PDI	Perylene diimide
PEG	Poly(ethylene glycol)
PEI	Poly(ethylene imine)
PEO	Poly(ethylene oxide)
p_i	Number density of the ith type of charge carrier
PLL	Poly-L-lysine
PLP	Poly(L-proline)
PMA	Polymethacrylate
PMMA	Poly(methyl methacrylate)
PPD	Polyphenylene dendrimer
p_s	Total ion concentration
PS	Polystyrene
P_{sc}	Side chain degree of polymerization
PSS	Poly(styrene sulfonate)
PVP	Poly-2-vinylpyridinium
P_w	Weight average degree of polymerization
q	Scattering vector
QD	Quantum dot
q_i	Charge of the ith type of charge carrier
r_c	Distance separating a point-like cation from a point-like anion

R_c	Core radius of a spherical brush
R_{cs}	Cross-sectional radius
R_g	Radius of gyration
R_{gc}	Cross-sectional radius of gyration of brush polymer
R_h	Hydrodynamic radius
S	Dynamic order parameter
s	Number of bonds along the backbone
SANS	Small angle neutron scattering
SAXS	Small-angle X-ray scattering
s_{blob}	Number of monomers per blob
SDS	Sodium dodecyl sulfate
SLS	Static light scattering
T	Temperature
t	Time
TBA^+	Tetrabutylammonium cation
TEM	Transmission electron microscopy
T_g	Glass transition temperature
THF	Tetrahydrofuran
T_Θ	Theta temperature
$W(r)$	Potential of mean force for two particles at distance r
WAXS	Wide-angle X-ray scattering
x_{anion}	Mole fraction of anionic charges
XPS	X-ray photoelectron spectroscopy
Z^+/Z^-	Charge ratio
ε_0	Permittivity of free space
ε_r	Dielectric permittivity
μ_i	Mobility of the ith type of charge carrier
σ_0	Limiting conductivity

1 Introduction

This chapter is organized according to the complexity of structure formation (Fig. 1) and along the dominating interactions. First we focus on van der Waals attraction, electrostatic interactions, and possible phase separations. They depend on distance but are not specifically oriented. When hydrogen bonds or π–π interactions come into play, more complex macromolecular architectures are formed due to the directionality. Although phase separations are often driven by interactions including H-bonds (e.g., the phase separation between water and hydrocarbons), we have included them in the first part because the resulting supramolecular structures are not dominated by the orientation of the H-bonds. As a further "interaction" we include geometrical constraints. In the simplest case, such a constraint is formed by the adsorbing surface. As a real volumetric constraint we include the confinement of block copolymers to small spherical drops.

Fig. 1 Overview of the topics in this chapter

(A) Comlex macro-molecules

(B) Aggregation in solution

(C) Adsorption

(D) Aggregation on surfaces
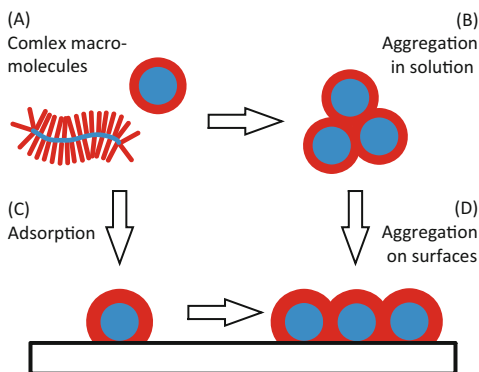
We start with two examples: polyphenylene dendrimers (PPDs) and linear brush polymers. Dendrimers (Sect. 2) are three-dimensional, mostly spherical macromolecules that are built around a core with multiple branching points. Among this intensively studied class of polymers, PPDs are distinguished because they are shape-persistent due to the stiffness of the polyphenylene arms and their steric interactions. Herein, PPDs with widely different functions, caused by different chemical groups at their surface, in their scaffold, and in their core, are described. Since PPDs are perfectly monodisperse and possess a defined shape, they are ideal for addressing fundamental questions of polymer science. One example is the charging of PPDs in organic liquids. Embedding an ionic core in a nonpolar PPD shell immediately highlights the dissociation of ion pairs in nonpolar liquids: how does the degree of dissociation depend on the size of the ions and the dielectric permittivity of the solvent? As examples for functionality, two classes of PPDs are described: first, PPDs as light harvesting, light-emitting, and photoswitchable multichromophores and second, by designing the interior and surface solution properties, PPDs as hosts for specific molecules and as carriers and for drug transport.

As a second example cylindrical brush polymers, often called bottle brushes, are described (Sect. 3). Cylindrical brush polymers usually consist of a flexible main chain, densely grafted by flexible, stiff or dendritically branched side chains. The latter are known as dendronized polymers and have been frequently investigated by both theory and experiment. In the present review, we focus on brush polymers with linear side chains.

The main conformation of cylindrical brush polymers is governed by two opposing forces: The steric repulsion of the densely grafted side chains leads to stretching of the side chains and of the main chain, whereas the entropy elasticity causes both main and side chains to adopt a coiled conformation. Thus, the shape of cylindrical brush polymers emerges from a subtle balance of repulsive and entropic forces. In more detail, the directional persistence of the main chain is primarily governed by the grafting density, the length and the solvent quality of the side chains, as well as by the electrostatic interaction in the case of charged side chains. Bottle brushes have been analyzed experimentally, theoretically, and by simulations.

More specific and oriented interactions, such as hydrogen bonds and shape-dependent π–π interactions offer the possibility to control supramolecular

organization in a much more defined way. This is exemplified in Sect. 4. In fact, the same interactions that dominate the shape of complex macromolecules are also responsible for the formation of defined aggregates and for the adsorption to surfaces. They govern self-assembly at the two levels: the internal structure of the building blocks and the self-assembly of the building blocks. In a simplified manner, the first role can be viewed as "intramolecular" and the second role as "intermolecular". These intra- and intermolecular roles of different interactions are discussed for all types of macromolecules.

Another type of "interaction" is confinement. We focus on the confinement of block copolymers and the resulting microphase separation. As one example, the structure of polystyrene-*block*-poly(methyl methacrylate) (PS-*b*-PMMA) in the confinement of droplets in miniemulsions is described. To better understand microphase separation, experimental results are compared to self-consistent field theory simulations. Then, we consider block copolymers bound to a solid surfaces and their response to different environmental conditions (Sect. 5). As a third example of structures and confinement, the incorporation of quantum dots into the hydrophobic region of polymersomes is demonstrated.

In the last section (Sect. 6) we focus on molecules adsorbed to surfaces. Creating complex polymer architectures on surfaces is important for applications such as (bio)sensors and molecular electronics. However, molecular self-assembly usually relies on weak, reversible interactions leading to inherently fragile structures. To provide stability as well as enhanced electron transport properties we explore the possibility of creating covalently linked molecular structures on bulk insulator surfaces.

In order to better understand the structure and dynamics of polymers, the formation of complex architectures, and to further improve the function of a specific material, a whole range of complementary characterization techniques was required. For example, complex formation of polyelectrolytes has been studied intensely with light and small angle neutron scattering (SANS). Techniques were not only applied but also improved and new techniques have been developed. One example is solid-state NMR. NMR not only yields information on the atomic structure but also provides dynamic information. Typically, NMR results are complemented by wide and small angle X-ray scattering (WAXS and SAXS, respectively) and computer simulations. Another example is high-resolution atomic force microscopy (AFM). In recent years non-contact AFM has been developed, which allows imaging of crystalline structures and defects at the atomic level. So far, however, most studies have been limited to comparatively small organic molecules deposited under well-controlled ultrahigh vacuum conditions. Therefore, the technique is constantly being further developed to extend it to "soft" organic materials and to "real" environments such as in liquids.

Fig. 2 Representation of
polyphenylene dendrimers
(PPDs) with functional
groups in the core, scaffold,
and on the rim
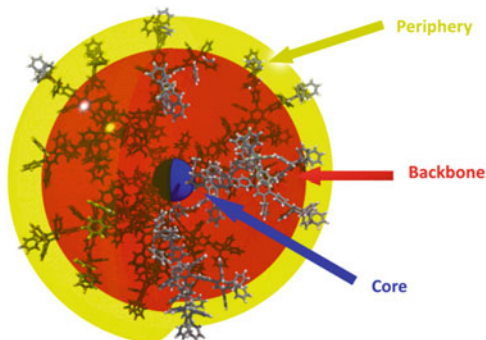
2 Polyphenylene Dendrimers

2.1 Introduction

One of the key features in the synthesis of semirigid macromolecules such as dendrimers is to keep the entropy price low in all kinds of hierarchical structure formation. Dendrimers as unique macromolecules with three-dimensional (3D) shape have found multiple applications [1]. However, in spite of their multi-functional character and their remarkable aesthetic appeal [2], there remain conceptual and experimental problems: How perfectly can they be synthesized [3, 4] and are they really spherical? Many dendrimers described in the literature are not shape-persistent because they are made from conformationally flexible building blocks [5, 6]. They change their shape under the influence of external forces or the prevailing environment. Polyphenylene dendrimers (PPDs) [7–9] introduced here adopt a special role because they (1) possess a high degree of structural perfection, (2) are extremely stable even under harsh conditions, and (3) determine a perfect nanosite definition for active groups either in the core, in the scaffold, or on the rim (Fig. 2) [10]. Examples of such active groups are chromophores, catalysts, and electrolyte functions.

The design principle for PPDs is the build-up from twisted, tightly packed benzene rings. Slight liberation of these rings causes some entropy gain upon solvation, so that the dendrimers become soluble. Solubility can even increase from generation to generation. On the other hand, the phenylene arms of the dendrons cannot undergo back-bending. This is what makes these 3D objects shape-persistent [11].
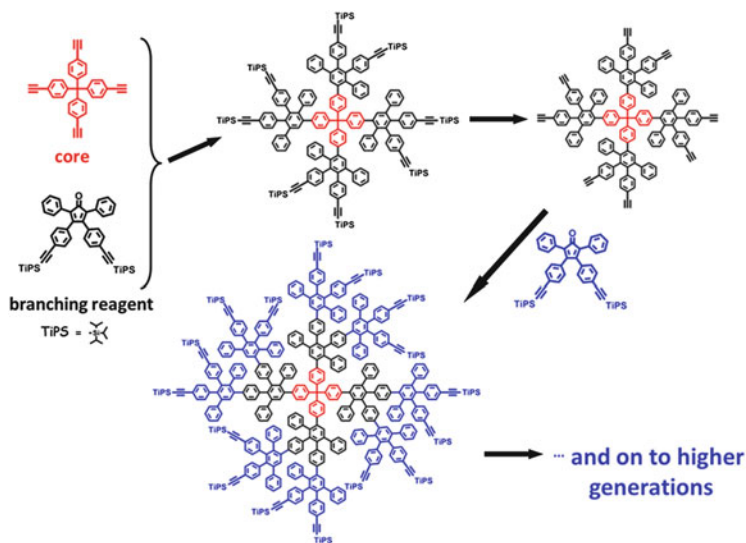
Fig. 3 Synthesis of PPDs via the divergent route using a protected AB2-branching segment and a tetraphenyl methane core

2.2 Synthesis of PPDs

We have succeeded in divergent growth [12] from generation to generation up to nine generations (G9) [13, 14]. The synthetic breakthrough depended upon the use of AB2 and AB4 branching reagents, which comprise both a diene and two or four, respectively, ethinyls as dienophile units for repetitive Diels–Alder cycloaddition (Fig. 3). The dienophiles are blocked by attachment of bulky tri-isopropylsilyl groups [15].

Thus, when the branching reagents are heated together with any multi-ethinyl-substituted core molecule, cycloaddition upon extrusion of carbon monoxide occurs and pentaphenyl benzene moieties are formed. The number of surface ethinyl functions is thus doubled when going to the next generation with the branching reagent. It is the use of multiple irreversible Diels–Alder reactions that leads to a high degree of structural perfection in dendrimer synthesis, a structural perfection so far not reached by other dendrimers. We have verified the structural perfection of PPDs with molecular weights of 1.8 MDa and diameters in excess of 30 nm (Fig. 4). Gel permeation chromatography (GPC), mass spectrometry (MS), and NMR spectroscopy are combined to give a unified view of polymer characterization. Apart from this synthetic achievement, and the importance of this work for precision polymer synthesis in general, there is the additional opportunity of functionalizing the PPDs either inside or outside. The perfect nanosite definition mentioned above proves its value upon incorporation of different functions [7].
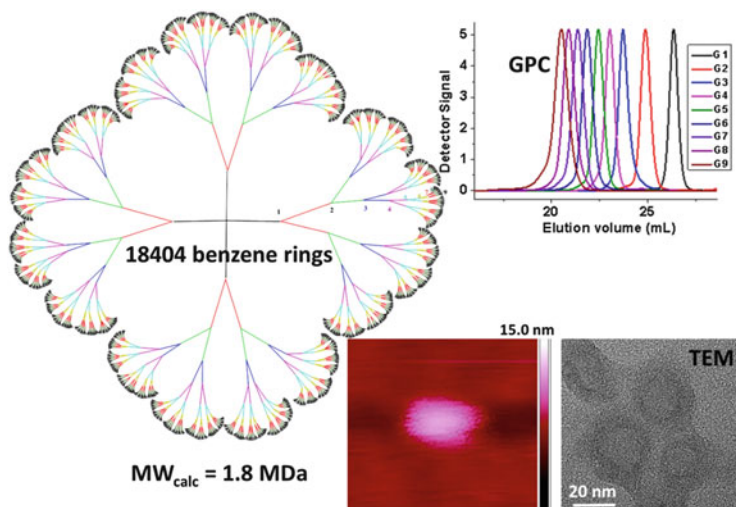
Fig. 4 Structure, GPC chromatograms, and AFM and TEM images of the G9 PPD

2.3 Dissociation of Charged PPDs and Ion Transport

What is particularly challenging and what also defines a tight connection with bottle brush polymers is the incorporation of electrolyte functions. Loading charges on the surface of the dendrimer, e.g., via sulfonate groups, can make an nonpolar polymer water soluble. The same can be achieved by core–shell synthesis when polyacrylate or polylysine chains are grafted from the surface of the dendrimer [16–19]. What is particularly useful for grafting by controlled radical polymerization is that one can perfectly control the number of initiator groups and thus the number of resulting arms [16]. Since these PPDs are water-soluble their ability to cross cellular membranes can be studied (Sect. 2.5).

Alternatively, a single charge, for example in the form of a borate anion [20] or a phosphonium cation, can be placed in the core of the dendrimer. This furnishes organosoluble salts, whereby the ion inside the rigid capsule is spatially separated from the counterion. It is clear that these objects open new pathways in polyelectrolyte studies, for example, by dielectric spectroscopy. More specifically, there is now a chance to independently studying dissociation and ion mobility as a function of ion size [21] (Fig. 5). Dissociable, shape-persistent dendrimers allow the analysis of the fundamental question of how charges arise in nonpolar liquids.

In nonpolar solvents, ion dissociation is hindered because of the Coulomb attractive energy [22], which for two monovalent charges is:
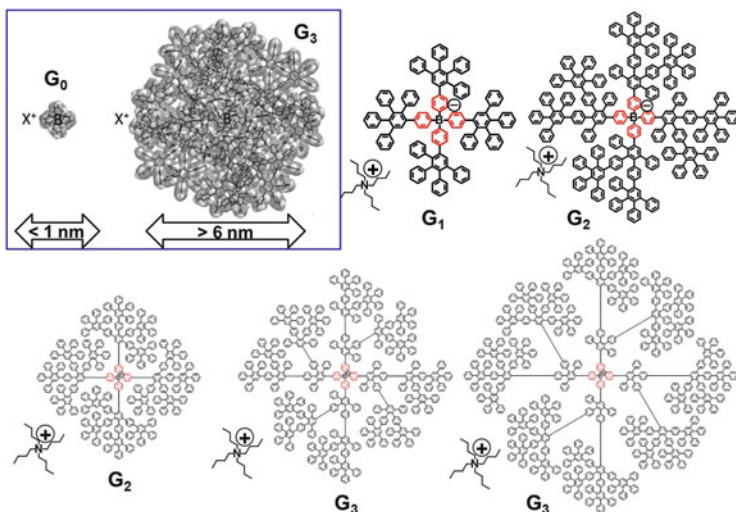
Fig. 5 Increasing size of tetraphenylborate anions via dendronization with polyphenylenes. G_1, G_2, G_3 first, second, and third generation, respectively

$$E_C = \frac{e^2}{4\pi\varepsilon_0\varepsilon_r r_c} \tag{1}$$

Here, e is the elementary charge, ε_0 is the permittivity of free space, r_c is the distance separating a point-like cation from a point-like anion and ε_r is the dielectric permittivity of the surrounding medium. The "escape distance" from the Coulomb energy is set by the Bjerrum length, $\lambda_B = e^2/4\pi\varepsilon_0\varepsilon_r k_B T$, giving the characteristic separation between two ions at which Coulombic interactions are balanced by the thermal energy. Here, k_B is the Boltzmann constant and T the temperature. In liquids of low polarity, such as toluene or even tetrahydrofuran (THF), the Bjerrum length is 20.4 and 7.4 nm, respectively. Ion dissociation in such solvents is limited unless the ion size approaches the escape distance set by λ_B.

Figure 6 schematically describes the effect of solvent polarity and ion size on the Coulomb potential. It shows that increasing the dielectric permittivity of the solvent raises the attractive part of the potential, making the potential less attractive and facilitating ion dissociation. On the other hand, increasing the ionic size effectively shifts the repulsive part of the potential to length scales that approach the Bjerrum length promoting ion separation. With respect to electric conductivity and charge transport, one has to take into account the balance between ion dissociation (promoted by the bulky ions) and mobility (inhibited by the large ions). With respect to the latter, extensive research on increasing the size and bulkiness of molecular anions has led to a new class of compounds known as weakly coordinating anions [23].

With the recent synthesis of ionic dendrimers (Fig. 6) [20] a number of large and rigid molecular ions with dimensions approaching the Bjerrum length in nonpolar

Fig. 6 *Left*: Effective Coulomb energy (*solid line*) showing the effect of increasing dielectric permittivity of the medium (*dashed-dotted line*) and the effect of increasing the anion size (*dashed lines*). *Right*: Dendritic molecules as a function of the anion generation. All molecules share the same cation, i.e., TBA$^+$
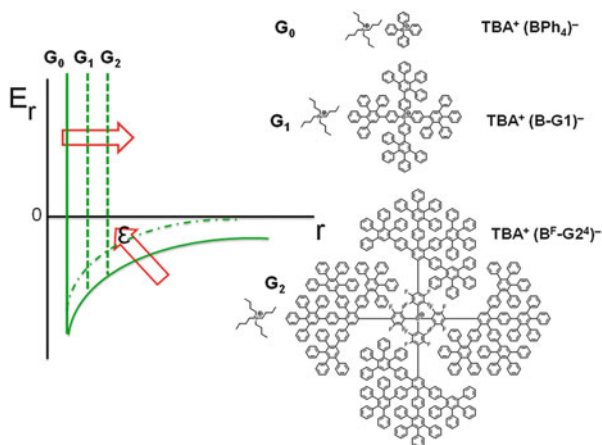
solvents have become available. In addition to the increase in anion size, another approach emphasized the effect of delocalization of the anion charge [21]. It is thought that the spreading of the anion charge to a larger area is responsible for the weaker coordination. However, it is still unknown how the large size, shape, and selective anion functionalization with fluoro-substituted phenylene groups at the anion core and dendritic corona affect the dissociation and eventually the transport properties of ions. To study ion transport, dielectric spectroscopy is the method of choice because of its inherent ability to provide both the degree of ion dissociation and the transport properties through the measured DC conductivity. Herein we report on the ion dissociation and transport properties of a series of tetrabutylammonium salts (TBA$^+$) of rigidly dendronized anions with various sizes (with diameters up to 5 nm) in solution and as a function of the solvent polarity [21].

The DC conductivity of an ion-containing medium is expressed as the sum of the individual contributions of all charge carriers, $\sigma_{DC} = \sum_{i=1}^{n} p_i \mu_i q_i$. Here, p_i, μ_i, and q_i are the number density, the mobility, and the charge of the ith type of charge carrier, respectively. An underlying assumption is that all charge carriers move independently of each other with a constant mobility. In the present case there are two monovalent charge carriers, i.e., the cations (TBA$^+$) and respective anions. Therefore, the DC conductivity of the fully dissociated ions can be expressed as $\sigma_{DC} = p_+ \mu_+ e + p_- \mu_- e$. Measured DC conductivities (with values of $\approx 10^{-5}$ S/cm) for the different dendrimers in THF conform to $\sigma_{DC} = \sigma_0 \exp(-E_\sigma/k_B T)$, where σ_0 is the limiting conductivity and E_σ is the activation energy for ion transport. Furthermore, a linear concentration dependence of the DC conductivity was found, which implies an increasing number of mobile charge carriers at a fixed degree of ion dissociation. The degree of ion dissociation can be extracted from the ratio of the measured DC conductivity σ_{exp} and the calculated conductivity σ_{calc} that assumes complete ion dissociation as $\alpha = \sigma_{exp}/\sigma_{calc}$, also known as the Haven ratio [24]. The denominator can be calculated from the mobility, $\mu_i = e/6\pi\eta r_i$:
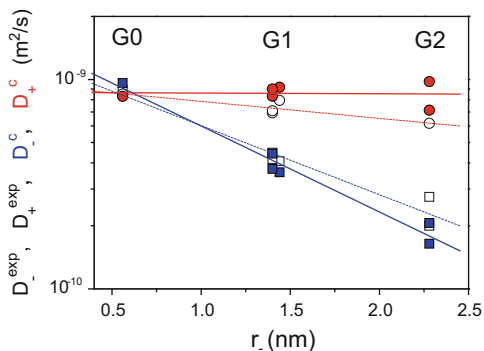
Fig. 7 NMR anion (D_-^{exp}, *open squares*) and cation (D_+^{exp}, *open black circles*) diffusion coefficients plotted for the different generations (G0, G1, and G2) as a function of the anion size. The calculated anion (D_-^c, *filled blue squares*) and cation (D_+^c, *filled red circles*) diffusion coefficients corresponding to free ions are also plotted for comparison. The *solid* and *dashed lines* through the calculated and measured data, respectively, are guides for the eye

$$\sigma_{calc} = \frac{p_s^{e^2}}{6\pi\eta}\left[\frac{1}{r^+} + \frac{1}{r^-}\right] \tag{2}$$

Here, η is the viscosity of the surrounding liquid, $r^{+/-}$ are the ionic radii, and p_s is the total ion concentration from the stoichiometry. The measured DC conductivity differs from the calculated conductivity because the paired charges do not contribute to the current.

Further information is provided by diffusion-ordered spectroscopy (DOSY)-NMR. With DOSY-NMR the diffusion coefficient, D_{exp}, can be measured. The measured diffusion coefficients, however, are not the diffusion coefficients of the free ions. They represent some average of the fully dissociated and paired states. Nevertheless, knowledge of the measured (NMR) diffusion coefficients together with the degree of ion dissociation allows calculation of the diffusion coefficients of the free ions [21].

Figure 7 compares the measured and calculated diffusion coefficients for different anion sizes and generations at 25°C. The NMR diffusion coefficients underestimate/overestimate the respective cation/anion diffusion coefficients with regard to the free ions. However, when coupled with independent conductivity measurements they result in the transport properties of the unassociated species.

Ion dissociation is promoted by fluoro-substitution away from the boron position in the corona. This shows that the reduction of the electrostatic interactions is more effective in producing weakly coordinating anions than the mere delocalization of the anion charge produced by fluorination of the core. In the absence of fluoro-substitution, steric effects gain importance and result in a higher dissociation.

Charging of PPDs in nonpolar solvents is not only interesting from the fundamental physics point of view. On the chemical side, the encapsulation of a borate anion leads to so-called weakly coordinating anions [23, 25]. In many

chemical reactions, including dissociation and solvolysis, one is interested in weak anion–cation interactions [20]. A well-known case is metallocene-catalyzed olefin polymerization, where chain growth occurs at a zirconocenium cation. The necessary counteranion should only weakly interact with the extremely sensitive catalyst center and this is why methylaluminoxanes (MAO) as anionic species without nucleophilic power have become so important. Huge excesses of MAO are often applied and this has prompted the use of tetraphenylborate as stoichiometrically applied counterions. It is clear that our dendritic borates are much larger, giving the possibility to leave the positively charged catalyst as unperturbed as possible during polyolefin synthesis.

## 2.4 PPDs as Light-Harvesting, Light-Emitting, and Photoswitchable Multichromophores

Rylene dyes can be tuned so that absorption and emission cover the whole spectrum of visible light and extend far into the near infrared. It is then logical to incorporate these dyes at the core, in the scaffold, or on the rim of a PPD [26–28]. In that way, one can precisely control the steric and electronic conditions for a Förster resonant energy transfer and for light-induced electron transfer. The resulting dendrimers are unique multichromophoric light-harvesting systems [29–32] and have become important objects, even for single molecule spectroscopy [33–35]. Using, for example, a perylenediimide chromophore as a core, one obtains nanosized emitters with constant fluorescence wavelength, but increasing diameter. These dyes have served as probes for studying the dynamics of solid polymers by defocused widefield imaging. Another good case can be made for using PPDs as active components of light-emitting diodes (LEDs). A well-known troublesome problem is to match the concentration of holes and electrons and to keep the recombination zone away from the electrode. This is normally accomplished by complex multilayer devices. The dendrimers, in a sense, also represent a layer-by-layer design, but now with molecular precision. More specifically, we have synthesized PPDs with a triphenylamine-based hole-capturing layer on the surface [36], an inner layer of triphenylenes where excitons are formed upon charge recombination, and a central core of pyrene that removes the excitons from the area of charge recombination by a rapid energy transfer (Fig. 8) [37]. The light is finally emitted from the inner core. The advantages of this design in terms of device stability and efficiency define a topic of future research.

An additional challenge appears when multiple azobenzenes are introduced into otherwise rigid scaffolds and PPDs thus become stimulus-responsive, molecularly defined nanoparticles [38, 39]. One might argue that incorporation of azobenzenes into polymers or polymer nanoparticles is a well-known concept for changing structures (Fig. 9).

When combined with the rigid PPDs, however, this seemingly conventional method proves of special value. Only two examples will be mentioned. Light-induced transition from the *trans*- to the *cis*-isomer of the dendronized borate anion
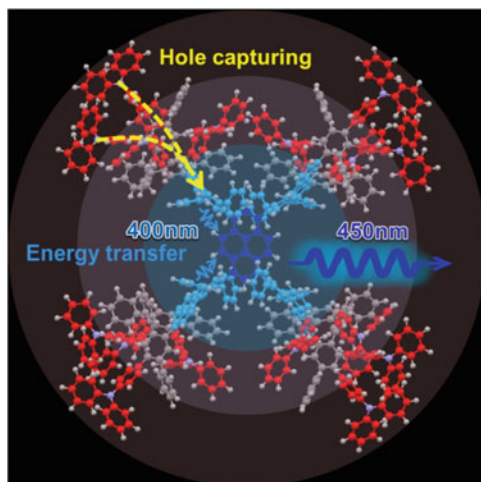
Fig. 8 Dendrimer for light-emitting diodes. Design of a PPD incorporating triphenylamines, triphenylene, and pyrene in defined positions
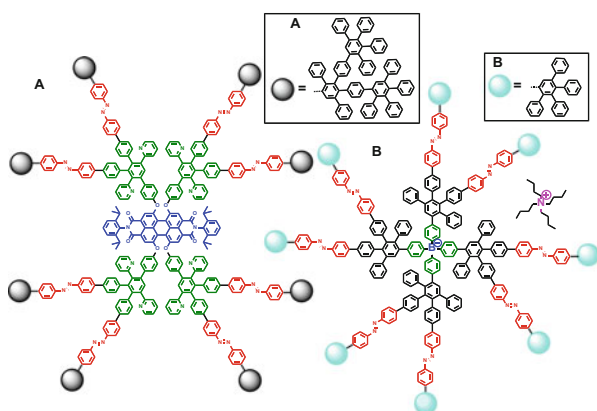
Fig. 9 PPDs with inserted azobenzene units and different cores: (*a*) perylendiimide, (*b*) borate

(Fig. 10a) changes the size of the 3D molecule with high precision. This affects the transport through porous materials. More importantly, the ion conductivity of such salts now becomes photoswitchable. Another case is the related structure with a perylenediimide core. Figure 10b illustrates that the space inside the dendrimer is suitable for the uptake of guest molecules. After forming the *cis*-isomer, the guest molecule is firmly entrapped and can only be released upon back-isomerization to the *trans*-isomer. It is tempting to think of such PPDs as vehicles carrying a payload of drugs, but now with the additional advantage of controlled uptake and release.
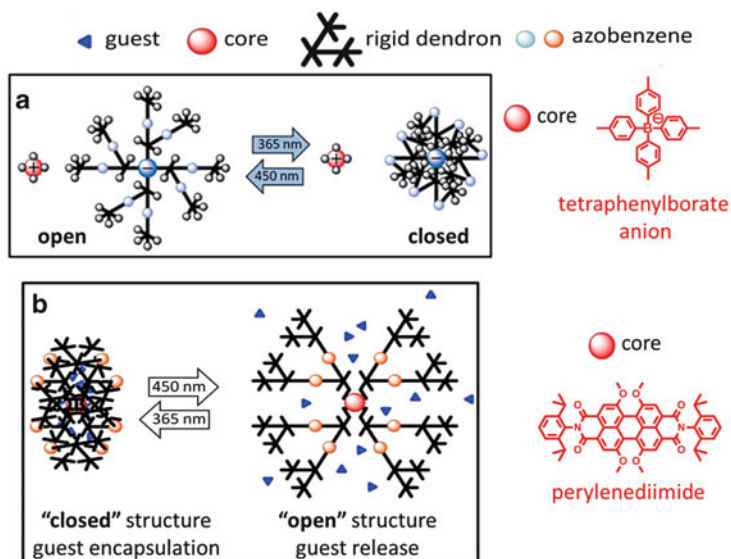
Fig. 10 PPDs with photoswitchable structures

2.5 PPDs as Hosts and Drug Carriers

Another example of designing the interior for suitable guest-uptake is the use of the dendrimers as receptors for analyzing vapors and for sensing of guest molecules [40–42]. Thus, hazardous explosives [43] such as triacetonetriperoxide, which has been used in terroristic attacks, can be trapped with high sensitivity and selectivity and can be detected by an ultra-microbalance that carries the dendrimer on its tip. Indeed, the limit of detection has now reached the picogram range. A challenging task is to understand the steric (size and nature of the voids) and electronic (incorporation of pyridine and imidazole units for activating charge-transfer interactions or hydrogen bonding with the guest) conditions and use this as a guideline for improved receptor design. There are many other useful applications of the PPDs as host or encapsulating species [44, 45] whose detailed description is beyond the scope of this text. One example is the growth of metal nanoparticles inside the rigid dendrimer by reduction of metal salts, thus preventing the particles from undesirable aggregation.

The PPDs thus create a perfect nanoenvironment with increasingly complex function. Admittedly, they define enormous tasks for precision polymer synthesis, but if really sophisticated function is targeted it is worthwhile to take on this challenge in view of the wealth of otherwise inaccessible chemical, physical, and biological properties [10, 46]. Further, there is much to learn when comparing multifunctional dendrimers based upon covalent build-up, with assemblies depending upon weak intermolecular forces. This is indeed another benefit of the structural perfection of the PPDs, that they also allow the fabrication of increasingly complex supramolecular structures.
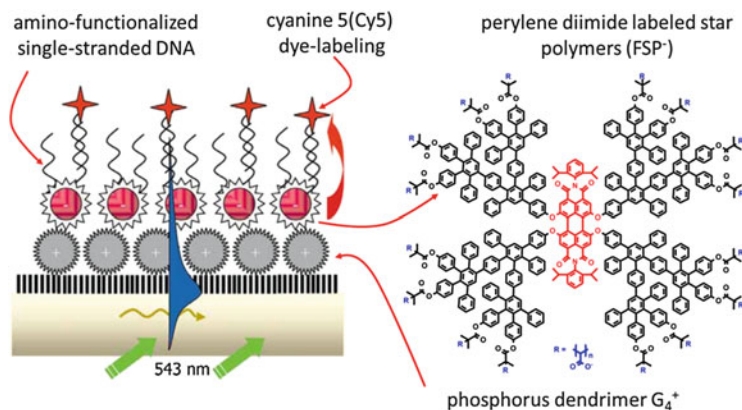
Fig. 11 Representation of a DNA biosensor prepared via layer-by-layer deposition of positively and negatively charged dendrimers

2.6   PPDs as Building Blocks for Self-Assembly

The PPDs can, indeed, serve as building blocks for assembly processes. Long fibers are obtained when their solutions are cast on substrate surfaces [47–49]. Here again, the shape-persistence of PPDs proves of special value because the extended arms can interdigitate, activate π–π interactions between benzene rings, and thus lead to a directional growth of the fibers. There are various ways to further control these self-assembly processes: by alkyl groups or electrolyte functions on the dendrimer surfaces [50] even including desymmetrization by forming amphiphilic Janus-type particles, by introduction of perfluorobenzenes into the interior, or by applying additional templating effects of the surfaces. Different, but equally powerful, cases of assembly processes are the formation of films for highly sensitive DNA detection via layer-by-layer deposition of PPDs (Fig. 11) with oppositely charged surfaces, or cell nucleus staining utilizing electrolyte–electrolyte interactions with histones [51–53].

Although the role of PPDs for cell uptake and drug delivery [16, 54, 55] has already been mentioned, it is important to stress the three key advantages in this regard: (1) the creation of perfect cavities for host–guest interactions, (2) the incorporation of fluorophores at defined positions for monitoring uptake experiments by fluorescence microscopies, and (3) the modification of the dendrimer surface for both water-solubility and transport through membranes [56]. With this in mind, an even more complex design should be introduced. The surface of a dendrimer is again equipped with electrolyte functions for water solubility, but now patches of polar and unipolar domains are formed. It is clear that the shape-persistence of the scaffold proves of key importance for defining the patches. Indeed, the cell uptake of such PPDs has been shown promising for doxorubicin delivery [57]. Even more, the holy grail of delivery experiments has been approached by looking at epithelial cells and, remarkably enough, transport through the blood–brain-barrier could be accomplished. It is not remote to thus

consider the "patched" PPDs as synthetic substitutes of transport proteins, which are also characterized by polar and unipolar surfaces areas of varying size [58].

Dendrimers are without doubt a unique case of 3D macromolecules. In this class, PPDs stand out because of the rigidity of the dendrons, which excludes back-bending. This leads to a pronounced rigidity of the shape, which can be further controlled by choice of the core and the branching points.

2.7 Conclusions

This brief overview illustrates that PPDs (1) are a challenging case of precision macromolecular synthesis; (2) define ample questions for supramolecular studies such as guest uptake, aggregation in solution, and controlled deposition on surfaces; (3) stimulate many functional investigations into sensing and optoelectronics, cell biology, and nanomedicine; and (4), as justified above, are suited for the fabrication of real devices such as ultrastable LEDs. In the meantime, a firm dendrimer community has been established for which the function of the these macromolecules stands in the foreground. It is, indeed, worthwhile to push the limits of complex dendrimer functions even if polymer nanoparticles or hyperbranched polymers are sometimes claimed to do the same job, but at lower cost. In any case, PPDs are unique among the dendrimers due to their structural perfection, stability, and shape-persistence.

3 Cylindrical Brush Polymers

3.1 Introduction

Like the PPDs, cylindrical brush polymers owe their properties to a very special macromolecular design. Attaching many side chains to a polymer backbone is another way of creating a spatially defined rigidity. The length and grafting density of the side chains on a polymer backbone has a profound and tunable influence on the structure and dynamics of the macromolecules. A further option is to introduce ionic charges on the side chains, leading to novel polyelectrolyte structures. PPDs and cylindrical brush polymers, special examples of unconventional polymer topologies, thus jointly offer two challenging possibilities: studying intra- and intermolecular structural changes in cases of controllable rigidity and gaining insight into unprecedented polyelectrolytes.

Bottlebrush polymers contain a long flexible macromolecule as a backbone to which side chains, which may also be flexible, are grafted [59, 60]. The idea then is that via suitable choices of parameters such as the grafting density, solvent quality, and side chain molecular weight the local stiffness of this cylindrical molecular brush can be controlled. The qualitative picture one draws is that of a wormlike
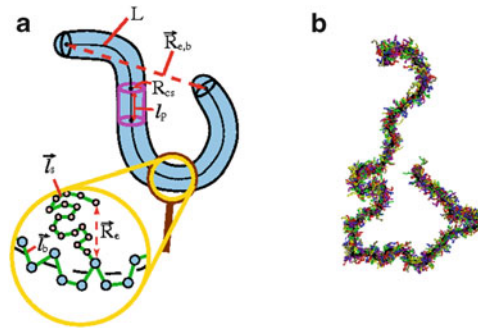
Fig. 12 (**a**) Explanation of the multiple length scales for molecular bottle brush polymers. A coarse-grained continuum description depicts the polymer as a flexible spherocylinder with a cross-sectional radius R_{cs} and a contour length L along the axis of the coarse-grained cylinder, which is straight over a length l_p, the persistence length. A less coarse view (*lower* part of the figure) depicts the backbone as a self-avoiding walk of N_b effective monomers (subscript b indicates the backbone) connected by effective bond vectors $\vec{l}_b$. Side chains with N_s effective monomers and bond vectors $\vec{l}_s$ are grafted to the backbone with grafting density σ. End-to-end vectors of the backbone $\vec{R}_{e,b}$ and a side chain $\vec{R}_e$ are also indicated. (**b**) Snapshot of a typical conformation of a simulated bottle brush polymer, using the athermal bond fluctuation model, with $N_b = 1{,}027$, $N_s = 24$, and very good solvent conditions. From Hsu et al. [61]

chain, described by effective parameters such as the contour length L_{cc} of the backbone chain, the persistence length l_p, and the cross-sectional radius R_{cs} (Fig. 12) [61]. But, the quantitative understanding of this picture has been rather controversial: scaling relations for the dependence of these parameters on the degree of polymerization N_s of the side chains were proposed (e.g. [62]), which turned out at variance with both experiments (e.g., [63]) and simulations (e.g., [64]); moreover, results from experiments on the persistence length of brushes having chemically similar (or even identical) structures disagreed with each other [63].

3.2 Simulations of Single Brushes

Getting this information experimentally is difficult [63] because one needs to do scattering experiments over a range of several decades of scattering wave number, and this has to be done under extremely dilute conditions (see Sect. 3.3 for experiments). However, the simulations [61, 64–66] revealed that the problem is more subtle, simply because the notion of persistence length is well-defined only for semiflexible Gaussian chains [66]. For polymers under good solvent conditions, the applicability of the Gaussian chain statistics (that is also implied by the Kratky–Porod model of wormlike chains [67]), which rather generally is taken to
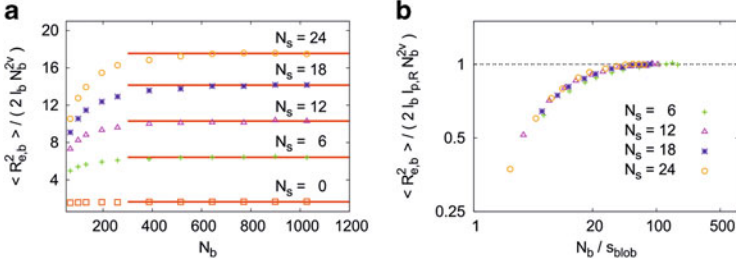
Fig. 13 (**a**) Rescaled mean-square end-to-end distance $\langle R^2_{e,b}\rangle/(2l_b N_b^{2\nu})$, $\nu \approx 0.588$, of the bottle brush polymer under good solvent condition plotted for grafting density $\sigma = 1$ and several choices of the side chain length N_s. (**b**) Rescaled mean-square end-to-end distance, taking the straight line ordinate values from the left plot as ordinate unit, and rescaling the backbone chain length N_b with the number of monomers per blob s_{blob}, as described in the main text. From [61]

be the "gold standard" for stiff polymers [68], is rather restricted. So it turns out that the exponential decay of the bond autocorrelation function $\langle\cos(\theta(s))\rangle$ for bonds along the backbone s steps of length l_b apart, $\langle\cos(\theta(s))\rangle \sim \exp(-s\,l_b/l_p)$, is delicate. Such an exponential decay can only be found for a rather small number of steps [66], $s < l_p/l_b$, but is not asymptotically for $s \to \infty$, where the decay always follows a power law $\langle\cos(\theta(s))\rangle \propto s^{-\beta}$ with $\beta = 2 - 2\nu \approx 0.824$ under good solvent conditions but $\beta = 3/2$ for theta solvents [66]. A Gaussian behavior (as predicted by the Kratky–Porod model) occurs only for polymers in 3D space that are both very stiff and very thin, namely for the contour lengths L in the range $l_p \ll L \ll (l_p/R_{cs})^2 l_p$ [70]. Only in this regime (and in the rather trivial regime $L < l_p$, where the polymer resembles a rigid rod of length l_p) would the Kratky–Porod model be applicable. As we shall see below, for bottlebrush polymers the persistence length (l_p) is not very much larger than their cross-sectional radius (R_{cs}), and then the Kratky–Porod model fails.

However, for bottlebrush polymers where the backbone chain and the arms are flexible, the chain stiffness is a consequence of chain thickness. The simulations give rather clear evidence [61, 66, 70] that the chains do get stiffer with increasing chain lengths of the side chains (Fig. 13a). However, there is a monotonic increase of the mean square end-to-end distance of the backbone with backbone chain length N_b, from the rod-like behavior at small N_b, where we find $\langle R^2_{e,b}\rangle/N_b^{2\nu} \propto N_b^{2 - 2\nu}$ $\approx N_b^{0.824}$ (since rods scale as $\langle R^2_{e,b}\rangle \propto N_b^2$), to coils swollen by the excluded volume forces $\langle R^2_{e,b}\rangle \propto N_b^{2\nu}$ with $\nu \approx 0.588$ [68]; hence, for $\langle R^2_{e,b}\rangle/N_b^{2\nu}$ horizontal plateaus result, as is evident from the data.

It turns out that there is a simple rescaling possible, by which all curves superimpose (at least approximately) on a master curve (Fig. 13b): N_b is rescaled by s_{blob}, the number of monomers per blob, motivated by the idea that the bottlebrush polymer is viewed as a pearl-necklace chain of blobs, the blob radius being the cross-sectional radius of the cylindrical brush. From this condition, s_{blob} is easily derived numerically from the simulation data.

It was also found [69] that in two dimensions (relevant for strongly adsorbed semiflexible polymers), excluded volume effects are much stronger than in three dimensions. This is not just because the exponent ν in the relation $\langle R^2_{e,b} \rangle \propto N_b^{2n}$, $\nu = 3/4$ [68] differs more strongly from the Gaussian value $\nu = 1/2$ than the value $\nu = 0.59$ in three dimensions. As mentioned above, for very stiff and thin polymers in three dimensions, a regime of Gaussian behavior occurs for chains of intermediate length, in between the rod regime (for short chains) and the self-avoiding walk regime (for long chains). In two dimensions, however, there is never a Gaussian regime intermediate between the rod regime ($\langle R^2_{e,b} \rangle \sim N_b^2$) and the swollen coil regime ($\langle R^2_{e,b} \rangle \sim N_b^{2\nu} = N_b^{3/2}$), rather the two regimes join smoothly for $N_b l_b = l_p$. It is also interesting to note that for a given energy of local bond bending, the persistence length l_p depends distinctly on the conditions in which the polymer exists: for an adsorbed stiff thin chain, l_p is about 2.4 times larger than when the same chain is not yet adsorbed. Also, the solvent conditions matter and this has been demonstrated by a simulation [71] of a bead-spring model of a bottlebrush polymer, comparing good solvent conditions (a temperature about 30% higher than the Theta temperature) with Theta conditions. At the Theta temperature, the persistence length is smaller, as expected, because the cross-sectional radius is also smaller.

3.3   Experiments on Individual Brushes

The main conformation of cylindrical brush polymers is governed by two opposing forces: The steric repulsion of the densely grafted side chains leads to stretching of the side chains and of the main chain, whereas the entropy elasticity causes both main and side chains to adopt a coiled conformation. In the case of rigid side chains, the arguments above apply to the main chain only. Rigid side chains were investigated by analytical theory as well as by simulations, but experimental data are rare (see below). An increase in main chain stiffness with the length of the side chains was one major goal of experimental investigations. Usually, the Kratky–Porod wormlike chain model is applied to fit experimental data such as form factors, dimensions such as the radius of gyration (R_g) and the hydrodynamic radius (R_h), and intrinsic viscosities. For a reliable application of the wormlike chain model, the contour length, L, needs to be known. Typically $L = l_m P$, with P being the (main chain) degree of polymerization and l_m the length per repeat unit. For vinyl main chains, $l_m = 0.25$ nm. There was considerable discussion about whether $l_m = 0.25$ nm also applies to cylindrical brush polymers, because AFM investigations resulted in smaller cylinder lengths than expected by the weight-average degree of polymerization, P_w, determined by static light scattering (SLS), even if corrected for main chain polydispersity [72–74]. It was speculated that within the cylindrical geometry the main chain was locally coiled, but persistent on larger length scales. This picture seemed to be supported by simulations, which showed a bimodal decay of the bond angle correlation function [66, 70, 75–77].

Another "caveat" was raised by theory, which revealed the main chain stiffness to decrease from the middle of the chain towards the ends. This relates to the fact that the steric repulsion between the side chains becomes less at both ends due to the hemispherical volume accessible. In addition, the motion of segments near the chain ends is less restricted [66, 70, 75–77]. Accordingly, application of the wormlike chain model with uniform chain stiffness is somewhat questionable, but for long main chains this effect is most probably not pronounced.

3.3.1 Polymethacrylate-Polystyrene Brushes in Toluene and Cyclohexane

A series of cylindrical brush polymers was synthesized with a polymethacrylate (PMA) main chain and polystyrene (PS) side chains of various side chain molar masses, M^{sc}, or side chain degrees of polymerization, $6 < P^{sc} < 33$. The aim was to experimentally investigate the length per repeat unit, l_m, the Kuhn statistical segment length, l_k, and the side chain extension in terms of the cross-sectional radius of gyration, R_{gc}, as well as the segment distribution within the cylindrical cross-section The full scattering envelope was measured by a combination of SLS and SANS. The cross-sectional radius of gyration was determined from the cross-sectional Guinier plot, i.e., $\ln(qI(q))$ versus q^2, with $I(q)$ being the absolute scattering intensity and q the scattering vector. The resulting R_{gc} values are shown in Fig. 14 for measurements in the very good solvent toluene and in the poor solvent cyclohexane. Fits to the scaling law $R_{gc} = k(M_n^{sc})^a$ [78, 79] yields values in toluene, $a = 0.61 - 0.67$, and in cyclohexane, $a = 0.56$. Here, k is a fitting constant and M_n^{sc} is the number average molar mass of the side chains. However, these results should be taken with caution due to the small side chain molar masses investigated, but they are qualitatively in good agreement with the simulation results of the previous section.

From the Holtzer plot of $qI(q)$ versus q [63], the mass per length, M_L, was determined, which translates into the length per monomer unit:

$$l_m = M_0/M_L \tag{3}$$

with M_0 as the molar mass of one repeat unit (Fig. 15a, b). In cyclohexane, $l_m = 0.207$ nm (solid black line in Fig. 15) is obtained, which is significantly lower than $l_m = 0.25$ nm, the usual value for vinylic chains. The situation in toluene is less clear: The average over all values yields $l_m = 0.241$ (solid red line in Fig. 15). A least square fit indicates a decrease of l_m with increasing side chain molar mass (dotted red line in Fig. 15). For small side chains $l_m = 0.26$ is obtained. The experimental uncertainty is, however, too large to allow for an unambiguous interpretation. In addition, the factorization of the scattering envelope into main and side chain form factors might not be justified if the cross-terms between side and main chain scattering are not negligible [64].
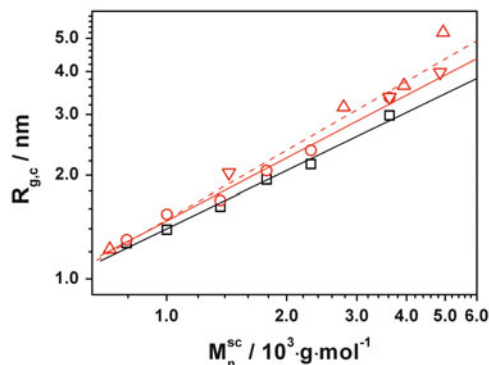
Fig. 14 Cross-sectional radius of gyration versus side chain molar mass M_n^{sc} measured in D8-toluene (*red circles*) and in D12-cyclohexane (*black squares*). Data from [63]. The *red triangles* show additional SANS and SAXS results of PMA-PS samples measured in toluene [80, 81]. The *solid black line* represents a power law fit to the data in cyclohexane, the *solid red line* to the data in toluene [63], and the *dashed red line* a power law fit to all data in toluene
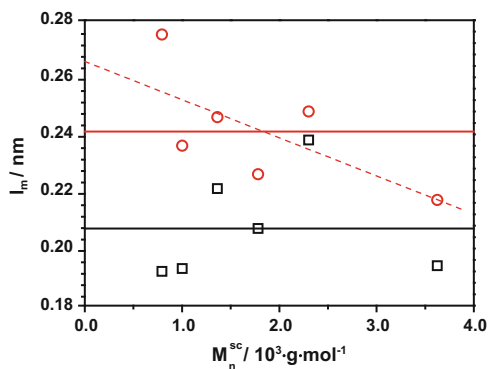
Fig. 15 Cylinder length per monomer as function of side chain molar mass for the samples measured in D8-toluene (*red circles*) and in D12-cyclohexane (*black squares*) as determined by Holtzer analysis. The *solid lines* indicate the mean values of $l_m = 0.241$ nm and of $l_m = 0.207$ nm, the *dotted red line* represents a least square fit to the *red circles*. From [63]

Utilizing the l_m values derived from the Holtzer plateau, the full scattering envelopes were fitted by the Pedersen–Schurtenberger expression for wormlike chains including polydispersity effects (Fig. 16) [63].

A fit of the data shown in Fig. 16 according to:

$$l_k = l_{k0} + k(M_n^{sc})^n \tag{4}$$

yields $l_{k0} = 5.28$ nm, $n = 1.79$ for the data in toluene and $l_{k0} = 5.66$ nm, $n = 1.42$ for cyclohexane. In the equation above, l_{k0} represents the "intrinsic" Kuhn length of
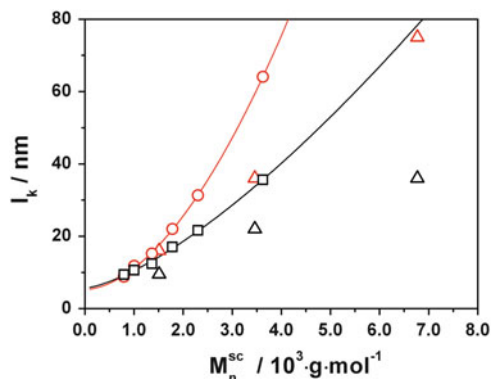
Fig. 16 Kuhn lengths as function of side chain molar mass for samples measured in D8-toluene (*red circles*, [63]; *red triangles*, [82–86]) and for the samples measured in cyclohexane (*black squares*, this work; *black triangles*, [82–86]). The *lines* represent the respective fits according to Eq. (4) (data of [63] only)

the bare backbone without any side chains, which is expected to lie close to the Kuhn length of polyethylene ($l_k = 1.5$ nm). The extrapolated l_{k0} values are much larger. This discrepancy has not been explained so far. Since the exponents n vary significantly with the value of l_{k0} and a range of exponents were postulated by various theories and simulations ($1.375 < n < 1.875$), a detailed discussion does not seem to be meaningful in view of the fact that the experimentally accessible side chain lengths are far too small to show asymptotic scaling properties.

The analysis of the experimental data so far is based on three assumptions: (1) Most seriously, the concept of the persistence length is applicable. Simulations indicate that for good solvent conditions the effective persistence lengths actually diverge with increasing backbone molecular weight. As a consequence, no intrinsic persistence lengths may be derived, only molar mass-dependent apparent persistence lengths. (2) The form factor can be factorized into a main chain part and a cross-sectional part. Simulations have shown that such a factorization may introduce systematic errors [64]. (3) The Pedersen–Schurtenberger expression was derived for values of $R_{gc}/l_k = 0.1$, which is smaller than observed for the present cylindrical brush polymers.

Therefore, it may be elucidating to express the chain stiffness as function of the cross-sectional radius of gyration. As discussed in [87] for bottlebrushes under good solvent conditions, a mapping of the scaling function in Fig. 13b to the scaling function of the mean square radius of gyration of moderately stiff linear chains appears to be possible. It leads to the following empirical relation:

$$l_p = 3R_{gc} \qquad (5)$$

where l_p is the persistence length. In Fig. 17, a direct comparison of the experimental data with the simulation results is shown. The length unit of the lattice model
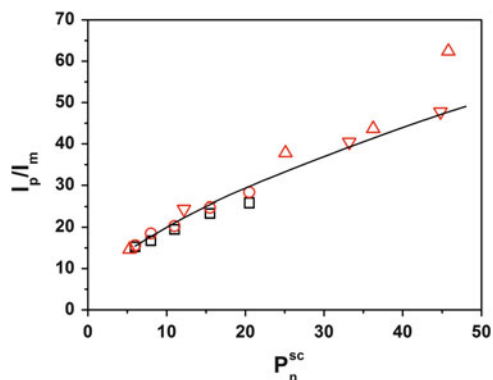
Fig. 17 Comparison of the experimental and simulated persistence lengths normalized to the length of one repeat unit, l_p/l_m, as function of the number-average side chain degree of polymerization P_n^{sc}. Both the simulated and the experimental persistence lengths were derived from the simulated or measured cross-sectional radii of gyration, R_{gc}, according to Eq. (5): simulation (*solid curve*), measurements in toluene (*red circles and triangles*), measurements in cyclohexane (*black squares*)

simulation was converted into physical units by taking the lattice spacing to be equivalent to 0.2 nm. The agreement is good, given the ambiguity in properly establishing the correlation of the simulation model to the chemical details of the experimental system.

3.3.2 Polymer Brushes with Poly-L-lysine Side Chains

In order to address the question of whether or not the specific side chain conformation influences the main chain conformation, cylindrical brush polymers with poly-L-lysine (PLL) side chains were synthesized [88]. Here, we will discussed in some detail the cylindrical brush sample CB-PLL55, which comprises 960 main chain repeat units and an average of 55 lysine repeat units in one side chain sample. Typically, PLL forms a random coil in aqueous solution In aqueous 0.5 M NaClO$_4$ solution, however, it is known to adopt one of the most prominent structures of polypeptides: an α-helix (see also Sect. 6.1) [89]. Upon reduction of the charge density by changing the pH to >9.8 and/or increasing the temperature or by addition of surfactant, a β-sheet structure is favored. Thus, cylindrical brushes with PLL side chains seemed to be ideal candidates for investigating the influence of a coil to α-helix to β-sheet transition of the side chains on the main chain conformation. Indeed, circular dichroism (CD) measurements confirmed that all three side chain conformations also occur in the side chains of cylindrical brush polymers (Fig. 18).

The fit of the CD spectra reveals a helix content of approximately 90%. Although we could not quantify the β-sheet content in absolute numbers, addition of the anionic surfactant sodium dodecyl sulfate (SDS) caused the β-sheet content to increase with
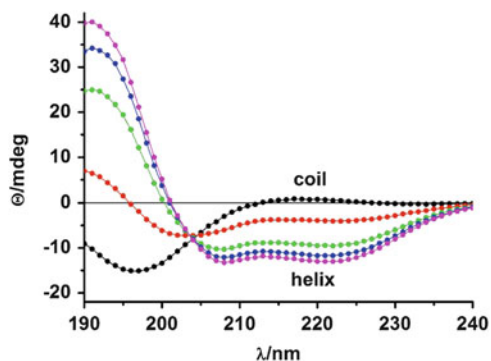
Fig. 18 CD spectra of the cylindrical PLL brush in aqueous solution for different concentrations of $NaClO_4$. The *solid lines* represent the fits to the data by the program Dichroweb: H_2O (*black circles*), 0.1 N $NaClO_4$ (*red circles*), 0.25 N $NaClO_4$ (*green circles*), 0.5 N $NaClO_4$ (*blue circles*), 1.0 N $NaClO_4$ (*magenta circles*). Adapted from [88]

increasing SDS/lysine ratio (Fig. 19). For a molar ratio SDS/lysine >4, aggregation and eventually precipitation was observed.

Unfortunately, quantitative light scattering results could not trace the effect of the coil-to-helix side chain transition on the main chain conformation, because the concomitant increase in ionic strength has a larger impact on the overall dimensions, i.e., leads to a significant decrease. Like many other polyelectrolytes, CB-PLL55 approaches the phase boundary at high ionic strength ("salting out"), which is known to depend on specific interactions with the added salt. This attraction at high salt is qualitatively confirmed by AFM pictures, which show strongly curved cylinders in both NaBr and $NaClO_4$ solutions, which is a clear indication of intramolecular attraction.

In contrast, the AFM pictures as well as cryo-TEM of sample CB-PLL55 prepared from 5 mM NaBr aqueous solution (Fig. 20) show extended cylinders. The cylinders exhibit undulations of the cross-section that are reminiscent of the "pinned clusters" [74, 91] postulated by scaling arguments. The occurrence of pearl-necklace-type structures, where pinned clusters of side chains alternate with regimes that are almost free of side chains, has also been seen in simulations of bottlebrushes, provided one has poor solvent conditions. These clusters are formed by collective collapse of several neighboring side chains [92]. We return to this problem in Sect. 3.5.

It is to be concluded so far, that the coil-to-helix transition of the side chains have no precisely detectable effect on the main chain conformation, since the effects of solvent quality/electrostatic screening are dominating.

The situation is entirely different if the side chains adopt a β-sheet structure. Here, the AFM-pictures in the dry state and measured in solution reveal a helical conformation of the cylinder (Fig. 21). The pitch of the helix lies in the regime of 15–25 nm, which cannot be explained by helix formation on a molecular (i.e.,
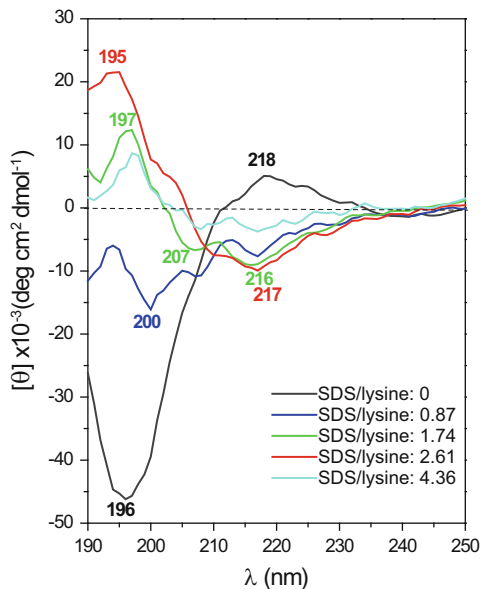
Fig. 19 CD spectra of PLL brush and of PLL–SDS complexes prepared with increasing SDS content. From [90]
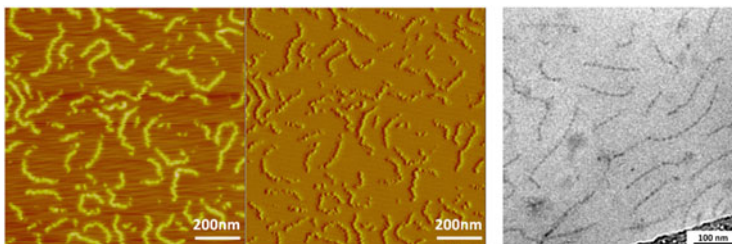
Fig. 20 AFM micrographs of sample CB-PLL55 in 0.005 M NaBr solution (*left* height, *middle* amplitude) and cryo-TEM picture (*right*). From [88]

monomeric) length scale. Rather, the twist of the β-sheet formed by the PLL side chains was postulated to force the main chain into a helix. Although a detailed molecular picture on how the side chains arrange to form the β-sheet structure is still missing, Fig. 21 may well illustrate the simplified origin of the formation of the cylindrical helix. Accordingly, the presented system constitutes an example of an intramolecular hierarchical structure formation.
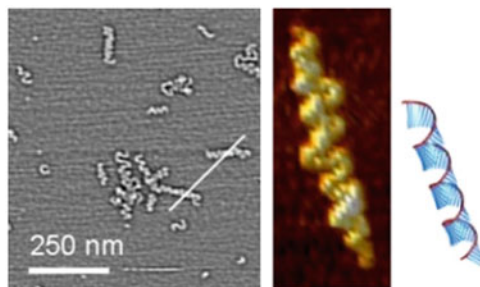
Fig. 21 AFM picture (in aqueous solution on a mica surface) showing helical cylindrical brush–SDS complexes (*left*), 3D presentation of a single helix (*middle*), and drawing of the helix induced by β-sheet formation of the side chains (*right*). From [90]

3.4 Intramolecular Phase Separation Within Cylindrical Copolymer Brushes with Incompatible Side Chains

In addition to the side chain conformation, chemically different side chains attached to the same main chain may also have a pronounced impact on the main chain conformation, particularly if the respective side chains are incompatible. Demixing of the side chain is hampered by the fact that the chemically different side chains are bound to the same main chain, leading to highly frustrated single chain structures. In order to experimentally address this point, the phase separation within statistical cylindrical brush copolymers comprising PMMA and poly-2-vinylpyridinium (PVP) side chains was investigated [93, 94]. The samples were prepared by radical copolymerization of methacryloyl end-functionalized PMMA (M_n^{sc} = 3,700 g/mol) and PVP (M_n^{sc} = 5,100 g/mol) macromonomers. Copolymer brushes with two different compositions were synthesized and characterized as shown in Table 1. Subsequent quaternization of the PVP side chains with ethylbromide was conducted in order to enhance incompatibility.

AFM pictures taken from the nonquaternized copolymer brushes after spin-casting a dilute solution in chloroform onto mica revealed the usual wormlike conformation (Fig. 22). However, the same preparation of the quaternized samples yielded cylindrical brushes with pronounced and regular curvatures. The shorter contour length sample 22PVP47-*co*-78PMMA35-QEB50 almost exclusively formed horseshoe structures (Fig. 23) and the longer copolymer brush 73PVP47-*co*-27PMMA35-QEB70 showed a meander-like conformation (Fig. 23). This behavior was interpreted as intramolecular phase separation of the PMMA and quaternized PVP side chains, as sketched in Fig. 24.

Later, some attempts were made to quantify the curvature of sample 21PVP47-*co*-79PMMA44 as function of the degree of quaternization and of the quaternization agent, i.e., ethyl versus benzyl bromide [94]. With increasing degree of quaternization of the PVP side chains, the curvature radius varies from R_{curv} = 27 nm

Table 1 Light scattering results of the copolymacromonomers in DMF, and AFM results (weight and number-average contour lengths, L_w and L_n) of the samples spincast from CHCl$_3$ solution onto mica

Polymacromonomer[a]	$M_w \times 10^{-6}$ (g mol^{-1})	R_g (nm)	R_h (nm)	L_w (nm)	L_n (nm)
22PVP47-*co*-78PMMA35	1.2	29.9	19.4	52	32
22PVP47-*co*-78PMMA35-QEB50	–	33.1	20.7	–	–
73PVP47-*co*-27PMMA35	4.54	54.9	40.1	143	75
73PVP47-*co*-27PMMA35-QEB70	–	58.8	42.5	–	–
21PVP47-*co*-79PMMA44	2.5	35	27	–	–
50PVP47-*co*-50PMMA44	1.9	27.2	19.9	–	–

[a]Sample code: w%PVP(P_n^{sc})-*co*-w%PMMA(P_n^{sc})-degree of quaternization(QEB) in %
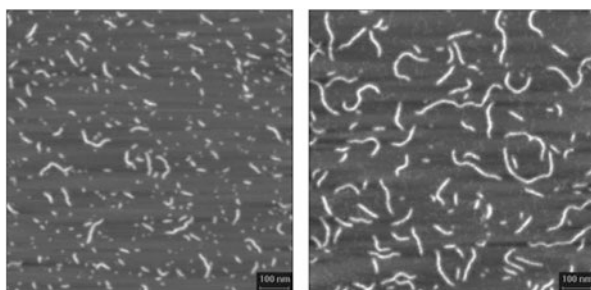
Fig. 22 AFM micrograph (height image) of 22PVP47-*co*-78PMMA35 (*left*) and of sample 73PVP47-*co*-27PMMA35 (*right*) spincast from CHCl$_3$ solution onto mica. From [93]
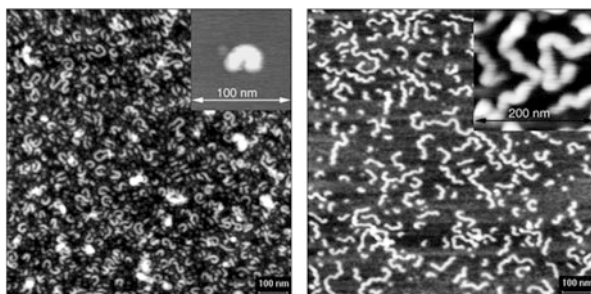
Fig. 23 AFM micrographs (height image, 2×2 μm^2) of the quaternized cylindrical brush copolymers. *Left*: 22PVP47-*co*-78PMMA35-QEB50 spincast from CHCl$_3$ solution onto mica, the *inset* shows the magnification of a single horseshoe-shaped brush. *Right*: 73PVP47-*co*-27PMMA35-QEB70 spincast from aqueous solution onto mica. The *inset* shows the magnification of meandering cylindrical brushes. From [93]
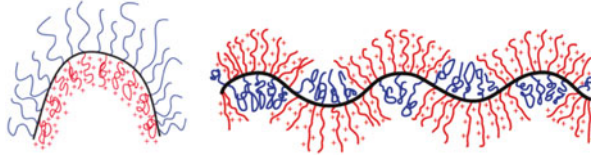
Fig. 24 Sketch of postulated phase-separated side chains in a horseshoe brush (*left*) and in a meandering brush (*right*) [93]
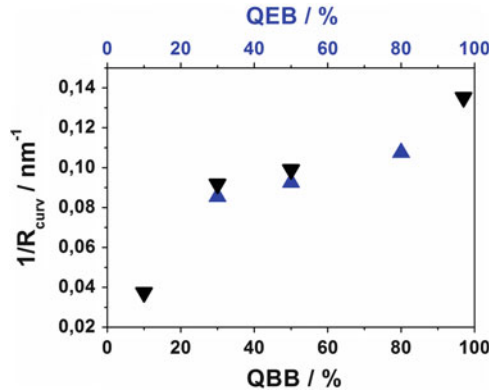
Fig. 25 Inverse radius of curvature determined from AFM pictures as function of the degree of quaternization for sample 21PVP47-*co*-79PMMA44. *QBB* degree of benzylation, *QEB* degree of ethylation. Data taken from [94]

(10% benzylated) down to $R_{\mathrm{curv}} = 7.4$ nm (100% benzylated). Figure 25 shows no pronounced difference in R_{c} for the ethylated and benzylated samples.

Finally, an interesting behavior was observed for sample 50PVP47-*co*-50PMMA44-QBB20, i.e., a cylindrical copolymer brush with 50% PMMA and 50% PVP side chains, which were quaternized to 20% with benzyl bromide. The AFM pictures taken from spin-cast solutions in chloroform are shown in Fig. 26. Almost exclusively two or three cylindrical brushes are observed to align parallel to each other, which is also seen for the ethylated sample 50PVP47-*co*-50PMMA44-QEB58 (Fig. 27).

It should be noted that aggregate formation could be confirmed by light scattering in chloroform solution for the quaternized samples derived from 50PVP47-*co*-50PMMA44, thus qualitatively confirming the conclusion drawn from the AFM pictures.

Evidence for intramolecular phase separation was not only provided by the AFM pictures, but also from X-ray investigations on melt extruded samples [95]. Whereas the unquaternized sample 73PVP47-*co*-27PMMA35 did not show any scattering peak, the quaternized sample 73PVP47-*co*-27PMMA35-QEB70 did show a peak, which indicates a mean distance between more or less ordered structures of
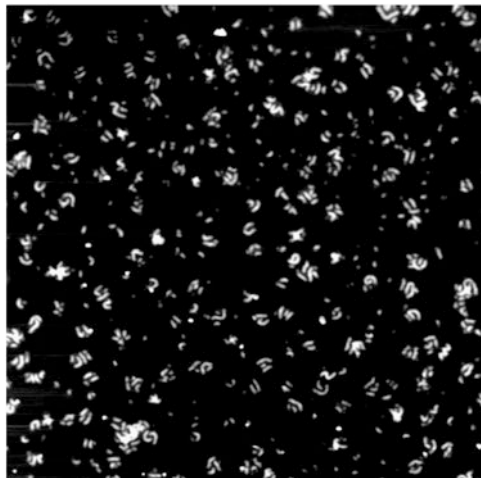
Fig. 26 AFM picture of sample 50PVP47-*co*-50PMMA44-QBB20 spincast from chloroform solution onto mica. Scale:2×2 μm^2. From [94]
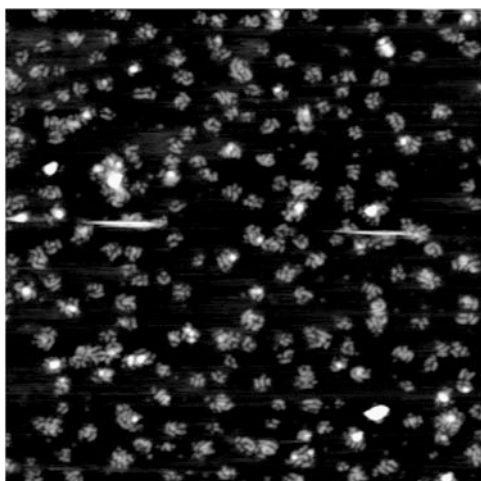
Fig. 27 AFM picture of sample 50PVP47-*co*-50PMMA44-QEB58 spincast from chloroform solution onto mica. Scale: 2×2 μm^2. From [94]

17.25 nm (Fig. 28). Such distance is not compatible with a correlation between single cylinders but rather of cylinder bundles, as sketched in Fig. 29.

In summary, there is ample evidence for the occurrence of intramolecular phase separation in cylindrical copolymer brushes. Since the phase separation is restricted to a length scale of a few nanometers, direct proof is extremely difficult to achieve. In addition, the computer simulations outlined in Sect. 3.5 will show that statistical
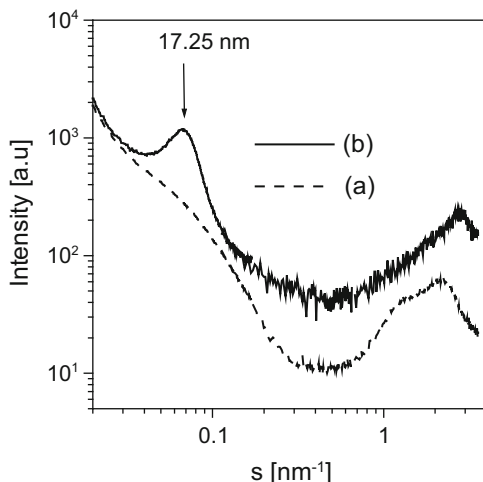
Fig. 28 X-ray scattering intensity versus scattering vector of sample 73PVP47-*co*-27PMMA35 (*a*) nonquaternized and (*b*) quaternized with ethyl bromide (70%) [95]
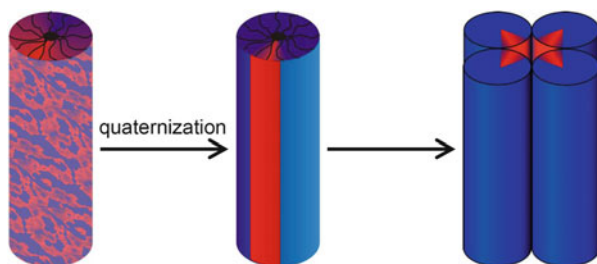
Fig. 29 Proposed scenario for the intramolecular phase separation and subsequent ordering, in order to explain the X-ray scattering peak corresponding to a mean distance of 17.25 nm of correlated scattering objects [95]

fluctuations in a quasi-one-dimensional (quasi-1D) system most probably destroy any long-range order.

3.5 Simulations of Cylindrical Bottlebrush Polymers

For the simulations we consider cylindrical bottlebrush polymers, where two types (A, B) of flexible side chains of length N_A, N_B are densely grafted to a backbone. The degree of (in)compatibility between these constituents can be characterized by a Flory–Huggins parameter χ_{AB}, and the solvent quality is described by Flory–Huggins parameters χ_{AA}, χ_{BB}, as usually done in the phenomenological
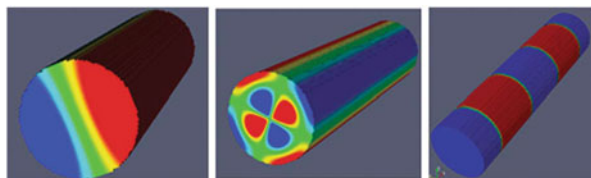
Fig. 30 Schematic phase morphologies of binary cylindrical bottle brushes: Janus cylinder (*left*), Janus dumbbell (*middle*) and lamellar-like (*right*) morphologies. The *red* and *blue* domains are filled by the A and B monomers; interfacial regions are *green*. From [99]

theory of copolymers (or of binary polymer mixtures, respectively) in the presence of solvent [96–98].

Here, we only consider the simplified case where the backbone of the bottle brush polymer is very stiff, so that the bottle brush polymer can be approximated as a rigid cylinder, at least over a large-enough length scale of interest along the cylinder axis that physical effects due to possible bending of the cylinder must be negligible. We shall address the most symmetric case, $N_A = N_B = N_s$ and $\chi_{AA} = \chi_{BB} = \chi$, for the sake of simplicity. An important observation [99] is that for large N_s the problem is in fact equivalent (at least to a very good approximation) to the problem of mesophase formation of symmetrical block copolymers of chain length $2N_s$ confined into a cylinder of radius R with "neutral walls" (i.e., there is no enthalpic preference of the cylinder walls to either A or B). When the solvent quality is poor, then the monomer density in the cylinder can be taken to be essentially homogeneous, and the interfacial thickness of the polymer–solvent interface (at the cylinder surface) is of the order of a few monomer diameters.

First of all, we emphasize that there is a negligible difference between the situation in which A-chains and B-chains (each chain has N_s effective monomers) are grafted alternatively with one chain end to the rigid backbone, and that in which $A_x B_{1-x}$ copolymers (with $x = 1/2$, each chain being twice as large) are grafted with their junctions to the backbone, such that the total number of monomers is identical. Secondly, if these junctions were not grafted to the backbone, but free to move in the cylinder, there would be only a minor entropy gain [99]. Hence, the theory of block copolymer mesophase formation in cylindrical confinement [100, 101], where no constraint on the location of these A–B junctions exists, can be generalized to the present problem [99].

Figure 30 shows the possible mesophase orderings that one might expect [99]. Early work [102, 103] has focused on the possibility of microphase separation in the form of "Janus cylinders" [104], i.e., the cylinder splits into two halves, with a planar A–B interface (containing the cylinder axis, taken to be the z-axis henceforth).

However, it was speculated that other structures could come into play, depending on the ratio χ_{AB} [105]. If A–B contacts are much more unfavorable than monomer–solvent contacts, the formation of a planar A–B interface is unfavorable and instead of a simple cylinder one expects the formation of a double cylinder (i.e.,
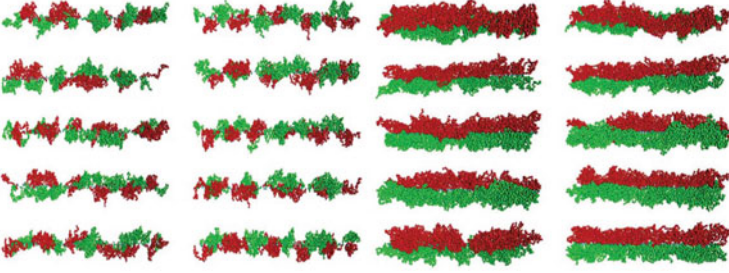
Fig. 31 Snapshot picture of bottle brush polymers at $\varepsilon_{AB} = 1/2$, $N_s = 35$, $T = 1.5$ and $\sigma = 0.57$ (*left*) and $\sigma = 1.5$ (*right*). A and B monomers are distinguished by different colors. From [99]

one cylinder contains the A chains and the other the B chains, both cylinders touch along the straight backbone of the bottlebrush [105]. More complicated morphologies such as Janus-dumbbell morphologies are also conceivable (Fig. 31).

In addition, even for one-component bottle brush polymers under poor solvent conditions it is known from experiment [74], theory [74], and simulation [92]) that mesophase formation in the z-direction along the backbone may occur; namely, the formation of a pearl-necklace structure, where monomer-rich clusters along the backbone alternate with regions almost free of monomers. It is conceivable to obtain a generalization of this structure for the two-component case, where A-rich and B-rich regions alternate along the backbone (Fig. 30). This is a variant of the lamellar structure, well known from block copolymer melts in the bulk [99, 106]. A weak segregation theory along the lines of Leibler [107] has been worked out for this problem, taking into account both the complications of cylindrical confinement and the constraint that the copolymers are tethered to the backbone, and succeeded in showing that for a range of conditions it is in fact the lamellar-like order of Fig. 30 that dominates. However, since this Leibler-type theory [99] is essentially a linear stability analysis around the homogeneous state, it cannot account for strongly nonlinear effects, which are expected to dominate in strongly segregated situations. Therefore, Erukhimovich et al. [99] complemented their study by molecular dynamics simulations of a bead-spring model, choosing side chain lengths of $N_s = 20$, 35, and 50, and working with backbone chain lengths L such that 50 side chains were always grafted. Choosing the interaction of nonbonded beads of the same type as a simple Lennard–Jones potential, with parameters $a = 1$ and $\varepsilon = 1$ setting the scale of length and temperature, the Theta temperature of isolated chains would be about $T_\Theta \approx 3.0$. The Lennard–Jones energy between unlike pairs of beads (ε_{AB}) and the grafting density (σ) along the backbone were parameters that could be varied ($\varepsilon_{AB} = 1/2$, 3/4, 7/8, 15/16, and 1), the value of 1 corresponding to a single-component bottlebrush. Figure 31 shows typical snapshots of the bottle brushes at $\varepsilon_{AB} = 1/2$, $T = 1.5$ and two grafting densities, $\sigma = 0.57$ and $\sigma = 1.51$. One can see that for the smaller grafting density a lamellar-like microphase separation is preferred, whereas for large grafting density

the order along the z-axis is more uniform, more or less compatible with the Janus cylinder-type morphology.

These conclusions have been strengthened by an analysis of suitable correlation functions and structure factors [99]. These results show (Fig. 31) that a cylindrical bottle brush is a quasi-1D object and, as expected for any kind of 1D system, from basic principles of statistical thermodynamics, statistical fluctuations destroy any kind of long-range order in one dimension [108]. Thus, for instance, in the lamellar structure there cannot be a strict periodicity of local composition along the z-axis, rather there are fluctuations in the size of the A-rich and B-rich domains; as one proceeds along the z-axis, these fluctuations are expected to add up in a random fashion. However, in the molecular dynamics simulations of Erukhimovich et al. [99] no attempt could be made to study such effects quantitatively because the backbone contour length L was not very large in comparison with the domain size l_d of an A-rich (or B-rich, respectively) domain.

Because a periodic boundary condition in the z-direction was used to eliminate effects due to the free chain end of the backbone, axial correlations could only be studied over distances z distinctly smaller than $L/2$, to avoid finite size effects. Another complication was that the density distribution in radial direction is still nonuniform for the rather short side chain lengths accessible in the simulations. Also, very long-lived fluctuations occurred, which created strong deviations from the average circular shape of the cross-section of the bottle brush in the xy-plane perpendicular to the backbone. These fluctuation phenomena not only concern the lamellar-like phase, where the translational symmetry along the z-axis is broken, but they also affect the Janus cylinder structure or the phase where the cylinder cross-section has a Janus dumbbell shape (Fig. 30). Here one expects that the orientation of A–B interfaces randomly changes when one proceeds along the z-axis [105, 109, 110]. This problem has been investigated by us with large scale Monte Carlo simulations of a lattice model of bottlebrush polymers [105, 109, 110] , applying the pruned-enriched Rosenbluth method (PERM) [111, 112]. By this method, precise results could be obtained for bottle brush polymers using three choices of the side chain length ($N_s = 6$, 12, and 18) and three choices of the backbone contour length ($L = 32$, 48, and 64 lattice spacings, respectively), studying various solvent conditions. Clearly, these side chain lengths are very short, but they do correspond to the range that is relevant experimentally [93, 113].

When a phase separation into a Janus cylinder structure occurs, e.g., where the upper half of the cylinder contains the B-rich phase and the lower half the A-rich phase, we have a planar AB interface (Fig. 32a) and the quantity that we wish to record is the vector normally oriented to this interface for any monomer of the backbone. Studying the orientational correlations of this vector will yield the desired information on possible fluctuations of interface orientation (Fig. 32b). Since the AB interface at nonzero temperature is not a sharp dividing surface, but rather has a finite width, a numerical characterization of the local orientation of this interface normal is difficult. Therefore, an essentially equivalent but numerically unambiguous characterization of this Janus cylinder-type ordering has been
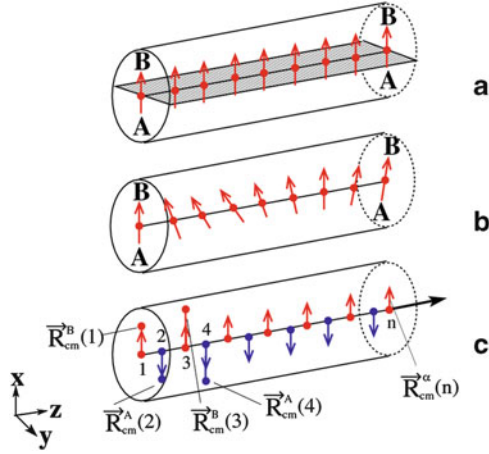
Fig. 32 (**a**) Perfect phase separation of side chains in a binary (A, B) copolymer bottle brush with alternating grafting sequence ABAB... of side chains along the backbone into a Janus cylinder structure implies formation of an AB-interface phase (*shaded*) between the A-rich part (*bottom*) and the B-rich part (*top*) of the cylindrical brush. The local orientation of the interface can be characterized by a unit vector oriented normal to it (*arrows*). (**b**) At nonzero but low temperatures, phase separation will occur locally, but entropy will lead to long wavelength fluctuations of the orientation of this unit vector, destroying axial long-range order along the z-direction of the bottle brush backbone. (**c**) Construction of unit vectors $\vec{R}_{cm}^{\alpha}(j)$ defined as projections of the vector from the grafting site of a chain to its center of mass position into the xy-plane. Here the grafting sites are labeled as $j = 1,2,...$ and $\alpha = $ A or B. $\vec{S}_{cm}^{\alpha}(j)$ then is a unit vector along $\vec{R}_{cm}^{\alpha}(j)$. From [109]

achieved by calculating the unit vector $\vec{S}_{n}^{\alpha}$ ($\alpha = $ A or B) from each grafting site n of the backbone to the projection of the center of mass position, $\vec{R}_{cm}^{\alpha}(n)$ of the grafted chain (Fig. 32c). Because A-chains and B-chains are grafted alternatively to the backbone in our model, the correlation function of interest is:

$$C_n \equiv \left(\left\langle \vec{S}_i^A \cdot \vec{S}_{i+n}^A \right\rangle + \left\langle \vec{S}_{i+1}^B \cdot \vec{S}_{i+1+n}^B \right\rangle \right)/2, \quad i = 1, 3, \dots \quad n = 2, 4, \dots \quad (6)$$

Note that we use an even number of backbone monomers and periodic boundary conditions along the backbone, so there is translational invariance. From this correlation function, a correlation length ξ then is extracted from a fit to:

$$C_n = \text{const}\left(e^{-n/\xi} + e^{-(N_b - n)/\xi} \right) \quad (7)$$

Figure 33a shows a plot of the inverse correlation length ξ^{-1} versus the inverse Flory–Huggins parameter χ_{AB}^{-1} for the three side chain lengths studied, in the case of poor solvent conditions $q = \exp(-\varepsilon/k_B T) = 1.5$, (where ε is the energy that is
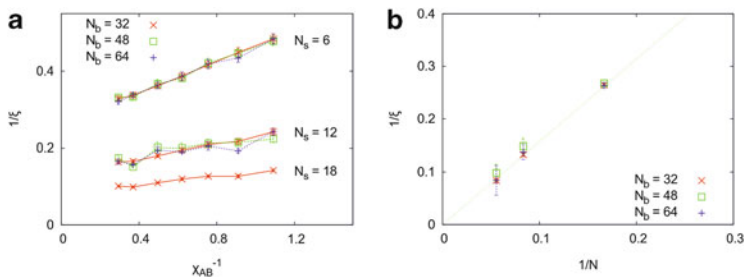
Fig. 33 (**a**) Plot of inverse correlation length for Janus-cylinder-type order versus χ_{AB}^{-1} (with $\chi_{AB} = z_c \, [\varepsilon_{AB} - (\varepsilon_{AA} + \varepsilon_{BB})/2]/k_B T$, $z_c = 6$ being the coordination number of the simple cubic lattice) for the three side chain lengths $N_s = 6$, 12, and 18. These data do not depend significantly on the backbone chain length N_b, as seen from the coincidence of data for $N_b = 32$, 48, and 64, respectively. From [109]. (**b**) Inverse correlation length ξ^{-1} in the limit of $\chi_{AB} \to 0$ plotted versus $1/N_s$ for a poor solvent. The *straight line* suggests an asymptotic behavior $\xi \approx N_s$ in this limit. From [109]

won if two lattice sites are occupied by monomers of the same kind.). Even for $\chi_{AB} \to \infty$ (i.e., the strong segregation limit), the correlation length seems to remain finite for finite N_s. But actually there is a significant increase of this correlation length with increasing side chain length, because, as $N_s \to \infty$ the diameter of the cylindrical bottle brush would become macroscopic, and then long-range order of the Janus cylinder-type occurs.

For real binary bottlebrushes, changes of solvent quality have been shown to lead to very interesting structure formation, such as meander-like or horseshoe-like structures [93]. For a theoretical modeling of such phenomena, it is necessary to take into account both the flexibility of the backbone (and hence a finite persistence length of the bottlebrush [71]and differences in solvent quality for A and B side chains. Although we have studied the effect of solvent quality on the effective stiffness of the bottle brush for homopolymer bottle brushes with flexible backbone [71], an analogous study for binary bottle brushes would be very demanding, and hence has not yet been attempted with the methods described in this section.

The main results of this section are that binary bottle brush polymers show microphase separation but the range over which this mesophase ordering occurs is always is finite, due to the quasi-1D character of these cylindrical brushes. The correlation range over which such order is possible increases with increasing side chain length and grafting density (and with increasing monomer density inside the cylindrical brush caused by decreasing solvent quality and resulting expulsion of solvent molecules from the brush). Apart from "Janus cylinder" and "Janus dumbbell" type structures, lamellar-like ordering (with almost regular alternation of A-rich and B-rich clusters along the backbone) may also occur, in particular for medium values of the grafting density.
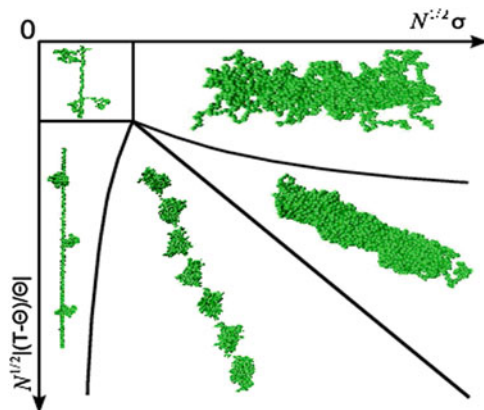
Fig. 34 Schematic phase diagram of a bottle brush polymer with a rigid backbone under poor-solvent conditions, in the plane of variables scaled grafting density and scaled distance to the Theta temperature [92]. The lines separating the different regions have been proposed by mean field arguments [74]. They are not to be understood as quantitative estimates of phase transition lines, but rather as rough estimates of smooth crossovers. Representative simulation snapshots visualize the different microphases

3.6 Complex Formation of Polymer Brushes

The same interactions that dominate the shape of complex macromolecules are also responsible for the formation of defined aggregates and for the adsorption to surfaces, which is described in Section 3.9. As one example, cylindrical brushes are again described. The interaction of side groups with the solvent determines the structure of the macromolecules and the interactions between them as well as with surfaces.

Poor solvent conditions for the side chains grafted to, e.g., a linear polymer (bottle brushes) will lead to intermolecular aggregation; however, interestingly, they can also lead to intramolecular microphase separation within a homopolymer chain. Consider a bottle brush polymer with a very stiff backbone (in the simulations [92] it was modeled as a rigid rod) placed into poor solvent conditions. The resulting structures then depend on solvent quality and grafting density of the side chains, as exhibited in Fig. 34.

For low grafting densities, isolated side chains collapse onto the backbone of the bottle brush. For high grafting densities, a homogeneous cylindrical brush collapses onto itself. For intermediate grafting densities, however, the translation invariance along the backbone is broken upon side-chain collapse, and a microphase-separated pearl-necklace structure is formed.

A similar breaking of the symmetry of the high temperature (good solvent) phase upon side-chain collapse also occurs for an even simpler kind of brush structure, a spherical polymer brush, and there it also leads to a specific form of intermolecular aggregation. Spherical polymer brushes formed from (spherical) nanoparticles to

which flexible polymers are grafted are interesting building blocks for various nanostructured materials [114, 115]. Since it is possible to vary parameters such as the radius (denoted as R_c) of the solid nanoparticle that forms the core of the spherical polymer brush, the grafting density of the macromolecules, their chemical nature, their degree of polymerization, and the chemical nature of the matrix (solvent or polymer melt) in which the spherical polymer brushes are embedded, a rich behavior can be expected [116, 117].

In the theoretical modeling [117–120] to be briefly described here, only limited aspects of this broad field were addressed, namely the case where the density of the nanoparticles in the system is sufficiently dilute such that only the structure of isolated spherical brushes or their pairwise interactions are of interest; dense aggregates formed from more than two spherical brushes were not considered. Two complementary techniques were used, molecular dynamics computer simulation [121] and analytical calculations based on density functional methods [122] and the self-consistent field theory of polymers [123]. We also restrict attention to the case where the grafting density is high enough such that under good solvent conditions the close approach of two nanoparticles (to a distance of a few diameters of the effective monomers) is prohibited by the large entropic penalties; hence, the direct van der Waals attraction of the nanoparticles can always be neglected. Note that for the standard bead-spring model of flexible polymers that is used here [121], every effective monomer represents 3–5 chemical monomers, so one can associate the effective monomer diameter (which is taken as length unit here $a = 1$) to a physical size of 1 nm, while the radius R_c of the nanoparticle typically was about $8a$. Choosing a number N of effective monomeric subunits of the grafted chains from $N = 20$ to $N = 80$, the thickness of the brush coating on the nanoparticles also is a few nanometers, comparable to R_c. Thus, our studies are neither in the limit where the spherical polymer brush can be considered as a many-arm star polymer, nor in the limit $R_c \to \infty$ where the brush coating can be described in terms of a planar polymer brush.

Figure 35 [118] shows typical configurations of two nanoparticles (with a total number of 92 grafted chains containing $N = 40$ effective monomers per chain) under good solvent conditions, for distances between them of $r = 55$ and $r = 20$. In this case, the potential of mean force $W(r)$ between the two particles is uniformly repulsive: although it is practically zero in the first case, i.e., the particles are essentially noninteracting, it is $200 \, k_BT$ for $r = 20$. Such a close approach of the brushes, where the two polymeric shells strongly interpenetrate, therefore cannot occur simply by thermal fluctuations.

However, the situation is different when the solvent quality varies (Fig. 36). Note that we have treated only implicit solvent in the simulations, whereas in the analytical calculations spherical brushes embedded in concentrated polymer solutions could also be treated, to check the extent to which this case resembles a dilute solution under Theta solvent conditions [120]. Figure 36 shows that in poor solvents conditions, for moderate grafting density, the nanoparticle is no longer coated by a uniform polymer layer but the system prefers to form a dumbbell-shaped object. At both the "north pole" and the "south pole" of the nanoparticle
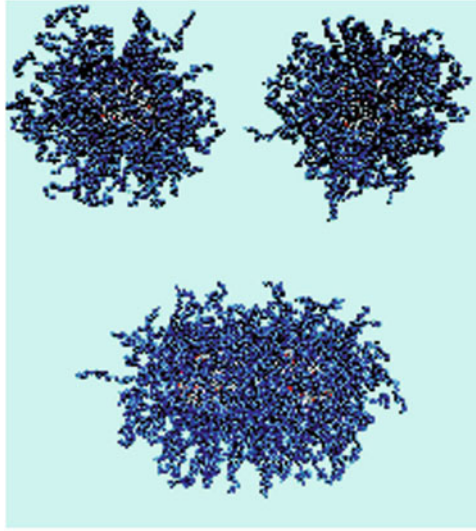
Fig. 35 Snapshot pictures of two spherical polymer brushes with 92 chains, with number of effective subunits $N = 40$ grafted to a nanoparticle with radius $R_c = 7.9$ Lennard–Jones diameters (grafting density $\sigma = 0.118$). Particles making up the nanoparticle are shown in *grey* and *red* (if they are grafting sites); effective monomers of the chain molecules are shown in *blue*. The *upper* picture refers to a separation of $r = 55$ between the core centers, and the *lower* picture to $r = 20$. Effective monomers interact with the repulsive Weeks–Chandler Anderson potential. Adapted from [118]
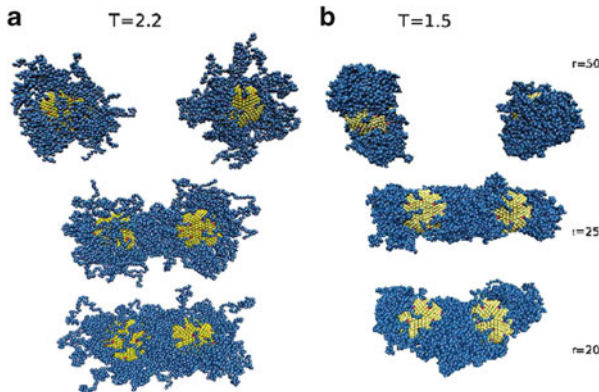
Fig. 36 Same as Fig. 35, but effective monomers interact with a Lennard–Jones potential, which leads to a Theta temperature at $T_\Theta = 3.0$, for temperatures $T < T_\Theta$: (**a**) $T = 2.2$ and (**b**) $T = 1.5$. $R_c = 7$, $N = 60$, and three core–core separations are chosen: $r = 50$ (*upper* picture), $r = 25$ (*middle* picture), and $r = 20$ (*lower* picture). Adapted from [120]
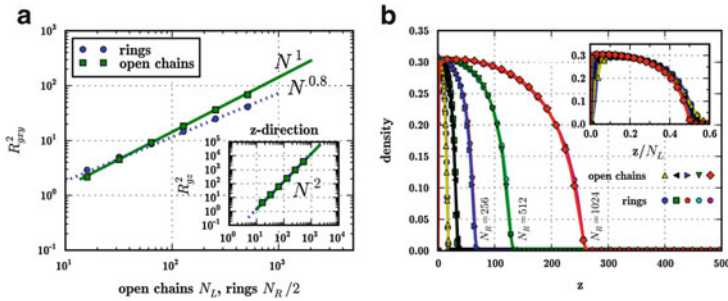
Fig. 37 (**a**) Comparison of density profiles for brushes composed of linear (open) chains and ring chains. A grafted ring polymer typically has the same profile as a linear chain of half length at twice the grafting density. *Inset*: Scaled plot. (**b**) Scaling of the transverse components of the radius of gyration for ring brushes and brushes composed of linear chains. *Inset*: Scaling of the component perpendicular to grafting plane. From [124]

there is a polymer-rich cluster, while the "equator" stays almost free of polymers (of course, the orientation of the north–south axis through the particle is random, resulting from fluctuations when cooling the particle down to a temperature of about $T = T_\Theta/2$, T_Θ being the Theta temperature of the solution. Such inhomogeneous structures, a kind of irregular mesophase where polymer-rich "dimples" alternate with regions that are almost free of polymers, are also known from flat polymer brushes [116]. When two such inhomogeneous spherical polymer brushes approach each other, rather elongated rod-like aggregates may form (Fig. 36b). However, a quantitative analysis shows that in this case $W(r)$ has a deep minimum, of the order of at least $-100\ k_\text{B}T$, so it is clear that Fig. 36b depicts frozen nonequilibrium structures [120].

A very special type of segregation between polymers in brushes also occurs when ring polymers are densely grafted on substrates. The non-crossability constraint of non-concatenated ring polymers causes the effect, even under good-solvent conditions, that the polymers are much more strongly segregated from each other, unlike brushes made of linear chains, where chains laterally interpenetrate much more strongly.

Numerical simulations performed on graphic processing units (GPUs) reveal that density profiles of these peculiar brushes are almost identical to those of linear brushes (at twice the grafting density and half the chain length), and that the radius of gyration scales linearly with N in the direction perpendicular to the grafting plane [124, 125]. The transverse components, however, differ considerably between the two. The radius of gyration scales like $N^{0.4}$ (as opposed to $N^{0.5}$ for regular brushes composed of linear polymers, Fig. 37), and if one looks at individual chains from the top, ring brushes are clearly much more segregated (Fig. 38). Intriguingly, this phenomenon can also be observed in semidilute solutions of ring polymers [126, 127]. There, the inability to interpenetrate other chains due to the lack of an adequate reptation mechanism also leads to a stronger segregation of individual chains and the same scaling behavior that was observed for transverse components is found for the complete chain ($N^{0.4}$ or even $N^{0.33}$ in the thermodynamic limit, versus $N^{0.5}$ for linear polymers).

Fig. 38 Snapshots of individual chains taken from a brush composed of ring chains (*left*) and linear chains (*right*); *side views* and *top views* are shown. From [124]
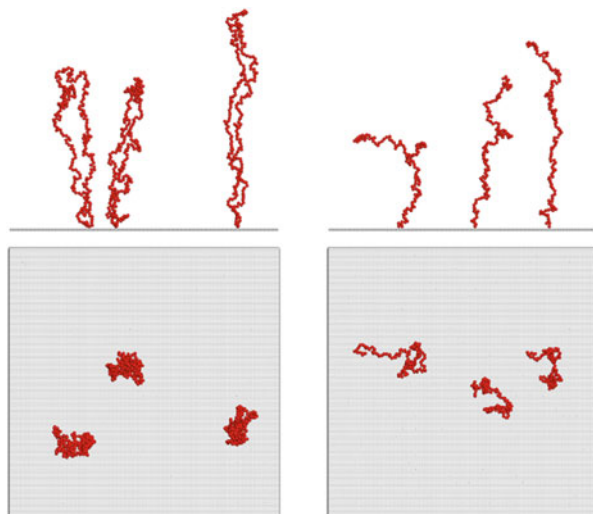
3.7 Complexes Formed in Between Polyelectrolytes in Aqueous Solution

The complex formation of oppositely charged macromolecules is a long-standing subject of interest in polymer science. Whereas complexes comprising linear flexible polyions [128–133] as well as linear polycations and DNA [134–143] are frequently reported, studies on the influence of chain topology are mostly restricted to dendrimers of various generations [144–147]. Only two reports deal with the complexation of DNA and polymers with dendritically branched side chains [148, 149]. We confine discussion to complexes formed by wormlike polyions with large persistence length, such as anionically and cationically charged cylindrical brush polyions and cationic cylindrical brush polymers and DNA. Particular emphasis is given to question of equilibrium versus nonequilibrium complexes.

The complexes formed by excess polycations and DNA have found interesting applications in gene transfection because the complexed DNA is believed to be protected against degradation and the complexes exhibit a more or less pronounced cationic charge, which facilitates cell uptake (Sect. 5). Here, the structure of the complexes should be elucidated with respect to molar mass, radius of gyration R_g, and hydrodynamic radius R_h [150]. This is not easily achieved because complexes are known to be stable only if they coexist with the non-complexed excess component, i.e., either polycation or DNA. The situation is well illustrated by Fig. 39, where the apparent molar mass of the mixture measured at a small but finite concentration is plotted versus the mass fraction of DNA, $w_{DNA} = m_{DNA}/(m_{DNA} + m_{polycation})$ with m_{DNA} and $m_{polycation}$ being the respective mass fractions of DNA and polycation. The data of the various polycations utilized and of DNA are summarized in Table 2 in terms of chain topology, contour length, total charge,
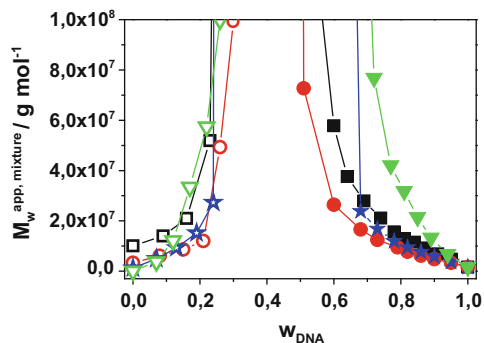
Fig. 39 Apparent molar mass (M_w) as function of weight fraction w_{DNA} for the various polycation topologies: PVP26 (*filled squares*, *open squares*), PVP47 (*filled circles*, *open circles*), PEI (*filled stars*, *open stars*), and PAMAM (*filled inverted triangles*, *open inverted triangles*); DNA excess and polycation added (*closed symbols*), polycation excess and DNA added (*open symbols*). From [150]

Table 2 Characteristics of the polycations and of DNA utilized for complex formation

Polyion	Topology	Size	M_w/M_n	Charges/ molecule ($Z^{+/-}$)	Charge density
PVP26	Cylindrical brush polymer	Contour length $L = 610$ nm	5.3	$<Z^+>_n = 5,500$	48 N$^+$/nm
PVP47	Cylindrical brush polymer	Contour length $L = 100$ nm	3.9	$<Z^+>_n = 2,800$	100 N$^+$/nm
PEI28	Cylindrical brush polymer	Contour length $L = 90$ nm	2.7	$<Z^+>_n = 1,800$	55 N$^+$/nm
PAMAM-G5	Dendrimer	Hydrodynamic radius $R_h = 3.4$ nm	~1	$Z^+ = 127$	(19 N$^+$/nm)
pUC19-supercoiled DNA	Supercoiled DNA	Contour length $L = 930$ nm	1	$Z^- = 5,372$	5.9 P$^-$/nm

and charge density and in Table 3 in terms of molar mass and dimensions. The cylindrical brush polymers have the same PMA main chain but differ in side chain length, which results in different number of chemical charges per main chain repeat unit as well as in different chemistry of the cationic side chains, i.e., ethylpyridinium (PVP) versus ethyleneimine (PEI) side chains. One commercial fifth generation poly(amido amine) (PAMAM) dendrimer sample was included for comparison.

For all polycations, the well known divergence of molar mass is observed in the regime more or less close to charge stoichiometry, indicating agglomeration. In order to determine molar mass and dimensions of the pure complexes by SLS and DLS, the

Table 3 Light scattering characterization of the investigated polymers

Polymer	Solvent	M_w (g mol^{-1})	R_g (nm)	R_h (nm)	R_g/R_h
pUC19	Aq. 5 mM phosphate buffer	1.66×10^6	65.6	43.6	1.5
PVP26	Aq. 10 mM NaBr	10.1×10^6	87.2	48.2	1.8
PVP47	Aq. 5 mM phosphate buffer	3.48×10^6	45.8	33.1	1.4
PEI*HCl	Aq. 0.1 M HCl	1.19×10^6	46.8	26.5	1.8
PAMAM-G5	MeOH + 10 mM LiBr	2.80×10^4	–	3.4	–
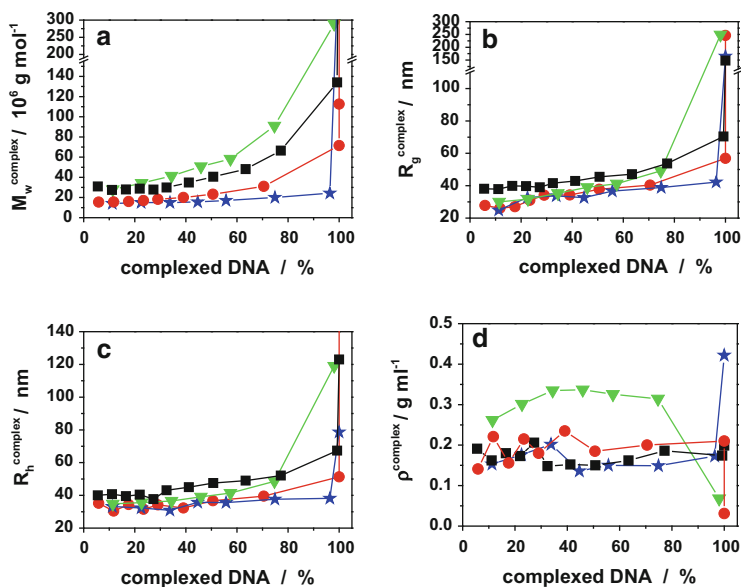
Fig. 40 (**a**) Molar masses, (**b**) radii of gyration, (**c**) hydrodynamic radii, and (**d**) densities of the complexes as function of the complexed DNA fraction for the various polycations: PVP26 (*filled black squares*), PVP47 (*filled red circles*), PEI (*filled blue stars*), and PAMAM (*filled inverted green triangles*). From [150]

weight fraction of the respective excess component needs to be known. This was achieved by gel electrophoresis in case of excess DNA and by GPC in case of excess polycation. As described in detail elsewhere[150], it is straightforward to extract the characterization data of the pure complexes from SLS and DLS of the mixture, i.e., complexes coexisting with excess DNA (Fig. 40a–d) and for excess polycation (Fig. 41a–d). It is found that at large excess of one component, the molar mass and dimensions of such "primary" complexes do not depend on the mixing ratio. Only if the fraction of excess DNA becomes less than 20% or if excess polycation is less than 10% does bridging of primary complexes set in, which eventually results in macroscopic phase separation. Although the complexes consist of several DNA and polycation molecules the sizes are significantly smaller as compared to pure DNA, i.e., the complexes are compacted for all cylindrical brush polycations to a density in
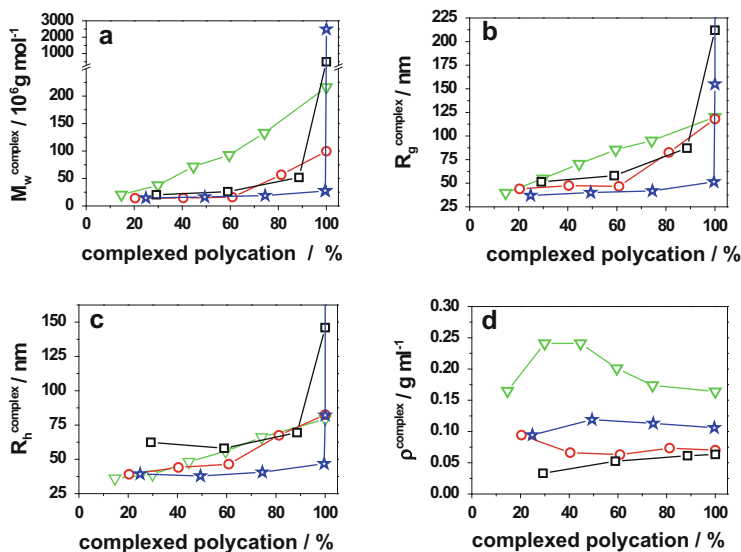
Fig. 41 (**a**) Molar masses, (**b**) radii of gyration, (**c**) hydrodynamic radii, and (**d**) densities of the complexes as function of the complexed polycation fraction: PVP26 (*open black squares*), PVP47 (*open red circles*), PEI (*open blue stars*), and PAMAM (*open inverted green triangles*). From [150]

solution, $\rho = 3M_w/(4\pi R_h^3)$, of $0.15 < \rho < 0.25$ g/cm^3 for excess DNA and somewhat less compacted for excess polycation, i.e., $0.05 < \rho < 0.1$ g/cm^3. For the PAMAM dendrimers, the density is even larger, i.e., $\rho = 0.3$ g/cm^3 for excess DNA and $\rho = 0.2$ g/cm^3 for excess PAMAM. Approximately five to ten DNA molecules are in one primary complex if the complexes are formed at excess DNA, whereas three DNA molecules are in one complex if formed at excess polycation.

Another result concerns the charge stoichiometry within one complex. For excess DNA, $Z^+/Z^- = 0.8$ whereas for excess polycation $Z^+/Z^- = 3$. It should be noted that these numbers do not represent the effective charge but the chemical charge of the complexes, which may include sterically shielded charges in the interior of the cylindrical brushes and ignores possible reduction of charges by counterions (Manning condensation, ion pair formation).

In summary, the complexes of DNA with the various cylindrical brush polycations form primary complexes of constant size as long as no intercomplex bridging occurs, whereas for PAMAM the complex mass and size increase monotonically with increasing content of the minority component. It should be noted that all complexes constitute nonequilibrium structures because size and stability depend significantly on the preparation conditions. For instance, dropping the minority component into the excess component under stirring, which was applied for the experiments described above, yields more stable and smaller complexes than those prepared by rapid mixing in a stopped-flow device. Also, the sequence of mixing matters. Adding the excess component to the minority component, which is avoided in the experiments above, seems to be problematic because the titration
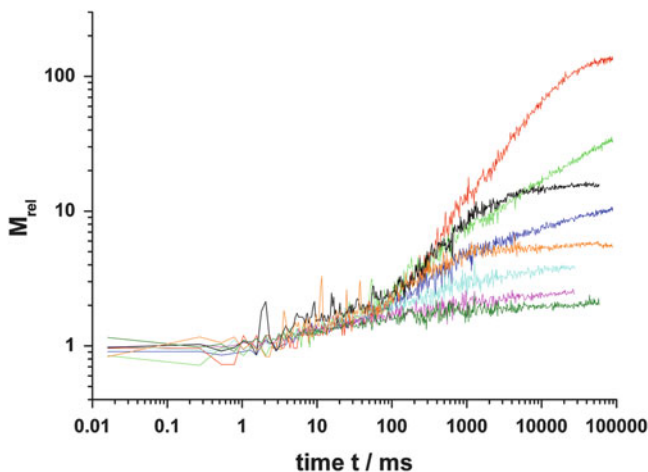
Fig. 42 Relative molar mass $M_{rel}(t)$ as function of time for complexes formed at different charge fractions x_{anion}. From top to bottom: $x_{anion} = 0.398$ (*red*), 0.332 (*green*), 0.498 (*black*), 0.284 (*blue*), 0.665 (*orange*), 0.249 (*light blue*), 0.199 (*magenta*), and 0.166 (*dark green*). From [151]

passes through the "unstable regime" in which phase separation is known to occur. Rapid mixing and vigorous stirring might avoid macroscopic phase separation, but the problem is obvious.

Recently, a light scattering stopped-flow cell was developed with a dead time of less than 5 ms, thus allowing for kinetic measurements of the apparent molar mass starting at 10–50 ms after mixing [151]. With such a device, the complexation kinetics of DNA with a cylindrical brush polymer with PVP side chains was investigated. The results are summarized in Fig. 42 for different mixing ratios, expressed by the mole fraction of anionic charges x_{anion}. For $x_{anion} < 0.25$ stable complexes are observed to form on a time scale of 60–70 ms. For $0.2 < x_{anion} < 0.4$ the complexes first grow on much larger time scale up to a maximum of 10 s for $x_{anion} = 0.4$, followed by a power law behavior, i.e., $M_{rel} \approx t^d$. Here M_{rel} is the increase in molar mass relative to the bare mixture of polycation and DNA, the time t, and the exponent $d \ll 1$. However, no theoretical explanation for $d < 1$ has been derived so far.

Many more and more detailed investigations of the kinetics of complex formation are needed in order to develop a deeper understanding of such nonequilibrium processes. These first experiments merely demonstrate the potential and the need to elucidate the kinetics of nonequilibrium structure formation.

Besides investigating nonequilibrium complexes, it is equally challenging to direct electrostatically driven complex formation into equilibrium. One vision was to obtain anisotropic complexes by mixing rod-like polycations and polyanions, such as anionic and cationic cylindrical brushes or cationic cylindrical brushes and DNA. In aqueous solution "scrambled egg" structures were always obtained by mixing cylindrical brush polymers with polystyrene sulfonate and with PVP side chains as well as by mixing cylindrical brushes with PVP or PLL side chains with
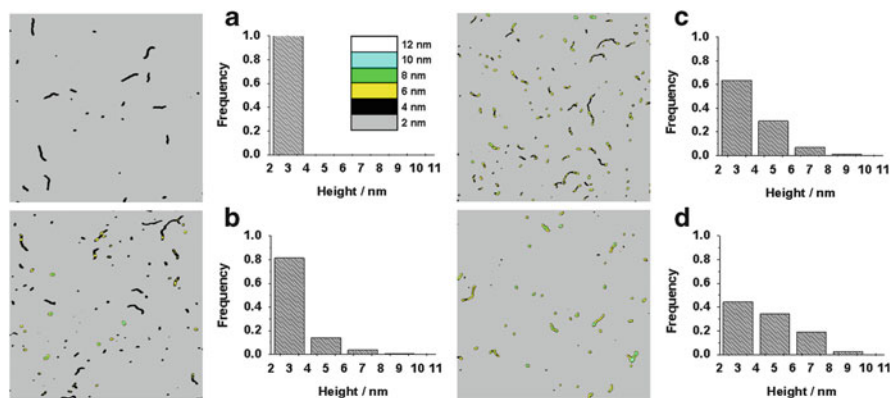
Fig. 43 AFM pictures and analysis of results for the complexes (spincast on freshly cleaved mica) between cylindrical brushes with PSS-surfactant side chains and with PEI-PEO side chains with increasing mass fraction *w* of cylindrical brushes with PEI-PEO side chains: (**a**) *w* = 0, (**b**) *w* = 0.33, (**c**) *w* = 0.7, and (**d**) *w* = 0.87. From [152]

plasmid and linear double-stranded DNA. It was speculated that strong electrostatic interactions prohibit the formation of well-organized structures. Addition of salt did not change much except that the complexes became larger and eventually unstable due to the well-known salting-out phenomenon.

3.8 Complex Formation Between Weakly Charged Polyelectrolytes in Organic Solvents

One strategy is to strongly reduce the ionic charges of the components. This was accomplished by excluding water as the solvent due to solubility problems and favoring solvents like alcohols, *N,N*-dimethylformamide (DMF), etc. Two examples utilizing cylindrical brush polymers as templates for single brush complexes have been successful so far [152, 153].

A polyelectrolyte/surfactant complex consisting of cylindrical brush polymers with polystyrene sulfonate side chains and dodecyltrimethylammonium bromide (DOTAB) was dissolved in DMF. In DMF some of the surfactant groups dissociate. For the polymer/surfactant aggregate, this leads to slightly anionically charged cylindrical brush polyions. The weak cation was a cylindrical brush with a PMA main and PEI side chains. The side chains were grafted by six PEG2000 chains per PEI side chain. Upon mixing in DMF, both light scattering and AFM revealed the larger PSS-C12 brush to act as a single molecule template for complexation of shorter PEI-PEG brushes (Fig. 43), i.e., several PEI-PEG brushes were complexed by one single PSS-C12 brush. Upon increasing the fraction of PEI-PEG brushes, the height of the complexes increased. At the same time, the molar mass measured by SLS was shown to strongly increase at constant radius of gyration (Fig. 44). Since

Fig. 44 *Upper graph*:
Reduced light scattering
intensity $(R(q = 0)/c)_{complex}$
measured at one small but
finite concentration and
extrapolated to zero
scattering vector of the
complexes between
cylindrical brushes with
PSS-C12 side chains and
with PEI-PEO side chains.
Values are normalized by
the respective calculated
scattering intensity of the
mixture, $(R(q = 0)/c)_{mixture}$,
as function of the weight
fraction of the cylindrical
brush with PEI-PEO side
chains. *Lower graph*:
Apparent radii of gyration
measured at one small but
finite concentration. From
[152]
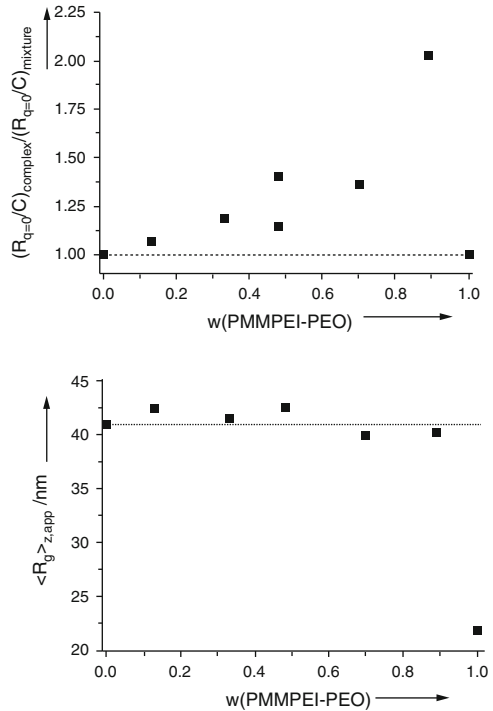
the sequence of mixing did not affect the results, the complexes are most probably equilibrium structures.

Similar results were obtained for mixtures of a cylindrical brush polymer with PSS-C12 side chains and fifth generation PAMAM dendrimers. In methanol large aggregates were obtained, whereas in both DMF and methyl formamide (MFA), single cylinder complexes were identified by AFM and by light scattering. Obviously, not only the effective charge (via the dielectric constant) governs electrostatically driven structure formation but also subtle solubility effects. Additionally, the nature of the solvent (protic versus aprotic) plays a role.

It should be mentioned that no equilibrium structures (neither in methanol nor in DMF) have been obtained so far with plasmid and various linear DNA–surfactant complexes and cylindrical PVP brushes [154].

3.9 Adsorption to Surfaces

The same interactions that determine intramolecular structure and aggregation also play a role in adsorption to surfaces. When a simple linear macromolecule interacts with a surface and becomes adsorbed, its structure changes from the 3D "mushroom" conformation to the (quasi)-2D "pancake" conformation [155]. In the
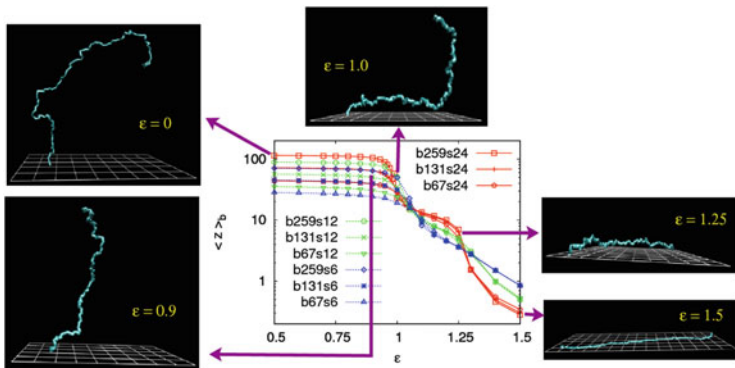
Fig. 45 Average distance $<z_b>$ of a backbone monomer from the adsorbing surface plotted versus adsorption energy ε (in units of the thermal energy $k_B T$) for several choices of the backbone chain length N_b and side chain length N_s (denoted as $b\ N_b\ s\ N_s$). For $N_b = 131$, $N_s = 24$, typical snapshots of the backbone chain are shown for five values of ε. Note that the simulation refers to the bond fluctuation model, where every monomer takes all sites of an elementary cube of the simple cubic model, but only the z-coordinate of the four lower sites of the cube is counted for computing $<z_b>$. Note also the logarithmic scales of the figure. Adapted from [157]

weakly adsorbed case, the chain in the pancake is an irregular sequence of "trains" (strictly 2D pieces of the chain attached to the planar substrate) alternating with "loops" (and "tails" at the chain ends) [123].

For the adsorption of macromolecules with complex architecture, such as bottle brush polymers, it is an intriguing question how the above picture of polymer adsorption changes; after all, most manipulations of macromolecules with external devices (e.g., AFM tips) presuppose that the macromolecule is situated at a suitable surface [156], rather than freely diffusing in the 3D space of a more or less dilute polymer solution.

The coarse-grained view of a bottle brush in 3D space is often similar to the wormlike chain model [59–61]: a more or less randomly bent cylinder with cross-sectional radius R_{cs}, contour length L along the contour axis, and persistence length l_p (meant to describe the local chain stiffness). Obviously, it is not completely clear how such a structure changes when the macromolecule interacts with an adsorbing surface. Do we expect a wormlike structure, where (like for a real living worm) the local cross-section of the worm is still spherical? If so, only a few monomers on the periphery of the bottle brush touch the substrate. However, it could also be that the bottle brush becomes adsorbed to the surface somewhat more strongly, so its local cross-section could look like a sphere cap rather than like a sphere. This situation is analogous to droplets at walls under incomplete wetting conditions [158]. If the picture of a sequence of trains and loops is still valid, the structure in the trains and loops could well be different. Finally, when the adsorption strength is very pronounced, the bottle brush can become forced into a quasi-2D flat configuration attached to the substrate. Then locally it would look like a comb, with spikes stretching away from the backbone at both sides. Given the fact that, in reality, the chemical structure of the backbone will differ from the chemical

Fig. 46 Snapshot pictures
of adsorbed bottle brushes
for the case $N_b = 131$,
$N_s = 24$ and two values
of ε: (**a**) $\varepsilon = 1.25$ and
(**b**) $\varepsilon = 2.0$. Different side
chains are in different colors
(the backbone is in light
blue). Adapted from [157]
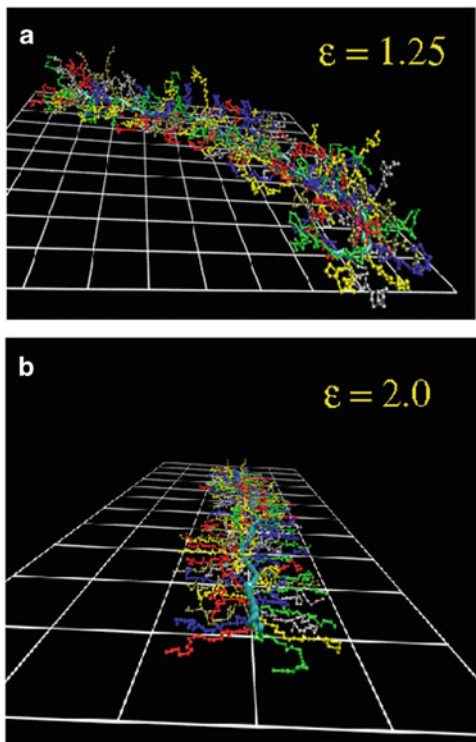
structure of the side arms, many model parameters may come into play when a simulational modeling of this problem is attempted. However, for the sake of simplicity this possible difference in chemistry has been ignored [157, 159]; thus, in the modeling results (cf. Fig. 45) [157] a single parameter ε occurs (units chosen such that $k_B T = 1$) that describes the strength of the short-range adsorption potential.

The simulations have revealed a two-stage adsorption process for a bottle brush polymer (Fig. 45): In the first stage, the configuration changes from mushroom-like structures where only very few monomers near one backbone end are bound to the surface (state with $\varepsilon = 0.9$ in Fig. 45) to a weakly bound wormlike chain ($\varepsilon = 1.25$ in Fig. 45). We find that for an absorbed bottle brush a more realistic picture than a worm is a "millipede": many "arms" (i.e., side chains of the bottle brush polymer) touch the substrate, all along the backbone, but the latter is still elevated. The typical distance $<z_b>$ of the backbone from the surface is still of the order of 10 lattice spacings (in the bond fluctuation model that is used here, bond lengths vary from 2 to $\sqrt{10}$ lattice spacings, and the number of effective monomers in a side chain in Fig. 45 varies from $N_s = 6$ to $N_s = 24$). At the transition from the mushroom to the millipede structure (near $\varepsilon \approx 1.3$), a second transition to a strongly adsorbed state occurs, $<z_b>$ is of order unity, and the backbone monomers

become more or less completely attached to the wall. But, even in the weakly adsorbed regime, such as $\varepsilon = 1.25$, one finds clear evidence that the backbone extension exhibits a scaling with the number of backbone monomers N_b compatible with 2D self-avoiding walks, $L \propto N_b^{2\nu(2d)} = N_b^{3/2}$ [68]. The snapshots in Fig. 45 show only the backbone chain, whereas Fig. 46 shows snapshots of a rather short bottle brush ($N_b = 131$, $N_s = 24$) in the weakly adsorbed ($\varepsilon = 1.25$) and strongly adsorbed ($\varepsilon = 2.0$) cases. Note that for $N_b = 131$ and $\varepsilon = 2.0$, the rod regime still holds and the contour length L of the (coarse-grained) cylindrical macromolecule does not exceed the persistence length l_p. Note also that the side chains are not fully adsorbed linear "spikes", but rather exhibit an irregular sequence of loops and trains: so the picture of a comb lying flat on the surfaces is not yet appropriate.

3.10 Conclusions

Cylindrical brushes constitute a hybrid between a branched polymer and a molecular object. Their shape is strongly anisotropic but both main and side chains preserve their intrinsic flexibility, although with strongly reduced degrees of freedom. The presented simulations demonstrate that the established wormlike chain models are not applicable for the determination of chain stiffness, which could well be the origin of diverging experimental results in the past. Particularly valuable is the finding that a global relation between the main chain stiffness and the cross-sectional diameter of the brushes is much more promising than subtle bond angle correlation functions in order to obtain a good measure of the directional persistence.

The unique structure of cylindrical brushes makes them ideal candidates to (1) experimentally and theoretically study the phase separation in quasi -1D molecular objects, (2) investigate the properties of polyelectrolyte complexes of shape-persistent polyions, (3) elucidate the adsorption on planar surfaces, and eventually (4) develop novel cationic carriers for gene transfection, as described in detail in Sect. 4.

4 Supramolecular Structure Formation by Directed Interactions

4.1 Introduction

The formation of intermolecular structure of the cylindrical brushes described in the previous section is mainly governed by their anisotropic shape, which enables them to form even lyotropic phases. Other driving forces are of ionic and/or entropic

origin or comprise thermodynamic phase separation, which typically do not induce preferred directions. One exception is the intramolecular β-sheet formation of the side chains in cylindrical brush structures with PLL side chains, which originate from intramolecular hydrogen bonds. The latter belongs to the class of interactions that induce a certain orientation. Such directional interactions are the main subject of this section, where more complex and highly ordered supramolecular structures are described on the basis of hydrogen bonds and shape-dependent π–π interactions. Here the investigations are focused on the interplay of both types of interactions occurring in the same system.

A particularly valuable tool for studying intra- and intermolecular interactions is solid-state NMR. Advanced solid-state NMR, combined with X-ray scattering and computer simulation, provides site-selective and noninvasive information of noncovalent interactions such as hydrogen bonding and π–π interactions. For this reason, we first briefly introduce the NMR techniques and then describe specific applications to macromolecular and supramolecular systems, including hybrids of synthetic polypeptides, hybrids containing synthetic polymers, polymers with incompatible segments, and systems containing rigid rods or rings.

4.2 Solid-state NMR Techniques for Analyzing Structure and Dynamics

Signals originating from hydrogen-bonded protons are well separated in ^{1}H magic-angle spinning (MAS) NMR spectra, typically resonating between 8 and 20 ppm [160]. The ^{1}H chemical shift includes semiquantitative information about the strength of the hydrogen bonds. In addition, the ^{1}H chemical shift is also a sensitive probe with respect to ring currents associated with aromatic moieties [161]. This is observed as a low field shift of the chemical shift compared to the corresponding liquid state signal and may thereby serve as a direct indication of π–π interactions. Likewise, the low field shift can be simply related to the packing via so-called nucleus independent chemical shift (NICS) maps [162]. This augments the well-known sensitivity of ^{13}C NMR chemical shifts to local conformation [163]. Detailed packing information is obtained from distance measurements between specific proton sites at adjacent building blocks via high resolution double quantum (DQ) solid-state NMR under MAS. Disk-shaped moieties that stack into columnar structures known as discotic liquid crystals have been studied extensively. In the liquid crystalline (LC) phase, the disks rotate about the column axis. A particularly simple way of characterizing such restricted molecular dynamics is provided by the dynamic order parameter S, where $0 \leq S \leq 1$. It is defined as the ratio between the motionally averaged and the static anisotropic NMR interaction, e.g., dipole–dipole coupling, anisotroc chemical shift, or quadrupole coupling [160]. For the rotation of disks in a perfectly packed column,

Fig. 47 Overview of systems, phenomena, and techniques for elucidating the interplay between structure and dynamics in macromolecular and supramolecular systems
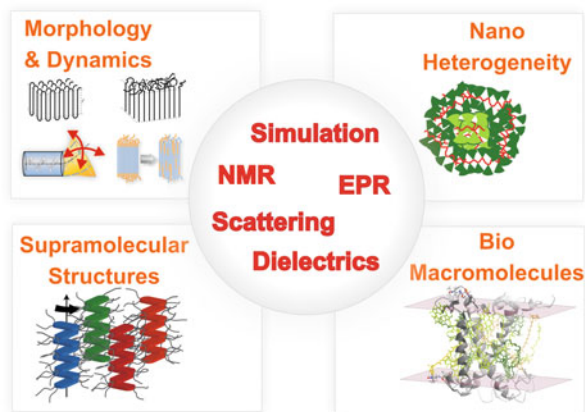
$S = 0.5$ for ^{13}C-^1H dipole–dipole coupling, or ^2H quadrupole coupling, centered around the C–H (C–D) bond direction. Imperfections of the packing in the LC phase, where disks are inclined to the column axis, lead to a reduction, $S < 0.5$. Thus, S provides both dynamic and structural information. In general, solid-state NMR can provide site-selective information about the amplitude and time scales of molecular motions over broad ranges of length and time [164].

Advances in the synthesis, characterization, and understanding of macromolecular and supramolecular systems have led to an enormous variety and complexity in the field of soft matter science [165]. The traditional separations in terms of structure versus dynamics, crystalline versus amorphous, or experiment versus theory are increasingly overcome. As far as characterization of such materials is concerned, no experimental or theoretical/simulation approach alone can provide full information. Instead, a combination of techniques is called for and conclusions should be backed by results provided by as many complimentary methods as possible [166]. Combining scattering or NMR spectroscopy with computer simulation is well established today in the study of structure and dynamics of biomacromolecules [167]. Prominent examples of such an approach in the supramolecular field involve the combination of X-ray scattering, spectroscopy and computer simulation to elucidate the packing in newly synthesized columnar systems [168]. The versatility of magnetic resonance techniques, in particular solid-state-type NMR, in elucidating the interplay between structure and dynamics in these systems is evident from the examples provided below. Yet none of the results in the examples are based on a single technique (Fig. 47).

The methods for determining structure and dynamics of supramolecular systems based on 2D DQNMR as reviewed, e.g., in [161, 164, 169] are now widely employed in soft matter and life sciences alike. Recently, a new systematic strategy for revealing the local packing in semicrystalline π-conjugated polymers was introduced [170]. Our strategy takes advantages of a multi-technique approach in which unit-cell parameters are derived from X-ray scattering, and molecular constraints are determined from solid-state NMR spectroscopy. The parameters

derived from this strategy include the space group, which is one of the first steps in a conventional approach to solving a crystal structure, distance constraints from ^{1}H DQNMR, and chemical shifts. These experimental results are unified by quantum-chemical calculations, enabling the verification of specific packing models in silico and quantification of π-stacking effects. This approach can be compared with that employed for solution structures of biomacromolecules through distance constraints (nuclear Overhauser effect, NOE) and NMR chemical shifts [171]. This, however, requires a large number of NOE constraints, whereas in a crystalline solid the periodicity described by the space group gives access to the full 3D structure from only a few constraints. Thus, our strategy, which we propose to term "multi-technique crystallography", can be applied in general to provide quantitative insights into the packing of semicrystalline polymers with specific intermolecular packing features, such as hydrogen bonds or stacking of aromatic moieties.

Based on work at the Max Planck Institute for Polymer Research [172, 173], pulsed electron paramagnetic resonance (EPR) has experienced a remarkable revival worldwide [174]. In particular, pulsed double electron–electron resonance (DEER) spectroscopy in combination with site-directed spin labeling [175] is extensively used today in studies of the structure of proteins, including their function as carriers of small molecules, and of nucleic acids. Moreover, it is used to probe large, complex biomacromolecules and their assemblies as well as 1361 protein folding [176].

4.3 Self-Assembly and Dynamics of Polypeptides

Polypeptides, i.e., macromolecules composed of amino acids, are probably the best known example of molecular structures determined by intramolecular hydrogen bonds [177]. Resembling biomacromolecules, they are considered for use in drug delivery and gene therapy and thus have been subject of intensive studies [178]. In addition, it is known that the superb performance of biological polypeptide-based materials such as hair or spiders' silk is due to a hierarchical superstructure over several length scales, where structure control is exerted at every level of hierarchy [179]. The two most common local conformations of polypeptides, known as secondary structures, are the α-helix, stabilized by intramolecular hydrogen bonds, and the β-sheet, stabilized by intermolecular bonds. These secondary structures can be probed directly by solid-state NMR [163] and their packing can be obtained by X-ray analysis [180]. Different chain conformations can also be distinguished by simple circular dichroism (CD) measurements [177], employed in Sect. 3.3.2. In addition, the α-helical structure posts a permanent dipole moment along its backbone and can, therefore, be classified as type-A polymer in Stockmayer's classification [181]. This dipole moment can be measured precisely using dielectric spectroscopy (DS) and can be used as a probe of the persistence length of the secondary structure [182]. Over the years, we have studied various
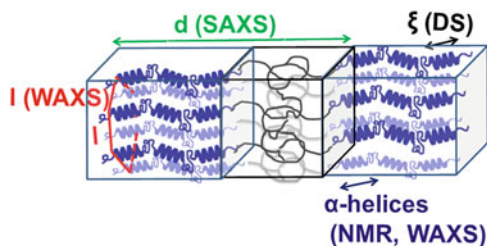
Fig. 48 Assembly of a lamellar-forming polypeptide–coil diblock copolymer depicting the main techniques employed in our studies. Small-angle X-ray scattering (SAXS) is employed for the domain spacing, d. ^{13}C NMR and wide-angle X-ray scattering (WAXS) are employed to identify the type of the peptide secondary structure (α-helical in the schematic). WAXS is further employed to specify the lateral self-assembly of α-helices within the polypeptide domain (a hexagonal lattice is indicated). Dielectric spectroscopy (DS) and site-specific NMR techniques are employed for the dynamics. Furthermore, the most intense DS process provides the persistence length, l_p, of α-helical segments [181]

polypeptides by different NMR techniques, X-ray scattering, and dielectric spectroscopy in order to better understand their hierarchical self-assembly (Fig. 48).

As shown in an extended review [181], the concerted application of these techniques has shed light on the origin of the glass transition, the persistence of the α-helical peptide secondary motif, and the effects of topology and packing on the type and persistence of secondary structures. Protein function and applications often depend on these issues. With respect to the freezing of the dynamics at the liquid-to-glass transition temperature (T_g), it was found that the origin of this effect is a network of broken hydrogen bonds. It is the diffusion of these defects along the chain that give rise to the strongly non-Arrhenius dynamics associated with T_g. Glass formation is largely independent of the presence or absence of side groups and is decoupled from the solvent dynamics. The selective probing of the α-helical motifs by NMR elucidated the geometry of the respective dynamic processes. Not surprisingly, the presence of defects in hydrogen-bonded regions also has consequences on the persistence length of α-helices. Using poly(γ-benzyl-L-glutamate), PBLG, as an example, it was shown that helices are objects of rather low persistence in the bulk as well as in concentrated solutions in helicogenic solvents [183].

Copolypeptides, on the other hand, with their inherent nanometer length scale of phase separation, provide means of manipulating both the type and persistence of peptide secondary structures. As examples we refer to the partial annihilation of α-helical structural defects due to chain stretching, to the induced chain folding of β-sheets in block copolypeptides with incommensurate dimensions, and to the destabilization of β-sheets in peptidic blocks having both secondary motifs [184–186]. These effects should be taken into account when such peptides are going to be employed in applications such as drug delivery.

Polypeptide star polymers with a large hydrocarbon core were found to exhibit several unanticipated properties. First, with the aid of a polyphenylene (see also Sect. 2) core scaffold it was shown that there is a distinct change in the

Fig. 49 Incompatible
segments, CF_2 (*yellow*),
CH_2 (*green*), and aromatics
(*red*), can be forced into
proximity by limiting
conformational freedom
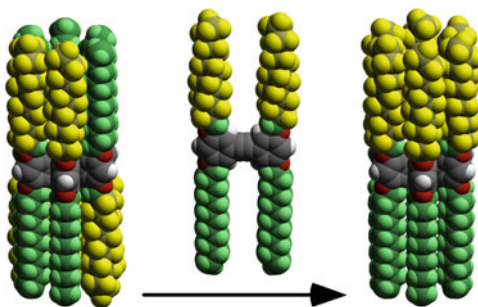
peptide secondary structure from coil/β-sheet conformations to α-helices that is
accompanied by an abrupt increase in the hydrodynamic radii. This change in
secondary structure and its consequences on the diffusion of the conjugates can
be crucial in the efficient design of multiple antigen peptides. Second, the bulk
studies revealed a strong effect of the polyphenylene core on the peptide secondary
motifs that could not be envisaged from their linear analogues. The time-scale and
the amplitude of polypeptide molecular motion could be measured by combining
dielectric spectroscopy with advanced NMR techniques [187].

Proline residues are of exceptional significance in protein conformation and
protein folding because proline is the only amino acid where the nitrogen bears no
amide hydrogen, preventing hydrogen bonding. Furthermore, the bulky pyrrolidine
ring restricts the available conformations. Therefore, polypeptides with proline
residues offer a unique possibility to unravel the interplay between hydrogen bonding
and geometric packing effects. A recent multi-technique study of diblock copolymers
of PBLG and poly(L-proline) (PLP) investigated their hierarchical self-assembly.
Both blocks possess helices stabilized solely either by hydrogen bonds (PBLG) or
by steric hindrance (PLP) and are further packed in two different hexagonal cells. An
intriguing *trans–cis* conformational change of PLP upon confinement was observed
that mimics the isomerization of isolated proline residues in proteins. These *cis*-PLP
conformations reside primarily at the PLP–PBLG interface, alleviate the packing
frustration, and permit PBLG and PLP helices to pack with their bulk
properties [188].

4.4 Polymers with Different Building Blocks

Precise 3D nanoscale morphological control of the solid state in the 5–10 nm range
using semiflexible chains is a demanding challenge [189]. The development of
strategies for increasing the intricacy within self-assembled nanostructures outside
of biology or analogous de novo examples is hindered by the ability to predict the
complex competition of intra- and intermolecular interactions at the molecular level.
With this in mind, fluorocarbon units were incorporated into polymers. This offers
ways of combining a low friction coefficient, high rigidity, extremely low surface
energy, hydrophobicity, chemical inertness, and thermal resistance, which make them
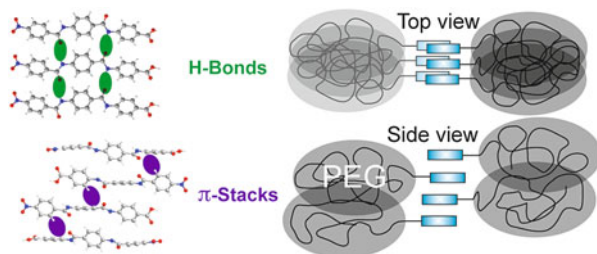
Fig. 50 Packing of rod–coil copolymers. The rigid rods are held together by intermolecular hydrogen bonds. The space between the stacks is filled by the PEG side chains adopting a Gaussian coil-like conformation

useful for a wide range of applications. Last, but not least, partially fluorinated compounds provide unique tools for tailoring self-assembly via the fluorophobic effect. In particular, in systems containing fluorocarbon/hydrocarbon amphiphiles tethered to cores with only rotational degrees of freedom, these incompatible segments can be forced into proximity (Fig. 49). The lack of sufficient conformational mobility leads to kinetically trapped phases, stabilized by favorable interactions with neighboring molecules [190, 191]. Here, ^{13}C and ^{19}F NMR both in solution and in solid state are especially informative for unraveling the self-organization.

4.5 Interplay of Undirected and Directed Interactions

Rod–coil block copolymers represent an interesting class of diblock copolymers due to their particular aggregation behavior. The interactions between various segments and geometric effects are responsible for nanoscale phase separation and liquid crystallinity. The ability to self-assemble on the nanometer length scale has promoted these systems for possible applications such as light-emitting diodes (LEDs) and organic photovoltaics and also for the preparation of nanometer-scaled architectures. Therefore, rod–coil block copolymers with an oligomeric rod segment are of particular interest because their aggregation might depend on the length of the respective building blocks [192, 193]. With this in mind, we have investigated copolymers built of oligomeric rod blocks of oligo(*p*-benzamides) (OPBA) and a poly(ethylene glycol) (PEG) coil (Fig. 50). An interesting feature of solid OPBAs is their rigidity resulting from packing due to hydrogen bonding and π–π interactions. Both are noncovalent interactions, and their influence on the structure of the studied system is not yet fully understood.

Insight into aggregation and local packing of both OPBAs and OPBA-based rod–coil copolymers can be obtained from advanced high-resolution solid-state NMR. It was found that longer OPBAs form hydrogen-bonded layered β-sheet-like aggregates, which are remarkably stable and apparently reflect an equilibrium structure [194]. This structure is retained after PEG attachment, forming a rod–coil

Fig. 51 Helical BTA stacks: (**a**, **b**) CO-centered and (**c**, **d**) N-centered. The tilted stacking leads to a splitting of the CH signals in ¹H MAS NMR spectra, as indicated by the NICS maps (**e**, **f**) [197]
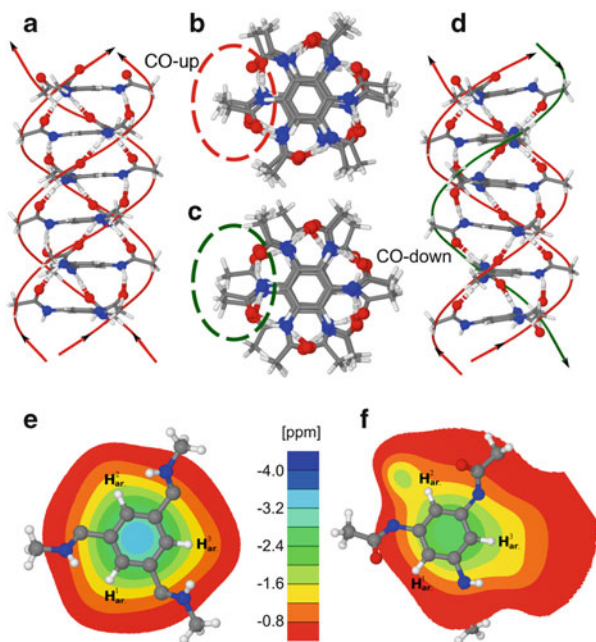
copolymer. At 59°C a transition to a LC phase of the rod–coil copolymer is observed by DSC. From solid-state NMR studies, this has been ascribed to melting of the PEG coil, where the aggregates of the OPBA rods are preserved. Because of the pre-organization in the LC phase, an improvement of the local order is observed for the OPBA rods in the copolymer.

C3 symmetric benzene-1,3,5-tricarboxamides (BTAs) are known to form helical supramolecular assemblies with columnar mesophases [195]. The driving forces for self-organization can vary from system to system despite equivalent, hydrogen-bonding central building blocks [195]. Solid-state NMR combined with X-ray scattering, optical spectroscopy, and computer simulation provides insight in the subtleties of the organization of the moieties [196]. When three bulky side groups, such as 3,3′-diamino-2,2′-bipyridines, are attached to BTAs, the self-assembly of the disk-like molecules is mainly driven by steric interactions between neighboring molecules, where surprisingly hydrogen bonding along the columns has almost no influence on the final supramolecular structure. This results in a complicated helical arrangement with a pitch angle between 13° and 16°, in accord with quantum chemical calculations. In contrast, in BTAs with short chiral, aliphatic side chains, the supramolecular organization sensitively depends on the local hydrogen bonding. Unlike the common symmetric co-planar helical arrangement of carbonyl-centered BTAs found in supramolecular polymers in gels (Fig. 51a, b), NH-centered BTAs adopt an asymmetric helical arrangement in the solid (Fig. 51c, d) [197].
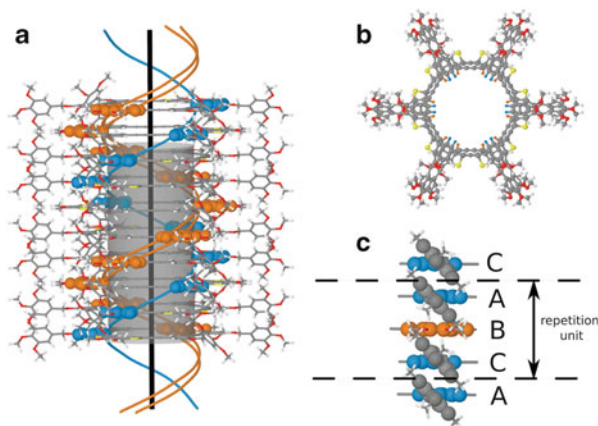
Fig. 52 a) Sketch of empty helical stacks formed by shape-persistent macrocycles. b) A pitch angle of ≈60° between adjacent macrocycles was determined from 2D double quantum NMR correlation spectra in agreement with NICS maps. c) Side-chain packing [201]

Supramolecular organization is also able to create tubular molecular structures [198, 199]. Tube stabilization utilizing strong bonds, e.g., by metal–ligand interactions or by surfactant-templated synthetic procedures, leads to fixed structures in the final material. To generate more flexible tubes one can take advantage of dissipative forces. A recent example is the self-assembly of shape-persistent low symmetry arylene-ethynylene-butydiynylene macrocycles into flexible molecular channels, with dissipative forces between aromatic moieties with different electron affinities [200]. From solid-state NMR experiments combined with chemical shift calculations it was possible to show that the channels are indeed empty [197]. The decisive role of the length of the dendritic side chains was unraveled, as well as the formation of a six-membered ring with weak intra-molecular contact involving a proton site on an aromatic group of the group and a flexible ethylene oxide linker of the side group. The formation of a LC phase then leads to the immediate and controllable formation of self-repairing nanochannels. These channels have an inner diameter of well over 1 nm in the LC phase. The channels are further stabilized by a helical arrangement, with a pitch of about 60° between individual macrocycles as identified from ^{1}H solid-state NMR experiments and NICS calculations (Fig. 52). Such artificial channels can function as size-selective or even as molecular-selective pores for chemical sensing or directed transport of nanosized objects [200, 201].

In addition to the structure of supramolecular objects, the dynamics of the building blocks themselves or molecules trapped in cages and channels is of great importance [166, 202]. For instance, the guest dynamics of dimeric capsules of tetratolyl urea calixarene filled with different aromatic guests such as benzene, fluorobenzene, and 1,4-difluorobenzene was studied. Upon inclusion, all guest moieties exhibit

complexation-induced chemical shifts varying from 3 to 5 ppm. All guest molecules undergo distinct motions, ranging from mere C_6-rotations of benzene at low temperatures to rather ill-defined 180° phenyl flips of fluorobenzene. In addition, by combination of both computed NICS maps and explicit ^{19}F and ^2H ab initio chemical shift calculations by density functional theory, the preferred orientation of the guest molecules within the host was derived. Although benzene populates the center plane formed by the stabilizing hydrogen bonds of the urea units, fluorobenzene prefers an equatorial position. In the case of 1,4-difluorobenzene, an axial position is suggested. Off-centered orientations towards the "walls" of the host, however, can be safely ruled out [203].

4.6 Columnar Structures from Discotic Liquid Crystals

The disk-shaped polycyclic aromatic hydrocarbons (PAH) form π-stacks and are currently of broad scientific interest due to their potential application as conducting molecular wires [204]. Charge mobility can occur parallel to the stacking axis. Critical for the charge-carrier properties are disk size, shape, and periphery [205]. We have studied two such disk-shaped molecules that form molecular wires in their crystalline and LC phases. We determined the packing and specific molecular dynamics of the disks, including the intriguing kinetics of self organization and self-healing.

The most prominent examples of such molecular π-stacks are based on hexa-peri-hexabenzocoronenes (HBC) [160, 204]. Here, the kinetics of phase transformation from the high temperature discotic liquid crystalline mesophase to the crystalline phase at lower temperatures has been studied in a model dipole-functionalized HBC derivative. Complementary structural (X-ray diffraction, solid-state NMR) and dynamic (solid-state NMR, DS) methods were employed. These experiments revealed long-lived metastability, slow kinetics, as well as an intermediate state that involves a change in unit cell prior to crystallization. The barrier properties for the unit cell transformation and crystallization amount to 1 and 2.5 eV, respectively. Although crystallization bears some similarity to nucleation and growth, the LC to crystalline transformation is more complex and involves fractional exponents. In addition, the selective probing of the alkyl chains and disk dynamics by NMR allowed identifying the role of the latter on inducing crystallization [206].

Among the different discotic liquid crystals, perylenediimide (PDI) derivatives have received considerable attention, originally because of their industrial applications as pigments. Efforts to optimize pigment colors resulted in high-grade industrial applications including automotive coatings [207]. These applications made use of the high tinctorial strength, light and weather stability, insolubility, and chemical inertness of PDIs. Other major applications of PDI derivatives are as organic electronics in all-organic photovoltaic solar cells and field-effect transistors. These applications rely on the high charge carrier mobilities that made PDI the best n-type semiconductors available to date [208]. Central to these applications of HBCs
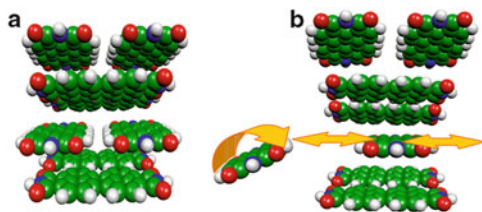
Fig. 53 Drawing of the PBI columns as revealed from solid-state NMR and computer simulation. (**a**) Tetramer motif stacking into columns. (**b**) Molecular reorganization: One PDI leaves the columns, flips over, and enters a column again [210]

and PDIs is their ability to organize efficiently in different packing motifs and, in particular, their degree of intra- and intermolecular order. The degree of structural perfection strongly affects their properties (absorbance, fluorescence, and charge transport) and results in applications in organic field-effect transistors, light-emitting diodes, and organic solar cells.

In a systematic investigation of the self-assembly, dynamics, and kinetics of phase formation of donor–acceptor substituted perylene derivatives, the role of the strong dipole associated with the diphenylamine-functionalized perylenemo- noimides molecules was elucidated. The close packing manifested itself in strong heteronuclear dipolar couplings, which were exploited in solid-state NMR. The structural investigation revealed that the self-assembly and thermodynamic properties of perylene derivatives are significantly different from those of the corresponding HBC compounds. Perylenes, with a small π–π overlap, form a crystalline phase as well, but the residues do not tilt with respect to the columnar axis. Because such a tilt is absent in perylenes, the intercolumnar thermal expansion is always positive, being similar to the intracolumnar thermal expansion. This constitutes a primary difference between the self-assembly motifs of the crystalline phase of perylenes and those of the HBCs. The phase formation involves a delicate balance of short-range interactions and packing. Our results suggest that branched chains substituted away from bay positions are important as space-filling agents within the alkyl domains for the formation of the crystalline phase.

The solid-state NMR experiments unraveled the role of intramolecular hydrogen bonding in stabilizing the crystalline phase as well as the influence of non-hydrogen- bonded moieties on the twist angle between successive monomers [209].

With respect to the dynamics, both solid-state NMR and DS revealed a relatively immobile core within the crystalline phase. Perylene derivatives that do not crystal- lize undergo an isotropic liquid-to-glass transformation at a temperature that was found to depend on the number of methylene units in the alkyl chains. The phase transformation kinetics from the high temperature isotropic phase to the crystalline phase at lower temperatures revealed a long-lived metastable state as a result of the soft potential. The crystalline phase is formed via nucleation and growth. The transformation kinetics is controlled by the nucleation barriers. The existence of slow molecular dynamics and of very slow phase transformation suggests that care should be taken in establishing the equilibrium phases of discotic liquid crystals.

Furthermore, these issues could influence the charge carrier mobilities that are required for applications as photovoltaic solar cells and field-effect transistors [209].

This is indeed the case for perylene bisdiimides (PBI) functionalized with dendritic goups. These dendronized PBIs self-assemble into a complex helical column generated from tetramers containing a pair of molecules arranged side-by-side and another pair in the next stratum of the column, turned upside-down and rotated around the column axis at an intratetramer angle that is different from that of the intertetramer angle (Fig. 53). In most cases, the intratetramer stacking distance in this column is 4.1 Å, while the intertetramer distance is 3.5 Å. The architecture of this complex helical column, the structure of its 3D periodic array, and its kinetically controlled self-organization with such a long intrateramer distance are not ideal for the design of supramolecular structures with high charge carrier mobility. In fact, the mobility of electrons is only moderate. However, in some cases heating above 100°C into the LC phase optimizes the packing, resulting in shorter intertetramer distances and much higher charge mobilities [210], This is accompanied by substantial narrowing of the ^{1}H NMR lines. Computer simulation showed that this narrowing of the NMR spectra indicates a complex reorganization mechanism, where the PBI molecules leave the supramolecular column, flip over, and reenter a column at a later time (Fig. 53) [210].

4.7 Conclusions

The examples briefly reviewed here demonstrate that the interplay of synthesis, multi-technique characterization and computer simulation is crucial for the development of functional materials based on supramolecular organization of carefully designed building blocks. Local conformation, intrinsic mobility, incompatibility, and well-established noncovalent interactions such as hydrogen bonds or π–π interactions can govern self-assembly in highly specific ways. Moreover, complex molecular dynamics is relevant for generating stable structures with desired properties such as high charge carrier mobility. In contrast, ill-defined sample preparation can lead to partially disordered structures with inferior properties. Magnetic resonance, both NMR and EPR, can provide unique detailed information about all these aspects over large ranges in space and time. Therefore, these techniques play an important role in the generation of functional organic materials.

5 Block Copolymers and Confinement

This section deals with the influence of amphiphilicity on the formation of block copolymer structures. These block copolymers are either confined in the spherical shape of a nanodroplet or on a surface. Whereas in the first case, the fundamental aspects of mesoscospic structure formation are the focus of attention, we concentrate in the second case on a specific function, i.e., switchable wettability due to the

in-chain attachment and self-assembly of a block copolymer on a surface. As a third example we describe the inverse effect: vesicles formed by block copolymers and dispersed in aqueous medium confine quantum dots in the hydrophobic interior of the lamellae.

5.1   Diblock Copolymers Confined in Miniemulsion Droplets

As a first example, we consider block copolymers confined in droplets as obtained by the miniemulsion process. It is well known that block copolymers self-assemble into periodic nanostructures such as lamellae, hexagonally coordinated cylinders, cubic lattices of spheres, and the gyroid morphology [189, 211]. This phase behavior can be adjusted by different parameters such as temperature or the chemical composition [212, 213]. Block copolymers have been investigated extensively in bulk. The influence of a 2D or 3D confinement on the sub-100-nm scale has, however, only been examined in a limited way. In the 2D confinement of a film, a deviation of the lamellar thickness from the value of the bulk material is induced [214]. By confining a block copolymer in a porous silica matrix, both cylindrical and lamellar structures were observed [215]. Electrospinning and subsequent annealing of the obtained fibers also lead to cylindrical structures [216]. Onion-like block copolymer morphologies were obtained in spherical particles using spray coating [217]. Using emulsion techniques and subsequent solvent evaporation techniques, onion-like particles from poly(styrene-*b*-isoprene) and poly(styrene-*b*-methyl methacrylate) (PS-*b*-PMMA) were created [218]. Lamellar, hexagonal, and bicontinuous phases in nanoparticles could be realized with a triblock copolymer [219].

Nanoparticles consisting of different molecular weight PS-*b*-PMMA copolymers and nanocapsules made of the same copolymers, but additionally with hexadecane as liquid core material, were prepared by using a combined miniemulsion and solvent evaporation technique [220]. The morphology of block copolymer assemblies was investigated in dependence of the nanoconfinement. We introduced two nanoconfinement parameters: the diameter D of the droplet throughout the synthesis and the shell thickness δ of the nanocapsules with a liquid as core. D was controlled by varying the concentration of the surfactant in the miniemulsion, while δ was controlled by the ratio of hexadecane to copolymer.

For the investigation of the influence of the molecular weight of the polymer on the morphology of the block copolymer, we used PS_{76}-*b*-$PMMA_{79}$ and PS_{838}-*b*-$PMMA_{945}$, where the numbers correspond to the average numbers of units of styrene and methylmethacrylate [221].

For the formation of solid copolymer nanoparticles without a liquid core, PS-*b*-PMMA was used as a model system. In order to be able to form nanoparticles, the block copolymer was dissolved in chloroform and the solution was miniemulsified in water by adding the SDS. In this case, homogeneous droplets were formed. After evaporation of the chloroform, nanoparticles consisting entirely of block copolymer
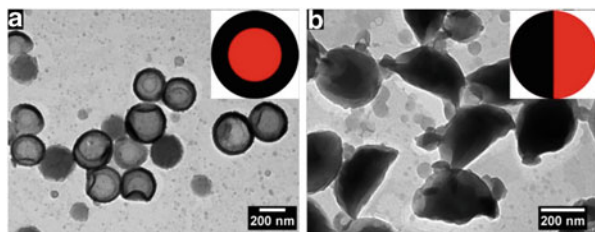
Fig. 54 TEM micrographs of nanoobjects made of PS$_{838}$-b-PMMA$_{945}$ and hexadecane (ratio 1:1) with increasing amount of SDS. Their morphology changes from (**a**) nanocapsule (low coverage of SDS, 0.67 wt%) to (**b**) a Janus-like structure (high coverage of SDS 3.33 wt%). The *insets* represent the morphology in aqueous phase with the copolymer (*black*) and hexadecane (*red*); the latter is evaporated in the electron microscope and therefore not visible on the TEM micrograph [221]. Reproduced by permission of The Royal Society of Chemistry

were obtained. Phase separation of the block copolymer took place during solvent evaporation.

Nanocapsules consisting of the block copolymer as shell and with a liquid as core could be obtained by adding hexadecane, which is a nonsolvent for the copolymer. The block copolymer was dissolved in a mixture of chloroform and hexadecane. During evaporation of the chloroform there is a phase separation of the block copolymer and the hexadecane, and a microphase separation of the block copolymer itself. For the successful formation of nanocapsules, the interfacial tensions for the polymer/water and water/hexadecane interfaces are important.

The presence of the surfactant SDS influences nanocapsule formation in two ways: With increasing SDS concentration, the nanocapsules become smaller. At the same time, with decreasing size of the nanocapsule, the coverage of the nanoobjects (before evaporation of the solvent, the nanodroplets; after the evaporation, the nanoparticles or nanocapsules) by SDS increases, leading to a decrease in the interfacial tension of droplet/water and copolymer/water. The interfacial tension between copolymer and water (≈ 0.035 N/m) without surfactant is considerably smaller than the interfacial tension between hexadecane and water (≈ 0.054 N/m). Thus, in the case of a low concentration of SDS and subsequent coverage of the nanoobjects by SDS, the interfacial tension of the copolymer/water interface is lower than that of the hexadecane/water interface; therefore as the thermodynamically most stable structure, nanocapsules are expected to be formed (Fig. 54a).

In the case that the concentration of SDS is high enough to give full coverage of the interfaces with surfactant, there are similar interfacial tensions for the polymer/water and hexadecane/water interfaces and Janus-like particles consisting of PS-b-PMMA and liquid hexadecane are formed in the aqueous phase. After drying (and therefore complete removal of the liquid hexadecane), a half-spherical morphology is obtained as verified by electron microscopy (Fig. 54b). Please note that in this case, the copolymer is seen as one phase.

The size of the nanoparticles and nanocapsules can be controlled by varying the amount of SDS in the miniemulsion process. For solid nanoparticles using the block copolymer PS$_{838}$-b-PMMA$_{945}$ without hexadecane, the diameter decreases with
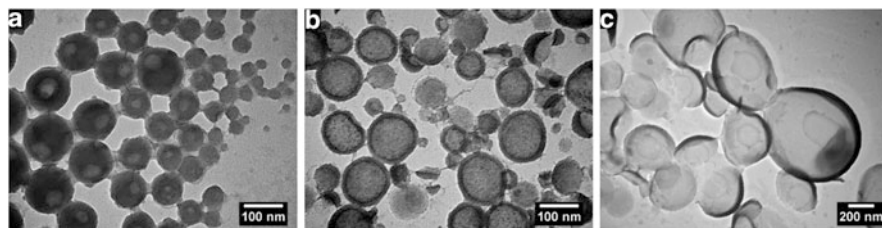
Fig. 55 TEM micrographs of capsules consisting of PS$_{838}$-*b*-PMMA$_{945}$ with increasing amount of hexadecane to copolymer: (**a**) 0%, (**b**) 40%, and (**c**) 80%. The SDS concentration was constant at 0.67 wt% compared to the dispersed phase. The capsules become more unstable as the wall thickness decreases with increasing amount of hexadecane [221]. Reproduced by permission of The Royal Society of Chemistry

increasing amount of surfactant (0.17–3.33 wt% compared to the dispersed phase) from about 250 nm down to 80 nm. For the nanocapsules with the same block copolymer, but additionally with hexadecane, the diameter of the nanocapsules was in the range of 470 nm (for the lowest amount of surfactant of 0.17 wt%) down to 200 nm (with a high concentration of SDS of 3.33 wt%). For the lower molecular weight block copolymer PS$_{76}$-*b*-PMMA$_{79}$, a decrease of the diameter from about 260 to 100 nm upon the same increase in SDS was observed. Since the diameter of the droplet determines the size of the particle or capsule obtained after solvent evaporation, the particle diameter is directly related to the amount of surfactant. For PS$_{838}$-*b*-PMMA$_{945}$, the average wall thickness varies between 68 and 20 nm and for PS$_{76}$-*b*-PMMA$_{79}$ between 36 and 12 nm (Fig. 55). A thinner shell leads to unstable capsules that easily collapse. The theoretical wall thickness is in good agreement with the observed wall thicknesses.

After having evaluated the structure of the nanoobjects and considering the copolymer as one phase, the microphase structure of the copolymer within the nanoparticles and nanocapsules can be elucidated. The theoretical lamellar thickness L_0 of PS-*b*-PMMA can be calculated for PS$_{76}$-*b*-PMMA$_{79}$ to be 13.1 nm and for PS$_{838}$-*b*-PMMA$_{945}$ to be 64.4 nm. For PS$_{76}$-*b*-PMMA$_{79}$, the product χN having a value of 6.5 is in the weak segregation limit. Therefore, no well-defined lamellar structures were expected for the low molecular weight PS$_{76}$-*b*-PMMA$_{79}$. In contrast, for high molecular weight PS$_{838}$-*b*-PMMA$_{945}$, the product χN equals 71 and the polymer is located in the strong segregation limit. A lamellar morphology is expected. When confined to spherical nanoparticles, this corresponds to an onion-like morphology. In cross-section cuts of stained particles in an epoxy matrix, this onion-like structure was indeed observed (Fig. 56e, f) using no hexadecane and low surfactant concentration. The lamellar thickness was 60 nm, in good agreement with the theoretical value of 64.4 nm. Because PMMA possesses a slightly lower interfacial tension with water than PS, it is expected that PMMA forms the outer layer. The XPS survey spectra revealed, as expected, only the elements carbon and oxygen. In addition, sulfur was found, but in low concentrations of less than 0.4 atomic %. High-resolution scans over carbon and oxygen were performed to determine the experimental oxygen/carbon ratio from which the molar PMMA

Nanocapsules with hexadecane

Nanoparticles without hexadecane

$C_{surfactant}$
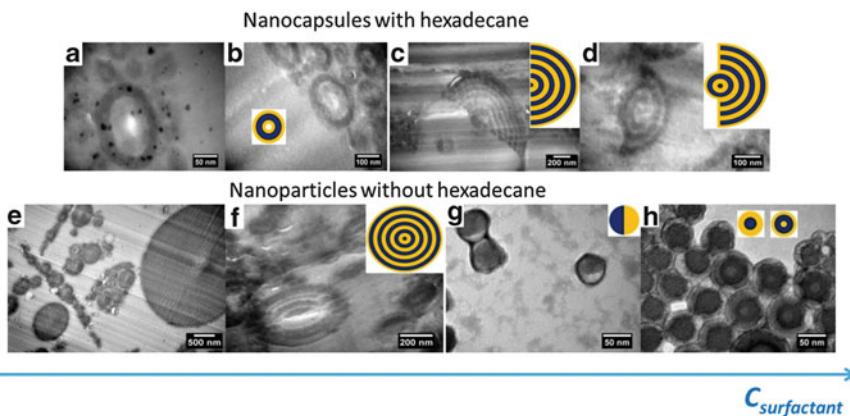
Fig. 56 Final structure of nanoparticles (without hexadecane) and nanocapsules (with hexadecane) obtained with PS$_{838}$-b-PMMA$_{945}$ after evaporation of hexadecane. The copolymer is in the strong segregation limit; PS (blue), PMMA (yellow). (**a**, **b**) Nanocapsules with hexadecane and low surfactant concentration show an onion-like morphology in cross-section cuts. (**c**, **d**) With hexadecane and high surfactant concentration, an onion-like structure is obtained at the geometrical center of the original Janus-like nanoparticle of hexadecane and polymer. In the outer regions, a bent structure is observed, which we attribute to volume conservation effects. (**e**, **f**) Without hexadecane and at low surfactant concentration, TEM micrographs show a lamellar structure in cross-sections of both large and small nanoparticles with good agreement between measured and theoretical layer thickness. (**g**) For higher concentrations of surfactant and therefore smaller nanoparticles, Janus-like block copolymer nanoparticles are obtained with diameters below the theoretical layer thickness. (**h**) For slightly larger nanoparticles, core–shell and onion-like morphologies form. Figure modified from [221]. Reproduced by permission of The Royal Society of Chemistry

surface concentration can be determined. For the onion-like particles, the surface consists of 87.1% PMMA.

For nanoparticle diameters below ~60 nm (higher surfactant concentrations), e.g., below the theoretical layer thickness, Janus-like particles were observed (Fig. 56g). Particles with slightly larger diameters showed a core–shell structure, and a further small increase in diameter yielded an onion-like morphology (Fig. 56h). Because these particles are small enough to be sufficiently transparent to electrons they could be directly deposited onto a carbon support for TEM. Embedding in an epoxy matrix and thin sectioning was not needed. Therefore, the contrast is high enough to distinguish PS, PMMA, and the surrounding area. In agreement with the XPS results on larger particles, PMMA is located on the outside for both core–shell and onion-like morphologies.

As for the Janus-like particles, the entropic penalty for bending the block copolymer domains is higher than the penalty for creating an interface of the PS domain with water. However, a slight increase in the diameter is sufficient for turning the Janus-like particles into core–shell particles. Core–shell particles suffer from a higher entropic penalty due the bending of the lamellae but gain interfacial energy because the PS domain is not exposed to water. The results indicate that $D \approx L_0$ represents the turning point for the conflicting energy contributions. Half-

Fig. 57 Nanocapsules of PS_{76}-b-$PMMA_{79}$ (weak segregation limit) show a structured surface in SEM and TEM images. In both cases, the small patches consist of PS, since it appears bright in the SEM and dark in the TEM. The patchy structure is also visible in TEM micrographs of stained cross-sections of (**a**) nanocapsules and (**b**) half-spherical nanoparticles and in (**c**) SEM and (**d**) TEM micrographs of nanoparticles consisting of PS_{76}-b-$PMMA_{79}$, indicating that it is not only a surface phenomenon [221]. Reproduced by permission of The Royal Society of Chemistry

spherical particles obtained from Janus-like particles of polymer and hexadecane showed an onion-like morphology at the center of the particle, whereas the outside of the particle consisted of bent lamellae.

Nanocapsules made of high molecular weight PS_{838}-b-$PMMA_{945}$ and hexadecane show an onion-like morphology (Fig. 55a, b). The PMMA located on the outside of the capsules is not visible in the cross-section cuts, but XPS measurements confirm that the surface is mainly PMMA (94.8%). Due to the elongation of the capsules during the cutting process, the exact layer thickness is difficult to estimate. However, it still corresponds well to the theoretical layer thickness of about 60 nm but no clear conclusion can be drawn about whether there is an increase in the lamellar thickness of the copolymer due to the strong double confinement in the shell.

At higher concentrations of SDS and in the presence of hexadecane, an onion-like morphology was observed at the center of the nanoparticle, whereas the outside of the nanoparticle consisted of bent lamellae (Fig. 56c, d). We attribute this to a conservation of volume of the two polymer blocks: the volume can be conserved quite easily by a slight change in lamellar thickness in the outer regions of the nanoparticle, resulting in bent lamellae. In the center of the nanoparticle, the degree

of curvature of the block layers is much higher; therefore the layers adopt an onion-like morphology to conserve the total volume.

In the case of nanocapsules consisting of low molecular weight PS_{76}-b-$PMMA_{79}$, patchy structures were observed in SEM and TEM (Fig. 57). In SEM, these patches with a diameter of 15 nm appear bright whereas they appear dark in TEM. The patchy structure is due to the weak phase separation characteristic for values of $10.5 > \chi N > 6$. The same patchy structures were also observed on the nanoparticles made of low molecular weight PS-b-PMMA. XPS measurements on nanoparticles and nanocapsules made of low molecular weight PS-b-PMMA show that both PS and PMMA are located on the surface. PMMA constitutes the main part (74.8% on nanocapsules and 77.7% on nanoparticles), which is probably due to the higher polarity of the PMMA. From the XPS measurements it can be deduced that the surface of the PS_{76}-b-$PMMA_{79}$ nanoparticles contains slightly more PMMA than PS_{76}-b-$PMMA_{79}$ nanocapsules does, whereas more PMMA is observed on nanocapsules than on nanoparticles for $P(S_{838}$-b-$MMA_{945})$. Patchy structures were not only observed on the surface of the nanoparticles and nanocapsules, but also on the inside (Fig. 57). The images show that there is no well-defined lamellar structure as observed in nanoparticles and nanocapsules made of high molecular weight PS-b-PMMA. There is an irregular sequence of brighter and darker domains, which can be assigned to PMMA and PS, respectively. Nanoparticles, half-spherical nanoparticles, and nanocapsules show this structure. Roughly, the size of these domains can be determined to be between 10 and 20 nm. They exhibit approximately the same size as the patches observed on the surface of the nanoparticles and nanocapsules with SEM and TEM. In the case of the nanocapsules, cross-sections were prepared. Therefore, the patches outside of the nanocapsules are due to cuts apart from the equator of the capsules through the capsular wall.

The examples show the influence of the confinement on polymers. Nanoparticles and nanocapsules of PS-b-PMMA with different molecular weights were prepared. Their morphology could be precisely tuned by changing the amount of surfactant and hexadecane in double confinement. Also, the wall thickness of the capsules could be controlled by the amount of hexadecane employed during formation using a miniemulsion process with subsequent solvent evaporation.

In order to better understand the experimentally observed microphase separation of block copolymers in confinement, it is instructive to consider an even simpler system theoretically. Therefore, we consider a mixture of 50% A and 50% B monomers in spherical confinement. The resulting structures depend on the interfacial tensions between the two species and the respective tensions between the monomers and the wall. One would expect a Janus-type structure, as observed in simulations of simple binary mixtures [222, 223], if the tensions towards the confining wall are equal (resulting in a contact angle of 90° according to Young's equation). Alternatively, core–shell structures emerge if one type of particle is strongly preferred and wets the wall. Sickle-like structures arise for finite contact angles of less than 90°.

Fig. 58 Mean-field density profiles obtained from self-consistent field theory simulations. A- versus B-rich domains are displayed for a blend of A- and B-homopolymers (**a**) and for AB-diblock-copolymer melts (**b**, **c**). In each case, all A-, and B-blocks contain equal numbers of monomers. Here, spherical confinement is implemented by blending either A- and B-homopolymers (**a**), or AB-diblock-copolymers (**b**, **c**) with C-homopolymers. The C-homopolymers act as a very bad solvent, thus enforcing the formation of A-, and B-rich spherical domains. In this case, the geometry of the confined polymer phases is studied in two dimensions. Whether Janus (**a**), core–shell (**b**), or onion (**c**) particles form depends on the number of monomers per block, and the interactions between different monomer species. From (**a**) to (**c**), the length of A-, and B-sequences steadily decreases; the sequences in (**a**) are roughly four times as long as in (**b**), and are about 15 times as long as in (**c**). To form Janus particles, the A–C versus B–C interactions need to be equal. To form layered structures, there has to be a significant difference

The same basic structures can be expected in melts that consist of 50% A and 50% B homopolymers (Fig. 58a) or even AB diblock copolymers (Fig. 58b). The situation changes somewhat for AB diblocks if the typical length of the polymer (as, e.g., expressed by its radius of gyration) is much smaller than the radius of the confining sphere. Now, the system is essentially forced to form additional interfaces as it can, e.g., no longer form a core–shell structure due to spatial constraints. Consequently, additional layers and onion-like structures emerge (Fig. 58c).

Finally, we would like to give a short outlook on the structure of a single homopolymer chain confined to a very small miniemulsion droplet. Advanced Monte Carlo methods [224] were applied to a simple coarse-grained model of polystyrene in spherical confinement [225]. The polymer chain becomes highly knotted once the confining droplet shrinks (e.g., by evaporation of the solvent) beyond the typical size of the polymer (in good solvent conditions) [225–227]. These simulations may hence lead the way to the synthesis of knotted and unknotted ring polymers in extremely small miniemulsion droplets when the termini of the polymer are chemically linked.

5.2 Junction-Point Reactive Block Copolymers for Surface Modification

Extending the concept of confining block copolymers at interfaces, we describe the synthesis and surface properties of a special type of diblock copolymer. These amphiphilic block copolymers are covalently attached to a surface as a consequence of a reactive moiety at the junction point of the two incompatible blocks. This block

copolymer topology results in a homogeneous, ultrathin polymer film that introduces the possibility to switch the surface polarity thermally or by contact with a solvent. The synthetic route described here for junction-point reactive block copolymers is of a general nature. The resulting materials can be used for tailoring of the surface wettability of a variety of flat surfaces and curved surfaces such nanoparticles. An important feature of this approach is that attachment to the interface is the final step of the approach, permitting the tailoring of the block copolymer structure in homogeneous solution prior to the final surface attachment, in pronounced contrast to established "grafting from" routes.

Ultrathin polymer films capable of stimuli-responsive wetting are particularly interesting because they permit reversible switching in surface properties from hydrophilic to hydrophobic and thus offer potential applications in the field of self-cleaning [228], "smart" coatings [229, 230] and also for microfluidic devices [231]. Y-shaped polymer brushes consisting of two incompatible polymer chains that are covalently linked to the surface with an in-chain anchor group have only been the subject of a few studies. The main advantage of these structures is the homogenous distribution of both incompatible polymer chains over the surface, due to the suppression of segregation processes. In the few reported approaches, these Y-shaped polymer brushes have been obtained by grafting-from [232] (attachment of a difunctional initiator to the substrate) or grafting-to [233] (grafting via junction-point functionalized block copolymers) strategies. Theoretical studies were carried out by Zhulina and Balazs [234]. Tsukruk and coworkers used carboxy-terminated PS and poly(*tert*-butyl acrylate) attached to 3,5-dihydroxybenzoic acid as an AB_2 anchoring moiety [233, 235]. Wang et al. presented a hydrosilylation grafting-to process to link block copolymers to silicon surfaces via a Si–H junction point [236]

To synthesize junction-point reactive block copolymers we combined carbanionic and oxyanionic polymerization with new bifunctional termination strategies based on tailored epoxide building units. As a precondition for the junction-point reactive block copolymers, a semicontinuous strategy for the rapid preparation of multihydroxyl functional polystyrenes has been established. It relies on the high stability of the acetal-protecting groups of the respective protected glycidyl ethers towards strong bases [237a]. The synthesis is carried out in a continuously operating microstructured reaction device for living carbanionic polymerization. The reaction is terminated with specifically tailored glycidyl ethers, followed by deprotection of the introduced end group moieties. Based on the termination with functional epoxide derivatives, a series of block copolymers bearing a single in-chain amino functionality was synthesized via anionic polymerization of styrene and ethylene oxide [237b]. By means of both a conventional and a continuous setup, living polystyrene was quantitatively end-functionalized with an oxirane (DBAG, dibenzyl-aminoglycidol; Fig. 59) prior to the polymerization of the PEO segment. The in-chain amine was conjugated with a fluorescent dye, evidencing full junction-point functionalization (Fig. 59).

As a consequence of this work, a general strategy for the synthesis of reversibly stimuli-responsive Y-shaped polymer brushes and their surface attachment has been developed (Fig. 60) [237c]. The preparation of the respective junction-point reactive block copolymers relies on a combination of carbanionic and oxyanionic
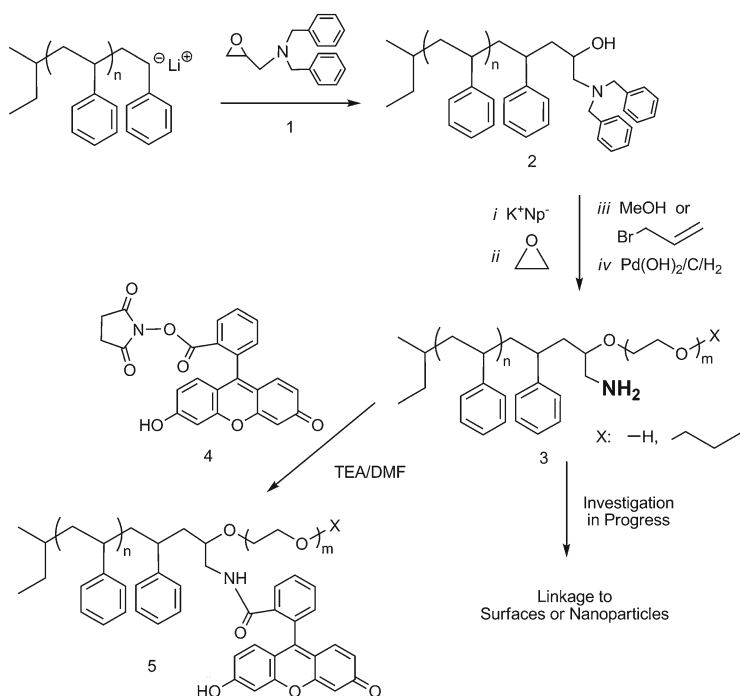
Fig. 59 Synthetic strategy for in-chain amino-functionalized, amphiphilic block copolymers with polystyrene and poly(ethylene glycol) blocks [PS-(NH$_2$)-b-PEO] via termination of the carbanionic polymerization with a benzyl-protected aminoglycidol unit (DBAG) [237b]. Numbers 1-5 refer to the compounds in the original article [237]

polymerization techniques. Allyl glycidyl ether (AGE) was utilized as an end-capping reagent for the anionic polymerization of polystyrene, achieving quantitative end-functionalization, as demonstrated by MALDI-TOF mass spectroscopy. In the next step, PS-(AGE) was used as a macroinitiator for the anionic ring-opening polymerization of ethylene oxide to afford amphiphilic PS-(AGE)-PEO block copolymers with different block ratios in the range of 6–24 kg/mol. The triethoxysilane (TEOS) anchor group for chemical grafting to silicon surfaces was introduced by hydrosilylation of PS-(AGE)-PEO leading to PS-(TEOS)-PEO (Fig. 60).

X-ray reflectivity measurements confirmed that after self-assembly and reaction of the alkoxysilyl group with the silicon oxide a 1–3 nm thick polymer layer had attached to the surface. One important issue was to clarify, whether the junction-point functional polymer was attached to the silicon surface by covalent bonds formed by the TEOS functionality, or by mere noncovalent adsorption of the PS chains at the surface. To shed light on this issue, we carried out additional deposition experiments using the allyl-functional block copolymer PS-(AGE)-PEO instead of the reactive PS-(TEOS)-PEO. X-ray reflectivity results for PS-(TEOS)-
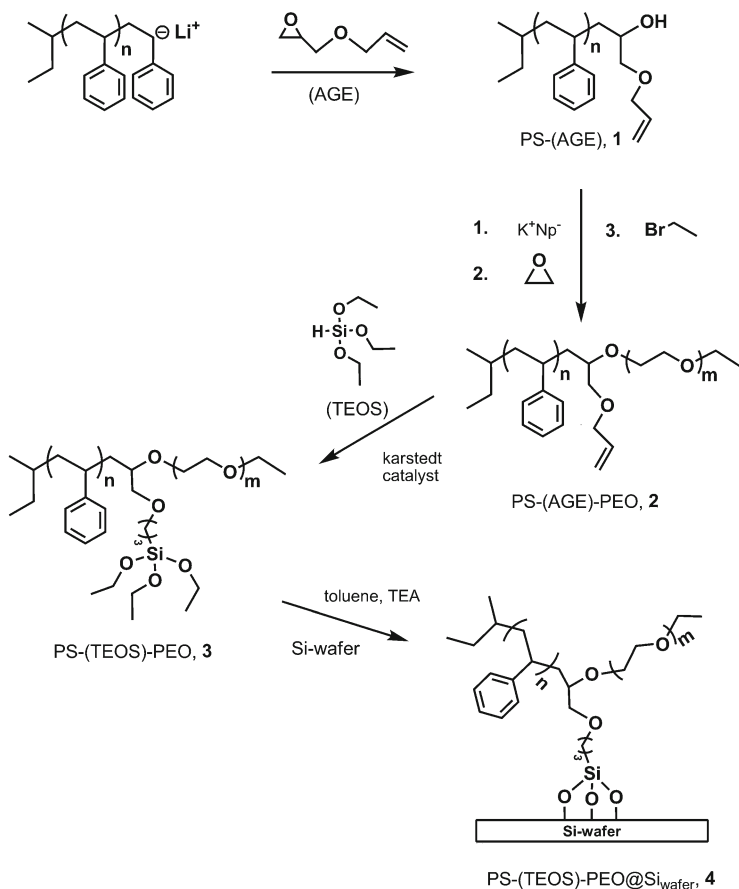
Fig. 60 Scheme of synthesis of the junction-point reactive block copolymer PS-TEOS-PEO on a silicon wafer. *AGE* allyl glycidyl ether, *TEOS* triethoxysilane, *TEA* triethylamine, K^+Np^- potassium naphthalide (see text for details) [237c]

PEO@Si$_{wafer}$ (Fig. 61a, top) showed a fringe, whereas on PS-(AGE)-PEO@Si$_{wafer}$ (Fig. 61a, bottom) no fringe was detected. This confirms that layers with the TEOS anchor group could not be rinsed away by solvents as a consequence of their covalent attachment. Without TEOS, the polymer only physisorbs and can be washed away. In addition, AFM images have been recorded (Fig. 62). Fully covered, smooth surfaces on the nanometer scale were observed. The evenly distributed hydrophilic and hydrophobic polymer chains result in a homogenous thin polymer film without any visible microphase segregation, unlike conventional mixed brushes.

Figure 61b presents images showing the contact angle and the proposed chain alignments upon thermal treatment of the surface-confined diblock copolymers. The PS chain flexibility is increased during the tempering process, and the PEO
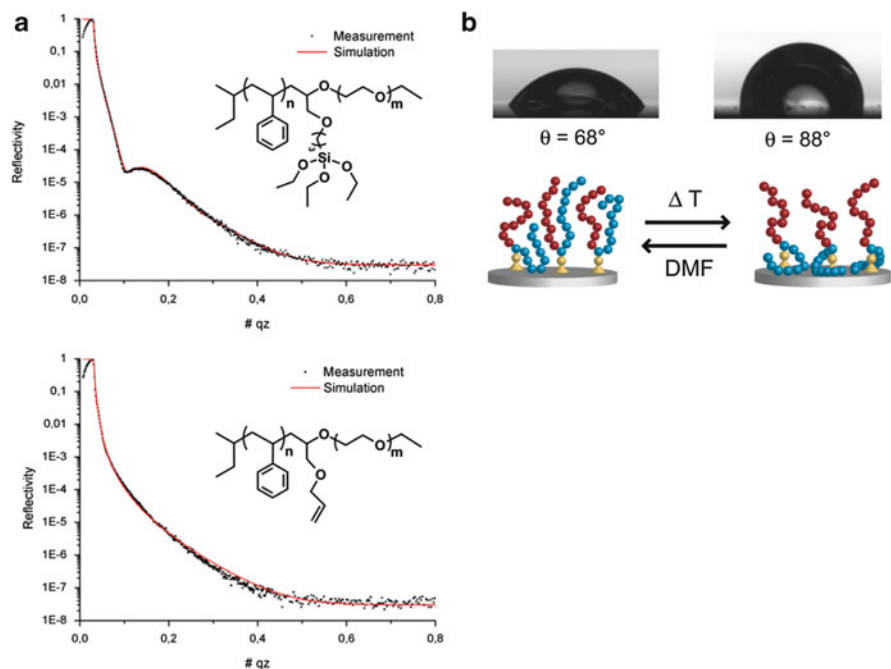
Fig. 61 (**a**) X-ray reflectivity of silicon surfaces after grafting-to process with PS_{27}-(TEOS)-PEO_{261} (*top*) and PS_{27}-(AGE)-PEO_{261} (*bottom*). A fringe could only be observed in the case of block copolymers functionalized with TEOS. (**b**) Sessile water drop on silicon surface after grafting-to process with PS_{27}-(TEOS)-PEO_{261}, after tempering and treatment with DMF under reflux. A contact angle change of 20° was observed. The scheme shows PS (*red*) and PEO (*blue*) chain alignment upon thermal treatment [237c]
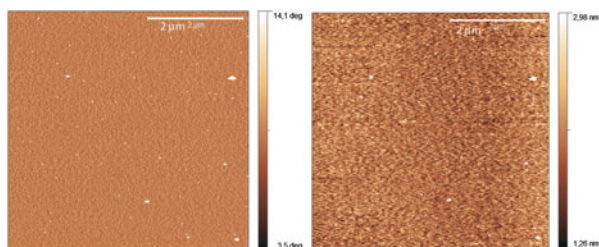
Fig. 62 AFM (**a**) phase and (**b**) height (total z range 1.7 nm) images of surface covered with surface-confined junction-point reactive block copolymer PS-(TEOS)-PEO

chains are able to segregate on the hydrophilic substrate. This tempering results in a stratification of the polymer film, with PS on the topmost layer and with a PEO layer segregated on the silicon surface as indicated by the water contact angles of 84–88°. An analogous preference for PS over PEO towards the free surface was observed for PS-PEO diblock copolymers [240]. This is caused by the lower surface tension

of PS of 36 mN/m rather than 44 mN/m for PEO. Reversible switching of surface properties was realized by repeated solvent treatment. DMF turned out to be a suitable polar solvent, which may be related to its high boiling point of 153°C, roughly 50°C above the T_g of PS. The samples were deposited in DMF under reflux and subsequent contact angle measurements showed a decreased contact angle of 68°, indicating a regression of the mixed polymer brushes at the topmost layer, similar to the initial state.

In summary, the surface wetting shows reversible stimuli-responsive behavior when applying external stimuli (e.g., temperature and solvent), as observed via contact angle measurements. A contact angle shift of up to 23° from 61° to 84° and vice versa was observed after heating and DMF treatment, respectively (Fig. 61b).

The role of the pre-organization of the amphiphilic block copolymers in solution prior to the surface attachment, the potential of the materials with respect to achievable film thicknesses, and larger contact angle changes to switch wettability are further intriguing issues based on the structural principle of amphiphilic junction-point reactive block copolymers. In addition, hydrolytic crosslinking of the TEOS moieties in organized solution structures, such as block copolymer vesicles (cf. Sect. 5.3) at the interface may be employed to stabilize "polymersome"-type assemblies. At present, the concept of junction-point reactive block copolymers is extended to other amphiphilic block copolymers with potential use for self-cleaning, anti-fouling, and friction-reducing ultrathin polymer layers.

5.3 Nanoparticles Confined in a Polymersome Shell Layer

Amphiphilic block copolymers self-assemble in selective solvents such as water. Depending on parameters like overall average molecular weight, volume fraction of each block, or effective interaction energy between monomers in the blocks, vesicles with a bilayer shell and a solvent interior volume similar to liposomes are formed. They are often called polymersomes [241]. Such polymersomes in aqueous media have attracted increasing interest due to their enhanced stability compared to classical liposomes and due to the potential to control vesicle properties like bilayer thickness, permeability, or surface functionalities by appropriate chemical copolymer adjustment [242].

The block copolymer polybutadiene-*block*-poly(ethylene oxide) (PB-*b*-PEO) is frequently studied because it offers several advantages [243–246]. For example, the PEO that forms the outer part of the assembled structures in water is generally regarded as biocompatible [247, 248]. Furthermore, depending on the PB block length, the assembled polymersomes can exhibit a thicker hydrophobic membrane core and therefore higher stability compared to liposomes [249]. Additionally, this copolymer features the possibility to crosslink the PB part and thereby stabilize the assembled structure [250–252].

Amphiphilic block copolymers have been suggested as drug carriers. The concept of drug delivery is based on successful encapsulation of substrates with

different solubility parameters. Micellar structures are favored in the case of hydrophobic substrates solubilized within the hydrophobic core of the micelle [253, 254]. Hydrophilic substrates are typically encapsulated by solubilization within the water-filled cavity of liposomes or vesicles. Several block copolymers have been used, including PB-*b*-PEO [255, 256]. The hydrophobic encapsulation into the vesicle shell of various polymers has been reported recently [257–263], but most of these works address the interface by simply utilizing the amphiphilic substrate itself [264–266]. However, it has not yet been possible to verify the full hydrophobic nature of the encapsulation, especially in the case of colloidal substrates.

Considering potential pharmaceutical applications, encapsulation of different substrates at the same time is demanded but is also a scientific challenge [267]. The polymersome system presented here offers the possibility for encapsulation of both hydrophilic and hydrophobic substances at the very same time in the very same polymersome. Potential loading systems are typically limited by the lack of suitable characterization methods. We utilized fluorescence correlation spectroscopy (FCS) in combination with cryogenic TEM imaging and DLS to characterize hydrophobic loading.

In order to understand the influence of different molecular parameters on structure formation and stability, we report on the directed encapsulation of two hydrophobic model substrates inside the polymersome shell. The system both complies with requirements like water insolubility and has sufficient fluorescence intensity for monitoring. Fluorescent CdSe/CdS/ZnS core–shell quantum dots (QDs), which carry hydrophobic surface ligands, serve as a model substrate of the nanosize regime (core size approximately 6 nm). Nile Red, a lipophilic fluorescent dye, represents the molecular size regime [268–270].

Polymersome dispersions were produced following two different routes, the cosolvent method and the rehydration method:

- In the cosolvent method, small polymersomes with a narrow size distribution were obtained starting with a copolymer solution in THF and dropwise addition of water. Controlled by a syringe pump, the dropping velocity of water addition was set to 9.9 mL/h. At approximately 30 wt% THF, the addition of water was stopped and the THF evaporated over 2–3 days. Standard final polymer concentration was around 1 g/L in water. The samples were filtered through 0.45-μm filters before proceeding. Nile Red loading of those polymersomes was achieved by the addition of dye to the starting copolymer/THF solution with different dye/copolymer weight ratios. Further treatment was done the same way.
- Employing the rehydration method, huge polymersomes with broad size distribution were obtained starting with a copolymer solution in THF or chloroform and creating a film in a Teflon vessel. After film drying at 50°C under vacuum, water was added. Film rehydration was supported by intense ultrasonic use and an elevated temperature of 50°C. The dispersions were filtered through 5 μm filters before proceeding. For DLS and FCS, additional filtration through 0.45-μm filters was used to remove dust and larger structures. QD loading of
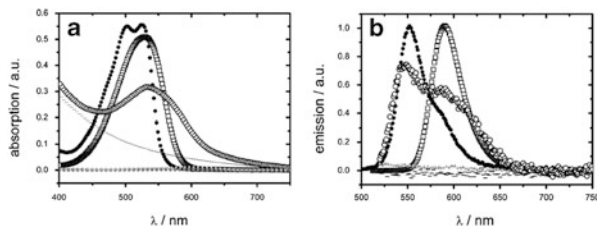
Fig. 63 (**a**) Absorption and (**b**) emission spectra of Nile Red in THF (*squares*), Nile Red-loaded polymersomes (*circles*), blank polymersomes (*dashed line*), blind samples with no copolymer (*dark gray dots*), blind samples with just PEO polymer with molecular weight of approximately 3,500 g/mol (*light gray dots*), and Nile Red in polybutadiene (*black dots*). From [269]

polymersomes was achieved by the addition of QDs to the starting copolymer/ chloroform solution at a QD/copolymer weight ratio of 1/2.8, corresponding to a molar ratio of 1/600. To load polymersomes with Nile Red, the dye was added to the starting copolymer/THF solution at a dye/copolymer weight ratio of 1/20. The rehydration procedure was performed as described above.

In order to study the potential influence of the surrounding polarity on the optical properties of an encapsulated hydrophobic dye, the hydrophobic dye Nile Red was employed to load vesicles via the "cosolvent method" starting from a solution of PB-*b*-PEO copolymer and Nile Red in THF and dropwise water addition as described above. This leads to homogeneously colored polymersome solutions with average hydrodynamic radii in the range of 40–50 nm. Typically, 500–550 dye molecules are taken up per vesicle, as determined from absorption spectra after calibration with Nile Red solutions in polybutadiene. This corresponds to an uptake of 3 mg of Nile Red per 1 g of copolymer. Blank polymersome samples without Nile Red were prepared the same way. DLS measurements showed no differences in size or size distribution of the polymersomes with or without Nile Red. Cryogenic TEM images proved the vesicular structure for both cases. Analogous to the Nile Red-loaded polymersomes, blind samples with no copolymer or with just PEO polymer with molecular weight of approximately 3,500 g/mol were prepared. Figure 63 shows absorption and emission spectra for the samples.

For $\lambda < 500$ nm, the polymersome samples scatter light increasingly with decreasing wavelengths due to their particle size (see blank polymersome sample). The two blind samples with no copolymer or just PEO show no absorption or emission signal, respectively, thereby indicating no Nile Red uptake. In none of the samples could a fluorescence band at $\lambda_{max} = 660$ nm originating from NR in aqueous environment be found [272]. The emission maximum of Nile Red in the vesicle is very close to the value found for Nile Red in a PB film (Fig. 63b), indicating its incorporation into the PB shell. As suggested by comparison with the Nile Red emission in THF, the increased emission intensity in the polymersome at around 600 nm might be attributed to traces of THF remaining in the hydrophobic shell from preparation. More likely are contributions of Nile Red molecules located close to the hydrophobic–hydrophilic interface.
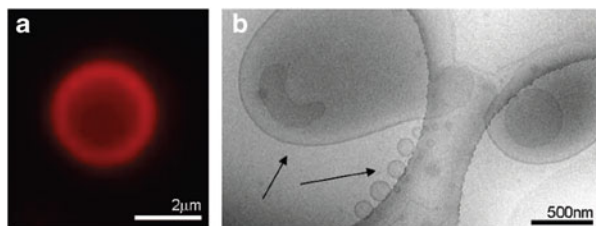
Fig. 64 (**a**) Fluorescence microscopy image of Nile Red-loaded polymersome in aqueous solution and (**b**) cryogenic TEM image of the same solution with its broad size distribution (*arrows* mark huge and small polymersomes). From [269]
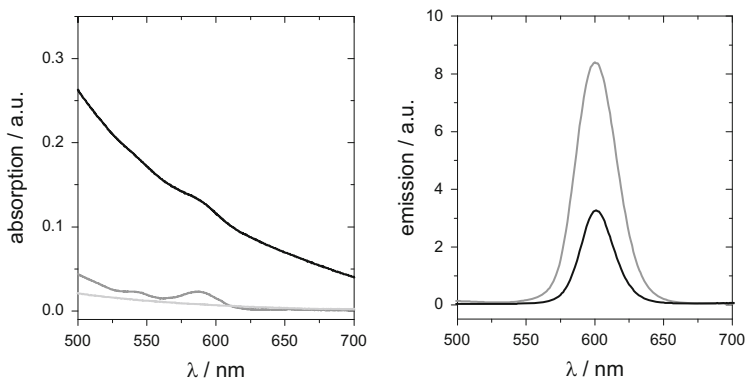
Fig. 65 Absorption (*left*) and emission (*right*) spectra of QD-loaded polymersomes: QD-loaded vesicles via rehydration method (*black line*), QDs in chloroform (*dark grey line*), and blank polymersome solution (*light grey line*)

For further investigations, starting from a dried copolymer and Nile Red film as described above, Nile Red-loaded polymersomes were prepared via the rehydration method. This method leads to vesicles with very broad size distribution and diameters ranging from 60 up to 3 μm. We imaged the fluorescently labeled polymersomes by fluorescence microscopy. Figure 64a shows the image of a Nile Red-loaded polymersome with a size of about 3 μm. The high fluorescence intensity at the outer shell supports the model of hydrophobic loading into the polymersome shell and the unloaded, water-filled core. The exact position inside the inner membrane core of the shell or at the hydrophobic–hydrophilic interface cannot be determined here.

Polymersomes with diameters smaller than 2 μm appear as nearly homogeneously fluorescing spots due to resolution limits of the microscope. Cryogenic TEM imaging of the very same solution showed vesicles over the full size distribution (Fig. 64b). In cryogenic TEM imaging, vitrified water films are typically 100–200 nm thick. Huge polymersomes with diameters of several micrometers lie only partly in those films and can therefore distort from their spherical shape in solution, as obvious in Fig. 64b.
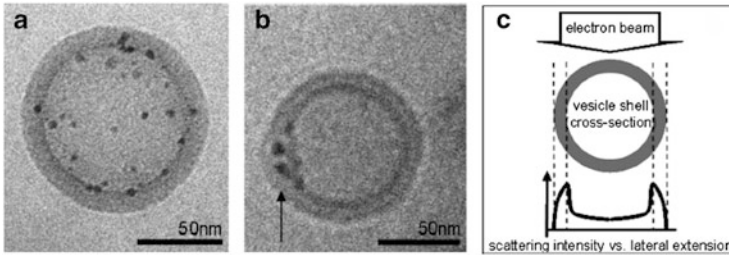
Fig. 66 (**a**, **b**) Cryogenic TEM images of QD-loaded vesicles (prepared via rehydration method) in aqueous solution. (**c**) Schematic of TEM scattering intensity versus lateral extension. From [269]

The encapsulation of a larger hydrophobic model substrate was successfully realized utilizing highly fluorescent QDs. The enclosing of these nanoparticles inside the PB-*b*-PEO polymersomes was performed only via the film rehydration procedure because the preferred dispersant of QDs, chloroform, is immiscible with water and therefore not suitable for the cosolvent method. The rehydration procedure for QDs was done analogously to that for the Nile Red samples. Afterwards, filtration through 0.45-μm filters ensured a smaller vesicle size regime, which is important for further characterization. Absorption and emission spectra indicated the presence of QDs in the vesicle solution after filtration (Fig. 65).

The quantification of QD load in the polymersomes has not yet been possible because the rehydration method never led to a complete solution of material and the QD absorption peak is drowned in the high scattering background of those huge and broadly distributed polymersomes. Furthermore, exact reference concentrations are difficult to determine for core–shell QD solutions.

Cryogenic TEM images of hydrophobically stabilized QD-containing polymersome samples are shown in Fig. 66. The PB-*b*-PEO copolymer exhibits a low scattering contrast compared to the QDs, enabling the QDs to be clearly seen as dark spots inside the vesicle structure. The TEM image represents a projection of the 3D loaded vesicle (as it is frozen in the water film) into the 2D imaging plane. Those QDs appearing in the inner core due to the projection are therefore also enclosed in the polymersome shell (Fig. 66c). Appropriate sample tilt during imaging reveals the QD position in the middle of the polymersome shell (Fig. 66b), between the two polybutadiene layers, introducing a curvature into the assembled shell. This QD/PB-*b*-PEO system is an example of hydrophobic polymersome shell loading. The phenomenon of bending around the guest particle is currently under investigation as a function of membrane thickness and incorporated nanoparticle diameter. A comparable mechanism has been observed experimentally and theoretically for the incorporation of colloids into block copolymers in the bulk [273–275].

As cryogenic TEM imaging does not necessarily represent the entire sample, FCS measurements (data not shown) were performed additionally for measuring diffusion coefficients of fluorescent particles [271, 276–280]. Light scattering yields a hydrodynamic radius of $R_h = 67$ nm, which describes the average of the whole sample content. Nevertheless, the result is in good agreement with FCS, which yields $R_h = 62$ nm detecting only the fluorescent sample content (in our case the loaded polymersomes). Both results are comparable to those observed with cryogenic TEM; two examples are shown in Fig. 66a, b. The agreement of DLS and FCS results shows that Nile Red and QDs were successfully incorporated into the hydrophobic part of the polymersomes.

In conclusion, the hydrophobic shell of PB-*b*-PEO polymersomes was successfully loaded with the fluorescent dye Nile Red and highly fluorescent QDs as hydrophobic model substrates. FCS showed that fluorescing signals belong to the diffusion of fluorescently loaded vesicles only, demonstrating that no other aggregation or structure stabilization occurred. Cryogenic TEM and fluorescence microscopy imaging confirmed that the hydrophobic substrates were enclosed inside the hydrophobic polymersome shell. In the case of the QD-loaded polymersomes, it has been possible by cryogenic TEM imaging to prove that the QD are located in between the two hydrophobic PB layers of the shell bilayer, introducing curvature of the copolymer layers around the guest particles. The combination of independent methods of characterization made it possible to successfully investigate the localization of the hydrophobic substrates within the hydrophobic shell of the polymersomes. Further experiments with differently sized nanoparticles will determine the limits for particle enclosing and confinement inside the shell, revealing how far the double-layer can curve before different structural assemblies are favored. Furthermore, these experiments can be nicely linked to the results obtained in other particle systems or confinement of nanoparticles in planar surfaces, as discussed in the other parts of this chapter.

5.4   Conclusion

The process of formation of complex block copolymer structures in 3D confinement has been elucidated for some selected PS-*b*-PMMA copolymers. Introduction of a nonsolvent into the spherical nanoparticles yielded hemispherical structures of onion-like morphology. Such structures may be viewed as a result of double confinement consisting of the outer surfactant double layer and the inner nanophase separation between the block copolymer and the nonsolvent for both blocks. This concept allows targeting the nanoparticle shape as well as the inner particle morphology (ranging from simple core–shell to onion-like to patched structures), which may find application for encapsulation of various substrates with predetermined release characteristics.

Regarding 2D confinement, newly synthesized "junction-point" block copolymers were chemically anchored onto planar substrates by their reactive junction-point moiety, forming a smooth monomolecular layer. By thermal treatment or exposure

to selective solvents for either of the blocks, the surface tension or contact angle of the coated substrate could be reversibly switched. Such adaptive surfaces may have potential applications for anti-fouling and self-cleaning surfaces.

Finally, fluorescent dye molecules as well as QDs were successfully immobilized in the hydrophobic part of the double layer of block copolymer vesicles below 100 nm in size. In the case of the QDs, the double layer was observed to strongly curve around the guest particles without becoming destabilized. The limit of stable confinement in terms of size and polarity of the guest molecules will be subject of future investigations. The presented example demonstrates that 2D confinement within a vesicle shell principally allows control of the spatial arrangement of nanoparticles in solution.

6 Towards Synthesis on an Insulating Surface

6.1 Introduction

Synthesizing macromolecules or studying the structure and dynamics of macromolecules in confining geometries is a challenging element of polymer science. A surface can also serve as confining geometry for both polymer synthesis and polymer characterization. Immobilizing polymerizable monomers on solid surfaces with suitable anchor groups and subjecting them to network formation is a well-established coating technique. A much more sophisticated approach to surface-bound polymer synthesis is the deposition of reactive monomers on conductive or insulating substrates and the promotion of light- or heat-driven polymerizations under in-situ control by scanning probe techniques. As well as the possibility of following macromolecule formation with atomic precision in real space, the surface can now also act as template by either stabilizing reactive intermediates or by pre-organizing them into a desired pattern.

In general, creating complex polymer architectures on surfaces offers a great potential for future applications, e.g., in the fields of (bio)sensors and molecular electronics. The bottom-up construction of functional devices from molecular building blocks provides utmost control in tailoring the properties and functionality of materials. Encoding the resulting structure and functionality in the molecular building blocks has been explored extensively in the field of molecular self-assembly [281]. However, because molecular self-assembly relies on weak, reversible inter-molecular interactions to arrive at the (local) thermodynamic minimum, the resulting structures are inherently unstable and might not survive further processing or harsh operation conditions. Moreover, when aiming at electrically conductive structures, conjugated structures are desired because of their superior electron transport properties. To provide stability and electric conductivity, on-surface synthesis has recently been explored as a promising route to the creation of covalently linked molecular structures [282, 283]. So far, these studies have been limited to metallic
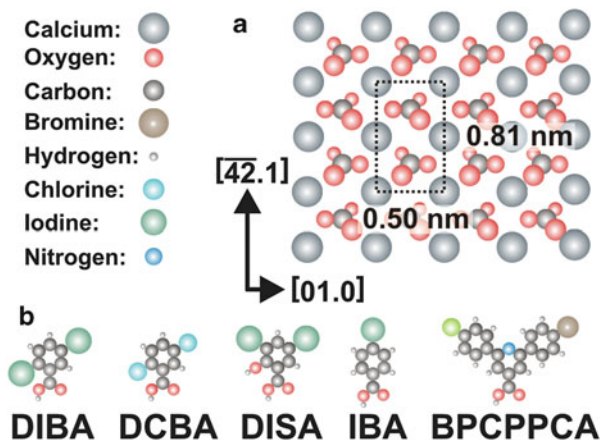
Fig. 67 Models of (**a**) the calcite(10.4) surface and (**b**) organic molecules 4-iodo benzoic acid (IBA), 2,5-diiodo benzoic acid (DIBA), 2,5-dichloro benzoic acid (DCBA), 3,5-diiodo salicylic acid (DISA) and 2-(4-bromophenyl)-6-(4-chlorophenyl)pyridine-4-carboxylic acid (BPCPPCA). The CaCO₃ (10.4) surface has a rectangular unit cell of size 0.50×0.81 nm², consisting of two carbonate groups and two calcium ions. The carbonate groups are rotated such that one oxygen atom lies above, one in, and one below the plane spanned by the calcium ions

substrates only [284–288]. From an experimental point of view, this is motivated by the fact that most surface-sensitive techniques such as scanning tunneling microscopy, low-energy electron diffraction, or photoelectron spectroscopy require conductive samples. Moreover, when considering covalent coupling based on an Ullmann-type reaction, a metallic surface has been regarded as mandatory because it is known to act as a catalyst.

Molecular electronics applications will, however, require decoupling the electronic structure of the polymer architecture from the supporting substrate. Moreover, extending the material base from metals to the comparatively heterogeneous group of bulk insulators offers the potential for tailoring the substrate properties to the specific, application-oriented needs.

We have, therefore, explored on-surfaces synthesis on a bulk insulator surface. As a prerequisite, we investigated strategies for anchoring organic molecules to insulating surfaces in order to avoid molecule desorption upon thermal activation of the linking reaction [289]. We succeeded in presenting the first demonstration of a covalent linking reaction on an insulating surface in an ultrahigh vacuum environment [290]. We then built upon this proof-of-concept work by exploring concepts for hierarchical structure formation to pave the way for creating complex polymer architectures on surfaces [291].

Insulating materials span a wide range from weakly van-der-Waals bonded molecular crystals to covalent crystals such as diamond or titanium dioxide to ionic crystals such as potassium bromide or calcium fluoride. Therefore, a general description of molecule–surface interactions is challenging in the case of insulating substrates. However, compared to metals, the interaction of organic molecules with

prototypical insulating surfaces such as KBr(001), NaCl(001), or CaF$_2$(111) is rather weak [292, 293]. This fact constitutes a severe challenge when aiming at complex structure formation because molecules tend to de-wet and pile up to form a 3D molecular bulk crystal.

Especially when aiming at thermal activation of an on-surface linking reaction, this rather weak molecule–surface interaction poses problems because many molecules desorb from the substrate upon annealing at temperatures well below the reaction temperature. Moreover, it is known that metal atoms act as catalysts in the dehalogenation that has been demonstrated before [285, 286]. Thus, as a first step, exploring suitable anchor groups turned out to be mandatory. Based on our previous results using the calcite as a substrate [294, 295], we identify the natural cleavage plane of calcite, namely calcite(10.4) (Fig. 67a), as an ideal substrate surface due to its comparatively high surface energy of 0.590 J/m^2 [295].

As simple model monomers, we explored the applicability of small benzoic acids derivatives (Fig. 67b), which were chosen for three reasons. First, these molecules are available in high purity and can readily be sublimated under ultrahigh vacuum conditions. Second, carboxylic acid groups are known to interact strongly with the calcite(10.4) surface [296]. This comparatively high molecule–substrate binding strength is employed to prevent clustering at step edges and to avoid desorption upon thermal activation of the coupling reaction. Depending on the acidity of the benzoic acid derivative, the as-deposited molecules can be deprotonated at room temperature or might require annealing for the deprotonation step to occur. We could directly follow such a deprotonation step at room temperature upon deposition of 2,5-dihydroxy benzoic acid having a pK_A value of 2.97 [297]. This study gives a first estimation of the protonation state of other benzoic acid derivatives as a function of the pK_A value. For all molecules shown here, deprotonation takes place on a surface held at room temperature when the pK_A value is around 3 or smaller. For molecules having a higher pK_A value, annealing is required to induce deprotonation. Third, by varying number and position of the halide substitution, we are able to rationally design the resulting polymer architecture.

6.2 Proof of Concept: Dehalogenation and Covalent Coupling on an Insulating Surface

For providing a proof-of-concept for covalent linking on a bulk insulator surface, we present the results of a systematic noncontact AFM study, investigating the reactions of four different halide-substituted benzoic acids. The molecules used were 4-iodo benzoic acid (IBA), 2,5-diiodo benzoic acid (DIBA), 2,5-dichloro benzoic acid (DCBA), and 3,5-diiodo salicylic acid (DISA), as shown in Fig. 67b. Within this series of systematically varied benzoic acid derivatives, IBA can be regarded as the conceptually simplest molecule. As only one halide atom is available for the linking reaction, dimer structures are expected. Based on the pK_A
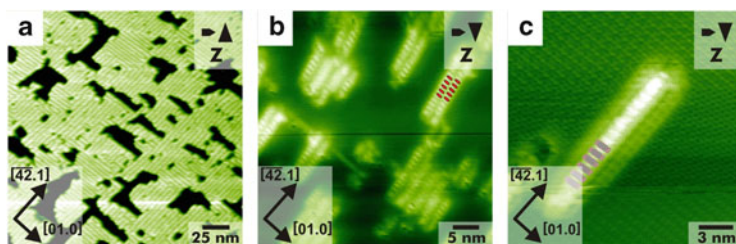
Fig. 68 Covalent linking of IBA. (**a**) After annealing of the IBA-covered sample to a temperature of around 250°C, two domains are revealed. (**b**) Molecular structure of the IBA-covered substrate after annealing to around 310°C, showing molecular rows running along the $[\overline{42}.1]$ direction. The rows are composed of individually resolved features that are aligned side-by-side. (**c**) Zoom onto a single molecular row with superimposed BPCDA model molecules

value of IBA of 4.02, we expect the molecules to remain protonated when deposited onto calcite(10.4) held at room temperature. This is, indeed, the case as can be deduced from two structural transitions that are observed upon annealing. Upon deposition at room temperature, the molecules appear to be mobile. No indication is obtained for island formation on the plane terraces. Molecular islands can only be found at step edges (not shown). After a first, moderate annealing step at around 250°C, two domains of extended islands are observed with a height of 0.8 nm, which suggests upright-standing molecules (Fig. 68a). This structure is readily explained by a deprotonation step, resulting in carboxylate species. The two domains can be understood by anchoring of the carboxylate groups to the surface calcium ions [298].

The linking reaction is induced when annealing the sample to around 310°C, which is associated with a second structural change (Fig. 68b). Now, rows are revealed that are oriented along the $[\overline{42}.1]$ calcite direction. The apparent height of the rows is 0.4 nm, suggesting a transition to flat-lying molecules. The rows are composed of features that fit excellently in size with the reaction product of two IBA molecules, namely biphenyl-4,4′-dicarboxylic acid (BPDCA). The BPDCA molecules align side-by-side, as illustrated by the superimposed ellipses with the size of BPDCA molecules (Fig. 68b). A high-resolution image of a single row is shown in Fig. 68c, which also reveals atomic resolution of the underlying calcite substrate. This image elucidates the binding configuration, confirming the assumption that the carboxylate group anchors to the surface calcium ions. The presence of the carboxylate group (being a strong electron donor) is expected to weaken the phenyl–halide bond. This might give an indication as to why homolytic cleavage of this bond is favored, resulting in reactive phenyl radicals at moderate temperatures without the need of a coupling catalyst. The transition in the molecular orientation provides further evidence for the covalent linking. After the reaction, the carboxylic groups point in opposite directions, making concerted binding of the carboxylate groups to the calcite impossible. As a consequence, the dimers are expected to lie flat on the surface, which is, indeed, observed. Thus, the formation of flat-lying
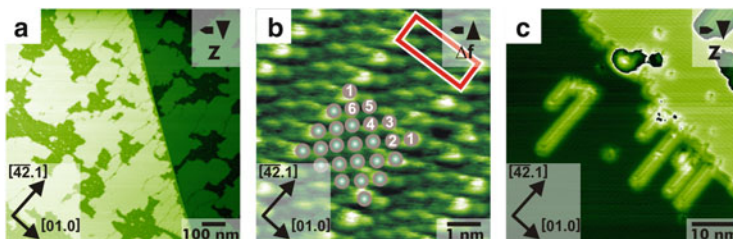
Fig. 69 (**a**) Overview image of DIBA, showing two calcite terraces covered by 0.7 nm high islands. (**b**) Drift-corrected detail image of the inner island structure with a (5 × 1) unit cell. (**c**) Structure obtained after annealing above 260°C. Molecular rows are observed that grow along the $[\overline{42}.1]$ direction

dimer species in the case of IBA monomer units constitutes the first indication of a successful covalent coupling reaction.

To arrive at extended polymeric structures, we next changed the monomer building block from having only one halide substitution to two halide atoms in *para* position. This should result in straight lines upon covalent coupling. To test this assumption, we investigated the structures observed upon deposition of DIBA. The as-deposited structure at room temperature is shown in Fig. 69a, revealing molecular islands. Based on the pK_A value of DIBA of 2.51, the molecules within the islands are expected to be deprotonated. A higher magnification image of the islands exhibits a (5 × 1) superstructure (Fig. 69b) with a moiré pattern, which can again be understood by the anchoring of the negatively charged carboxylate group with the surface calcium ions.

For DIBA, a structural change is initiated after annealing the sample to a temperature above 260°C, as shown in Fig. 69c. After annealing, the extended islands have vanished. Instead, rows running along the $[\overline{42}.1]$ direction are observed. This structural change can be understood by the thermolytic dissociation of the two iodine atoms from the molecule and subsequent covalent linking of the radical molecules. Because the iodine atoms are substituted at opposite positions, a straight row is expected upon covalent linking, in excellent agreement with the experimental finding. This assignment is further corroborated by the experimentally obtained periodicity along the chain of 0.41 nm, which fits to the distances expected for a polymeric chain.

To provide further proof for the homolytic cleavage and covalent coupling, we changed the halide atom from iodine to chlorine. This molecule, DCBA, has basically the same pK_A value of 2.50, but a higher carbon–halide bond strength (Cl-C_6H_5 399 kJ/mol versus I-C_6H_5 272 kJ/mol) [299]. Therefore, a similar reaction pathway is expected for DCBA. Exclusively considering the bond strengths certainly oversimplifies the situation; however, we expect that somewhat higher temperatures are required when repeating the same experiments with DCBA instead of DIBA. When performing the same experiment with DCBA, we found similar structures to those observed before for DIBA; however, the structural

Fig. 70 (**a**) Overview image of DISA deposited onto the calcite surface held at room temperature. (**b**) Drift-corrected detail image of an island, revealing a commensurate (1 × 1) structure. (**c**) Detail image after annealing to 310°C, revealing a distinctly different molecular structure. A *zigzag* pattern can be seen in the *upper right*. (**d**) Model of the different structures possible upon covalent linking. Besides zigzag rows, kinked and circular patterns are also possible
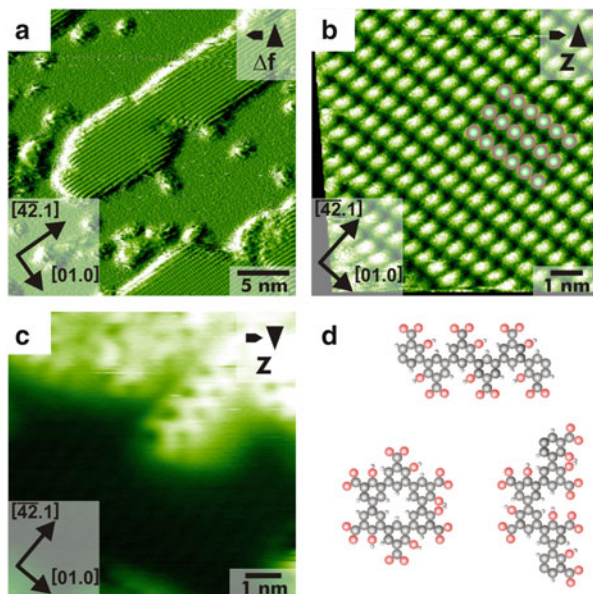
change only occurred when annealing above 295°C, which is, indeed, higher than needed for DIBA.

To explore the possibility of controlling the resulting polymer shape, we next changed the monomer building block with the idea that zigzag structures would be obtained instead of straight polymeric chains. This could be realized by changing the substitution position from *para* to *meta*. Because 3,5-diiodo benzoic acid was not available for this study, 3,5-diiodo salicylic acid (DISA) was used instead, having a pK_A of 2.07. Again, based on this pK_A, we expect the molecules to be deprotonated at room temperature.

When depositing DISA onto a calcite(10.4) surface held at room temperature, elongated islands are revealed (Fig. 70a) with a commensurate (1 × 1) superstructure (Fig. 70b). This structure can be explained by upright-standing molecules that again anchor with their carboxylate groups to the surface calcium ions. In the case of DISA, the reaction is induced upon annealing to approximately 310°C. Among the structures seen, zigzag structures are, indeed, obtained as shown in Fig. 70c. The apparent height of these structures suggests flat-lying molecules in this case. The observed transition from upright-standing molecules at room temperature to flat-lying molecules can be explained by considering the position of the carboxylate groups. Individual DISA molecules can arrange themselves with the carboxylate groups pointing towards the calcite surface. After linking, however, the carboxylate groups point in opposite directions, which prevents concerted binding of these groups to the surface. This provides the clue to understanding the transition from upright-standing to flat-lying molecules.
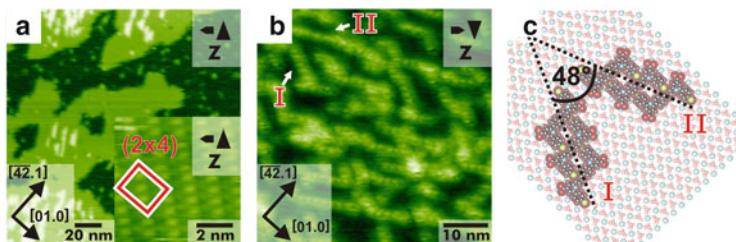
Fig. 71 Molecular structures of BPCPPCA onto calcite(10.4). (**a**) As-deposited, ordered island with a (2 × 4) superstructure (*inset*). (**b**) Overview image after annealing the substrate to about 300°C for 1 h, revealing rows (labeled *I* and *II*) with two distinct angles with respect to the [01.0] direction. (**c**) Proposed model for the two row types on calcite(10.4)

The other structures seen can be easily understood by considering the binding possibilities of DISA. As shown in Fig. 70d, the zigzag structure is not the only possible linkage. This explains why the zigzag structure is not the only pattern that exists on the surface after annealing. With these results, we demonstrate that even shape control can be achieved by choosing rationally designed monomer building blocks.

6.3 Towards Hierarchical Structure Formation: Exploring Two-Step Reactions

After having demonstrated a proof-of-concept covalent linking reaction in ultrahigh vacuum [290], an important next step for creating complex structures is exploring strategies for including hierarchical control. Up to now, the structural complexity of the structures achieved by on-surface synthesis has been limited to single-step processes. Increasing the structural complexity of the resulting structures requires utmost control, with the ability to selectively induce sequential linking reactions in a hierarchical manner. This has recently been demonstrated using halide-substituted porphyrin derivatives on a Au(111) surface [300], elegantly exploiting the specific dissociation energies of the bromine–phenyl and iodine–phenyl bonds. Because the dissociation energies are associated with different activation temperatures, the linking reactions can be performed in a site-specific and sequential manner. Thus, reaction sites and sequence are encoded in the structure of the precursor molecules. The latter results have, however, been obtained on a metallic substrate, again limiting the applicability of these structures with regard to molecular electronics.

Based on the results obtained, we chose a molecule for demonstrating a site-specific and selective two-step linking process on a bulk insulator surface in ultrahigh vacuum [298]. Bromophenyl and chlorophenyl groups were chosen for inducing site-specific and sequential covalent linking based on homolytic cleavage of the halide–phenyl bonds, having dissociation energies of 336 kJ/mol (Br-C_6H_5)
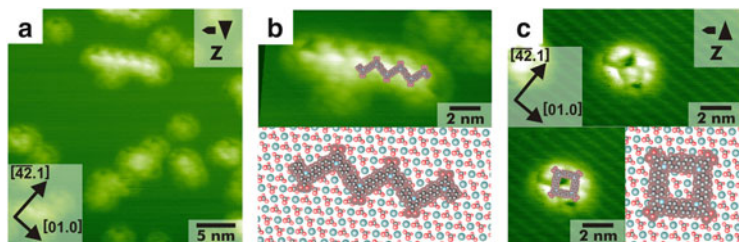
Fig. 72 Structures observed after the second annealing step to 340 K for 1 h. (**a**) Chains oriented along an angle of +60 ± 3° with respect to the $[\overline{42}.1]$ direction; ring-like features are observed to coexist on the surface. (**b**) Drift-corrected high-resolution image of an extended chain structure, with proposed model. (**c**) Drift-corrected high-resolution image of a closed ring structure, with proposed model. Note that the lines running from the *upper left* to *lower right* originate from the calcite(10.4) substrate

and 399 kJ/mol (Cl-C$_6$H$_5$), respectively [299]. Again, a carboxylic acid moiety was chosen to provide sufficient anchoring towards the calcite surface.

When depositing a submonolayer of BPCPPCA onto the calcite(10.4) surface at room temperature, ordered islands of a (2 × 4) superstructure are formed, as shown in Fig. 71a.

A first distinct change in the molecular structure is induced upon annealing to 300°C, which can be assigned to the homolytic cleavage of the bromine–phenyl bond and subsequent covalent linking of the resulting radicals, resulting in molecular dimers. A representative image is given in Fig. 71b. Instead of ordered islands, rows are formed on the surface. Although the overall ordering is poor compared to the islands, two main orientations of the rows can be identified that span an angle of 49 ± 3°. A dimer structure that is covalently linked at the former bromine position, 6,6′-[(1,1′-biphenyl)-4,4′-diyl]bis[2-(4-chloro- phenyl)isonicotinic acid], exhibits either a U- or an S-like shape. A stacking model for the S-form is given in Fig. 71c. Optimizing the intermolecular distance to allow for halogen–π interaction can be understood as the driving force behind the lateral shift of the molecules perpendicular to the row direction. This readily results in a molecular chain that forms an angle of either +66° or −66° with respect to the $[\overline{42}.1]$ mirror direction, resulting in an opening angle of 48°, in excellent agreement with the experimentally observed opening angle.

To induce the second reaction step, we annealed the surface to 340°C. The resulting structures are shown in Fig. 72. Most strikingly, the molecular structures that are present on the surface after the second annealing steps are, again, distinctly different from both the as-deposited ordered islands and the row structures observed after the first, moderate annealing step.

After the second annealing step, chains are oriented along an angle of 60 ± 3° with respect to the $[\overline{42}.1]$ direction and ring-like features are observed to coexist on the surface (Fig. 72a). The rows (Fig. 72b) differ in appearance and, most notably, in orientation as compared to the previously observed row structure, clearly indicating that the present chains are composed of building blocks other than

those in the previous row structures. A model can be drawn that is based on linking of the dimer to an extended row. This model is positioned onto the surface with the carboxylate groups positioned on top of the surface calcium ions. Despite this simple approach, the model fits excellently in size, in periodic repeat distance, and in the observed orientation on the surface. These three structural features together corroborate the model of a further linking of the dimer units into a zigzag polymer.

Considering the basic dimer units suggests that a second structure is feasible when linking the dimer building blocks, namely a closed ring. This structure is observed experimentally, as shown in Fig. 72c. The size of the ring-like structures fits excellently in size with a structure that is composed by further linking of the dimer molecules via cleavage of the chlorine–phenyl bond. Arranging the model such that the carboxylate groups can bind towards the calcium cations results in a well-defined angle with respect to the underlying substrate, which is exactly what is observed experimentally.

Thus, a two-step linking reaction was achieved by a sequential and selective activation of two reaction sites. Extended zigzag and closed ring structures were created upon sequential activation of homolytic cleavage of, first, the bromine–phenyl bonds and, second, the chlorine–phenyl bonds.

To conclude, we have demonstrated a proof-of-principle reaction of the covalent coupling of halide-substituted benzoic acid molecules on a bulk insulator, namely calcite(10.4). Depending on the number and position of the halide substitution, we can rationally design the structure of the resulting conjugated oligomers.

As a second step, we explored the possibility of a two-step polymerization reaction to enhance the structural control necessary to arrive at complex polymer architectures. By carefully selecting a precursor monomer that provides the encoding of the selective and sequential reaction sites, we rationally controlled a hierarchical two-step reaction process.

On-surface synthesis is expected to enhance variability when aiming at structure formation on surfaces. First, on-surface synthesis allows the creation of polymeric structures that might not be accessible from solution synthesis due to poor solubility. Second, larger structures that are difficult to transfer onto a supporting surface can be fabricated directly on the surface of interest, greatly facilitating the fabrication process. Third, due to the confinement of the molecular building blocks onto the 2D surface, fundamental new reaction pathways might be envisioned, providing further means for extending the structural complexity.

References

1. Vögtle F (2001) Dendrimers III – design, dimension, function. In: Houk KN, de Meijere A, Kessler H, Lehn I-M, Ley SV, Schreiber SL, Thiem I, Trost BM (eds) Topics in current chemistry, vol 212. Springer, Berlin

2. Frechet JMJ, Tomalia DA (2001) Dendrimers and other dendritic polymers. In: Scheirs J (ed) Wiley series in polymer science. Wiley, New York, p 688
3. Hawker CJ, Frechet JMJ (1990) J Am Chem Soc 112:7638
4. Fischer M, Vogtle F (1999) Angew Chem Int Ed 38:885
5. Tomalia DA, Naylor AM, Goddard WA (1990) Angew Chem Int Ed 29:138
6. Bosman AW, Janssen HM, Meijer EW (1999) Chem Rev 99:1665
7. Türp D, Nguyen T-T-T, Baumgarten M, Müllen K (2012) New J Chem 36:282
8. Miller TM, Neenan TX (1990) Chem Mater 2:346
9. Miller TM, Neenan TX, Zayas R, Bair HE (1992) J Am Chem Soc 114:1018
10. Tomalia DA, Baker H, Dewald J, Hall M, Kallos G, Martin S, Roeck J, Ryder J, Smith P (1985) Polym J 17:117
11. Petekidis G, Vlassopoulos D, Galda P, Rehahn M, Ballauff M (1996) Macromolecules 29:8948
12. Buhleier E, Wehner W, Vogtle F (1978) Synthesis-Stuttgart 1978(2):155-158
13. Andreitchenko EV, Clark CG, Bauer RE, Lieser G, Müllen K (2005) Angew Chem Int Ed 44:6348
14. Clark CG Jr, Wenzel RJ, Andreitchenko EV, Steffen W, Zenobi R, Müllen K (2007) J Am Chem Soc 129:3292
15. Morgenroth F, Reuther E, Müllen K (1997) Angew Chem Int Ed 36:631
16. Yin M, Ding K, Gropeanu RA, Shen J, Berger R, Weil T, Müllen K (2008) Biomacromolecules 9:3231
17. Herrmann A, Mihov G, Vandermeulen GWM, Klok HA, Müllen K (2003) Tetrahedron 59:3925
18. Mondeshki M, Mihov G, Graf R, Spiess HW, Müllen K, Papadopoulos P, Gitsas A, Floudas G (2006) Macromolecules 39:9605
19. Mihov G, Grebel-Koehler D, Lubbert A, Vandermeulen GWM, Herrmann A, Klok HA, Müllen K (2005) Bioconjug Chem 16:283
20. Türp D, Wagner M, Enkelmann V, Müllen K (2011) Angew Chem Int Ed 50:4962
21. Mpoukouvalas K, Türp D, Wagner M, Müllen K, Butt H-J, Floudas G (2011) J Phys Chem B 115:5801
22. Vanderhoeven PHC, Lyklema J (1992) Adv Colloid Interface Sci 42:205
23. Krossing I, Raabe I (2004) Angew Chem Int Ed 43:2066
24. Every HA, Bishop AG, MacFarlane DR, Oradd G, Forsyth M (2004) Phys Chem Chem Phys 6:1758
25. Strauss SH (1993) Chem Rev 93:927
26. Qu JQ, Pschirer NG, Liu DJ, Stefan A, De Schryver FC, Müllen K (2004) Chem Euro J 10:528
27. Qu JQ, Zhang JY, Grimsdale AC, Müllen K, Jaiser F, Yang XH, Neher D (2004) Macromolecules 37:8297
28. Herrmann A, Weil T, Sinigersky V, Wiesler UM, Vosch T, Hofkens J, De Schryver FC, Müllen K (2001) Chem Euro J 7:4844
29. Weil T, Reuther E, Beer C, Müllen K (2004) Chem Euro J 10:1398
30. Weil T, Reuther E, Müllen K (2002) Angew Chem Int Ed 41:1900
31. Weil T, Vosch T, Hofkens J, Peneva K, Müllen K (2010) Angew Chem Int Ed 49:9068
32. Österling I, Müllen K (2007) J Am Chem Soc 129:4595
33. Gronheid R, Hofkens J, Kohn F, Weil T, Reuther E, Müllen K, De Schryver FC (2002) J Am Chem Soc 124:2418
34. Cotlet M, Gronheid R, Habuchi S, Stefan A, Barbafina A, Müllen K, Hofkens J, De Schryver FC (2003) J Am Chem Soc 125:13609
35. Masuo S, Vosch T, Cotlet M, Tinnefeld P, Habuchi S, Bell TDM, Oesterling I, Beljonne D, Champagne B, Müllen K, Sauer M, Hofkens J, De Schryver FC (2004) J Phys Chem B 108:16686

36. Qin T, Zhou G, Scheiber H, Bauer RE, Baunigarten M, Anson CE, List EJW, Müllen K (2008) Angew Chem Int Ed 47:8292
37. Qin T, Wiedemair W, Nau S, Trattnig R, Sax S, Winkler S, Vollmer A, Koch N, Baumgarten M, List EJW, Müllen K (2011) J Am Chem Soc 133:1301
38. Nguyen T-T-T, Türp D, Wagner M, Müllen K (2013) Angew Chem Int Ed 52:669
39. Nguyen T-T-T, Türp D, Wang D, Noelscher B, Laquai F, Müllen K (2011) J Am Chem Soc 133:11194
40. Shifrina ZB, Rajadurai MS, Firsova NV, Bronstein LM, Huang XL, Rusanov AL, Müllen K (2005) Macromolecules 38:9920
41. Lubczyk D, Siering C, Loergen J, Shifrina ZB, Müllen M, Waldvogel SR (2010) Sensor Actuator B 143:561
42. Lubczyk D, Grill M, Baumgarten M, Waldvogel SR, Müllen K (2012) Chemphyschem 77:102
43. Gardner J, Yinon J (2003) Electronic noses & sensors for the detection of explosives. II mathematics, physics and chemistry. Kluwer Academic, New York
44. Newkome GR, Moorefield CN, Baker GR, Johnson AL, Behera RK (1991) Angew Chem Int Ed 30:1176
45. Hawker CJ, Wooley KL, Frechet JMJ (1993) J Chem Soc Perkin Trans 1:1287
46. Hecht S, Frechet JMJ (2001) Angew Chem Int Ed 40:74
47. Loi S, Butt HJ, Hampel C, Bauer R, Wiesler UM, Müllen K (2002) Langmuir 18:2398
48. Loi S, Wiesler UM, Butt HJ, Müllen K (2000) Chem Commun 1169
49. Loi S, Wiesler UM, Butt HJ, Müllen K (2001) Macromolecules 34:3661
50. Frechet JMJ (1994) Science 263:1710
51. Yin M, Feng C, Shen J, Yu Y, Xu Z, Yang W, Knoll W, Müllen K (2011) Small 7:1629
52. Feng CL, Yin M, Zhang D, Zhu S, Caminade AM, Majoral JP, Müllen K (2011) Macromol Rapid Commun 32:679
53. Yu Y, Yin M, Müllen K, Knoll W (2012) J Mater Chem 22:7880
54. Yin M, Shen J, Pflugfelder GO, Müllen K (2008) J Am Chem Soc 130:7806
55. Yin M, Shen J, Gropeanu R, Pflugfelder GO, Weil T, Müllen K (2008) Small 4:894
56. Dufes C, Uchegbu IF, Schatzlein AG (2005) Adv Drug Deliv Rev 57:2177
57. Kuan SL, Stöckle B, Reichenwallner J, Ng DYW, Wu Y, Doroshenko M, Koynov K, Hinderberger D, Müllen K, Weil T (2013) Biomacromolecules 14:367
58. Boas U, Heegaard PMH (2004) Chem Soc Rev 33:43
59. Zhang MF, Müller AHE (2005) J Polym Sci A 43:3461
60. Sheiko SS, Sumerlin BS, Matyjaszewski K (2008) Progr Polym Sci 33:759
61. Hsu H-P, Paul W, Binder K (2011) Macromol Theor Sim 20:510
62. Fredrickson GH (1993) Macromolecules 26:2825
63. Zhang B, Gröhn F, Pedersen JS, Fischer K, Schmidt M (2006) Macromolecules 39:8440
64. Hsu H-P, Paul W, Binder K (2008) J Chem Phys 129:204904
65. Hsu H-P, Paul W, Rathgeber S, Binder K (2010) Macromolecules 43:1592
66. Hsu H-P, Paul W, Binder K (2010) Macromolecules 43:3094
67. Kratky O, Porod G (1949) J Colloid Sci 4:35
68. Grosberg AY, Khoklov AR (1994) Statistical physics of macromolecules. In: Larson R, Pincus PA (eds) AIP series in polymer and complex materials. AIP, New York, p 382
69. Hsu H-P, Paul W, Binder K (2011) Europhys Lett 95:68004
70. Hsu H-P, Paul W, Binder K (2010) Europhys Lett 92:28003
71. Theodorakis PE, Hsu H-P, Paul W, Binder K (2011) J Chem Phys 135:164903
72. Gerle M, Fischer K, Roos S, Muller AHE, Schmidt M, Sheiko SS, Prokhorova S, Moller M (1999) Macromolecules 32:2629
73. Sun F, Sheiko SS, Möller M, Beers K, Matyjaszewski K (2004) J Phys Chem A 108:9682
74. Sheiko SS, Borisov OV, Prokhorova SA, Möller M (2004) Eur Phys J E 13:125
75. Saariaho M, Ikkala O, Szleifer I, Erukhimovich I, ten Brinke G (1997) J Chem Phys 107:3267

76. Elli S, Ganazzoli F, Timoshenko EG, Kuznetsov YA, Connolly R (2004) J Chem Phys 120:6257
77. Connolly R, Bellesia G, Timoshenko EG, Kuznetsov YA, Elli S, Ganazzoli F (2005) Macromolecules 38:5288
78. Subbotin A, Saariaho M, Ikkala O, ten Brinke G (2000) Macromolecules 33:3447
79. Nakamura Y, Norisuye T (2001) Polym J 33:874
80. Gerle M (1998) Dissertation, Universität Mainz
81. Wintermantel M, Gerle M, Fischer K, Schmidt M, Wataoka I, Urakawa H, Kajiwara K, Tsukahara Y (1996) Macromolecules 29:978
82. Terao K, Takeo Y, Tazaki M, Nakamura Y, Norisuye T (1999) Polym J 31:193
83. Terao K, Nakamura Y, Norisuye T (1999) Macromolecules 32:711
84. Terao K, Hokajo T, Nakamura Y, Norisuye T (1999) Macromolecules 32:3690
85. Terao K, Hayashi S, Nakamura Y, Norisuye T (2000) Polym Bull 44:309
86. Hokajo T, Terao K, Nakamura Y, Norisuye T (2001) Polym J 33:481
87. Hsu HP, Paul W, Binder K (2013) Polym Sci Ser C 55:39
88. Sahl M, Muth S, Branscheid R, Fischer K, Schmidt M (2012) Macromolecules 45:5167
89. Cassim JY, Yang JT (1970) Biopolymers 9:1475
90. Gunari N, Cong Y, Zhang B, Fischer K, Janshoff A, Schmidt M (2008) Macromol Rapid Commun 29:821
91. Halperin A, Zhulina EB (1991) Europhys Lett 15:417
92. Theodorakis PE, Paul W, Binder K (2009) Europhys Lett 88:63002
93. Stephan T, Muth S, Schmidt M (2002) Macromolecules 35:9857
94. Heimann N (2004) Konformationsänderungen von zylindrischen Makromolekülen. Diploma thesis, University of Mainz
95. Zhang B, Zhang SJ, Okrasa L, Pakula T, Stephan T, Schmidt M (2004) Polymer 45:4009
96. Flory PJ (1953) Principles of polymer chemistry. Cornell University Press, Ithaca
97. Binder K (1994) Theories and mechanism of phase transitions, heterophase polymerizations, homopolymerization. Addition Polym 112:181
98. Enders S, Wolf BA (2011) Polymer thermodynamics: liquid polymer-containing mixtures. Springer, Berlin
99. Erukhimovich I, Theodorakis PE, Paul W, Binder K (2011) J Chem Phys 134:085101
100. Sevink GJA, Zvelindovsky AV, Fraaije J, Huinink HP (2001) J Chem Phys 115:8226
101. Erukhimovich I, Johner A (2007) Europhys Lett 79:56004
102. Stepanyan R, Subbotin A, ten Brinke G (2002) Macromolecules 35:5640
103. de Jong J, ten Brinke G (2004) Macromol Theor Sim 13:318
104. Liu YF, Abetz V, Muller AHE (2003) Macromolecules 36:7894
105. Hsu H-P, Paul W, Binder K (2007) Macromol Theor Sim 16:660
106. Hamley IW (1998) The physics of block polymers. Oxford University Press, New York
107. Leibler L (1980) Macromolecules 13:1602
108. Landau LD, Lifshitz EM (1958) Statistical physics. Pergamon, London
109. Hsu H-P, Paul W, Binder K (2006) Europhys Lett 76:526
110. Hsu H-P, Paul W, Binder K (2007) Macromol Symp 252:58
111. Grassberger P (1997) Phys Rev E 56:3682
112. Hsu H-P, Grassberger P (2011) J Stat Phys 144:597
113. Li CM, Gunari N, Fischer K, Janshoff A, Schmidt M (2004) Angew Chem Int Ed 43:1101
114. Ballauff M, Lu Y (2007) Polymer 48:1815
115. Akcora P, Liu H, Kumar SK, Moll J, Li Y, Benicewicz BC, Schadler LS, Acehan D, Panagiotopoulos AZ, Pryamitsyn V, Ganesan V, Ilavsky J, Thiyagarajan P, Colby RH, Douglas JF (2009) Nat Mater 8:354
116. Binder K, Milchev A (2012) J Polym Sci B 50:1515
117. Lo Verso F, Yelash L, Egorov SA, Binder K (2012) Soft Matter 8:4185
118. Lo Verso F, Yelash L, Egorov SA, Binder K (2011) J Chem Phys 135:214902
119. Lo Verso F, Egorov SA, Milchev A, Binder K (2010) J Chem Phys 133:184901

120. Lo Verso F, Egorov SA, Binder K (2012) Macromolecules 45:8892
121. Kremer K, Grest GS (1995) Entanglement effects in polymer melts and networks. In: Binder K (ed) Monte Carlo and molecular dynamics methods in polymer science. Oxford University Press, New York, p. 194
122. Egorov SA (2008) J Chem Phys 129:064901
123. Fleer GJ, Cohen Stuart MA, Scheutjens JMHM, Cosgrove T, Vincent B (1993) Polymers at interfaces. Chapman & Hall, London, p 496
124. Reith D, Milchev A, Virnau P, Binder K (2011) Europhys Lett 95:28003
125. Reith D, Milchev A, Virnau P, Binder K (2012) Macromolecules 45:4381
126. Reith D, Mirny L, Virnau P (2011) Progr Theor Phys Suppl 191:135
127. Halverson JD, Lee WB, Grest GS, Grosberg AY, Kremer K (2011) J Chem Phys 134:204904
128. Wieland T, Goldmann H, Kern W (1953) Macromol Chem Phys 10:136
129. Michaels AS, Miekka RG (1961) J Phys Chem 65:1765
130. Kabanov VA, Zezin AB, Izumrudov VA, Bronich TK, Bakeev KN (1985) Macromol Chem Phys 13:137-155 doi: 10.1002/macp.1985.020131985111
131. Dautzenberg H (2000) Macromol Symp 162:1
132. Thünemann A, Müller M, Dautzenberg H, Joanny J-F, Löwen H (2004) Polyelectrolyte Complexes. In: Schimidt M (ed) Polyelectrolytes with defined molecular architecture II. Springer, Berlin, p 113
133. Karibyants N, Dautzenberg H, Colfen H (1997) Macromolecules 30:7803
134. Bloomfield VA (1997) Biopolymers 44:269
135. Park TG, Jeong JH, Kim SW (2006) Adv Drug Deliv Rev 58:467
136. Haag R, Kratz F (2006) Angew Chem Int Ed 45:1198
137. Kabanov AV, Kabanov VA (1995) Bioconjug Chem 6:7
138. Bronich TK, Nguyen HK, Eisenberg A, Kabanov AV (2000) J Am Chem Soc 122:8339
139. Fischer D, Dautzenberg H, Kunath K, Kissel T (2004) Intern J Pharm 280:253
140. Katakura H, Harada A, Kataoka K, Furusho M, Tanaka F, Wada H, Ikenaka K (2004) J Gene Med 6:471
141. Oupicky D, Reschel T, Konak C, Oupicka L (2003) Macromolecules 36:6863
142. Ogris M, Steinlein P, Kursa M, Mechtler K, Kircheis R, Wagner E (1998) Gene Ther 5:1425
143. Boeckle S, von Gersdorff K, van der Piepen S, Culmsee C, Wagner E, Ogris M (2004) J Gene Med 6:1102
144. Chen W, Turro NJ, Tomalia DA (2000) Langmuir 16:15
145. Ottaviani MF, Sacchi B, Turro NJ, Chen W, Jockusch S, Tomalia DA (1999) Macromolecules 32:2275
146. Zinchenko AA, Yoshikawa K, Baigl D (2005) Phys Rev Lett 95:228101
147. Keren K, Soen Y, Ben Yoseph G, Gilad R, Braun E, Sivan U, Talmon Y (2002) Phys Rev Lett 89:088103
148. Gössl I, Shu L, Schlüter AD, Rabe JP (2002) J Am Chem Soc 124:6860
149. Gössl I, Shu L, Schlüter D, Rabe JP (2002) Single Molecules 3:315
150. Störkle D, Duschner S, Heimann N, Maskos M, Schmidt M (2007) Macromolecules 40:7998
151. Kuehn F, Fischer K, Schmidt M (2009) Macromol Rapid Commun 30:1470
152. Duschner S, Störkle D, Schmidt M, Maskos M (2008) Macromolecules 41:9067
153. Krohne K, Duschner S, Störkle D, Schmidt M, Maskos M (2010) Macromolecules 43:8645
154. Medina-Oliva A (2012) Ph.D. thesis, Dept. of Chemistry, University of Mainz, Mainz
155. Eisenriegler E (1991) Polymers near surfaces. World Scientific, Singapore
156. Gunari N, Schmidt M, Janshoff A (2006) Macromolecules 39:2219
157. Hsu H-P, Paul W, Binder K (2011) J Phys Chem B 115:14116
158. Winter D, Virnau P, Binder K (2009) Phys Rev Lett 103:225703
159. Hsu H-P, Paul W, Binder K (2010) J Chem Phys 133:104901
160. Brown SP, Spiess HW (2001) Chem Rev 101:4125
161. Brown SP (2009) Macromol Rapid Commun 30:688
162. Sebastiani D (2006) Chemphyschem 7:164

163. Tonelli AE, Schilling FC (1981) Acc Chem Res 14:233
164. Hansen MR, Graf R, Spiess HW (2013) Acc Chem Res 46:1996
165. Ober CK, Cheng SZD, Hammond PT, Muthukumar M, Reichmanis E, Wooley KL, Lodge TP (2009) Macromolecules 42:465
166. Spiess HW (2010) Macromolecules 43:5479
167. Vila JA, Scheraga HA (2009) Acc Chem Res 42:1545
168. Ochsenfeld C, Brown SP, Schnell I, Gauss J, Spiess HW (2001) J Am Chem Soc 123:2597
169. Spiess HW (2004) J Polym Sci A 42:5031
170. Dudenko D, Kiersnowski A, Shu J, Pisula W, Sebastiani D, Spiess HW, Hansen MR (2012) Angew Chem Int Ed 51:11068
171. Wüthrich K (2003) Angew Chem Int Ed 42:3340
172. Pannier M, Veit S, Godt A, Jeschke G, Spiess HW (2000) J Magn Reson 142:331
173. Spiess HW (2011) J Magn Reson 213:326
174. Jeschke G (2012) Annu Rev Phys Chem 62:419
175. Hubbell WL, Cafiso DS, Altenbach C (2000) Nat Struct Biol 7:735
176. Dockter C, Volkov A, Bauer C, Polyhach Y, Joly-Lopez Z, Jeschke G, Paulsen H (2009) Proc Natl Acad Sci USA 106:18485
177. Walton AG, Blackwell JB (1973) Biopolymers. Academic, New York
178. Klok H-A, Lecommandoux S (2006) Solid-state structure, organization and properties of peptide – synthetic hybrid block copolymers. In: Klok HA, Schlaad H (eds) Peptide hybrid polymers, Advances in polymer science, vol 202. Springer, Berlin, pp 75-111
179. Tycko R (2001) Ann Rev Phys Chem 52:575
180. Strobl G (2007) The physics of polymers: concepts for understanding their structures and behavior, 3rd edn. Springer, New York, 518
181. Floudas G, Spiess HW (2009) Macromol Rapid Commun 30:278
182. Floudas G (2004) Progr Polym Sci 29:1143
183. Wang J, Lu H, Ren Y, Zhang YF, Morton M, Cheng JJ, Lin Y (2011) Macromolecules 44:8699
184. Aliferis T, Iatrou H, Hadjichristidis N (2004) Biomacromolecules 5:1653
185. Floudas G, Papadopoulos P, Klok HA, Vandermeulen GWM, Rodriguez-Hernandez J (2003) Macromolecules 36:3673
186. Gibson MI, Cameron NR (2008) Angew Chem Int Ed 47:5160
187. Gitsas A, Floudas G, Mondeshki M, Lieberwirth I, Spiess HW, Iatrou H, Hadjichristidis N, Hirao A (2010) Macromolecules 43:1874
188. Graf R, Spiess HW, Floudas G, Butt HJ, Gkikas M, Iatrou H (2012) Macromolecules 45:9326
189. Bates FS, Fredrickson GH (1990) Ann Rev Phys Chem 41:525
190. Clark CG, Floudas GA, Lee YJ, Graf R, Spiess HW, Müllen K (2009) J Am Chem Soc 131:8537
191. Young Joo L, Clark CG Jr, Graf R, Wagner M, Müllen K, Spiess HW (2009) J Phys Chem B 113:1360
192. Gorelik T, Matveeva G, Kolb U, Schleuss T, Kilbinger AFM, van de Streek J, Bohle A, Brunklaus G (2010) CrystEngComm 12:1824
193. Gorelik TE, van de Streek J, Kilbinger AFM, Brunklaus G, Kolb U (2012) Acta Crystallogr B 68:171
194. Bohle A, Brunklaus G, Hansen MR, Schleuss TW, Kilbinger AFM, Seltmann J, Spiess HW (2010) Macromolecules 43:4978
195. Palmans ARA, Meijer EW (2007) Angew Chem Int Ed 46:8948
196. Metzroth T, Hoffmann A, Martin-Rapun R, Smulders MMJ, Pieterse K, Palmans ARA, Vekemans JAJM, Meijer EW, Spiess HW, Gauss J (2011) Chem Sci 2:69
197. Wegner M, Dudenko D, Sebastiani D, Palmans ARA, de Greef TFA, Graf R, Spiess HW (2011) Chem Sci 2:2040
198. Zhao DY, Feng JL, Huo QS, Melosh N, Fredrickson GH, Chmelka BF, Stucky GD (1998) Science 279:548

199. Ferey G, Mellot-Draznieks C, Serre C, Millange F, Dutour J, Surble S, Margiolaki I (2005) Science 309:2040
200. Vollmeyer J, Jester SS, Eberhagen F, Prangenberg T, Mader W, Höger S (2012) Chem Commun 48:6547
201. Fritzsche M, Bohle A, Dudenko D, Baumeister U, Sebastiani D, Richardt G, Spiess HW, Hansen MR, Hoeger S (2011) Angew Chem Int Ed 50:3030
202. Ajami D, Rebek J (2008) Angew Chem Int Ed 47:6059
203. Moon C, Brunklaus G, Sebastiani D, Rudzevich Y, Böhmer V, Spiess HW (2009) Phys Chem Chem Phys 11:9241
204. Wu JS, Pisula W, Müllen K (2007) Chem Rev 107:718
205. Feng X, Marcon V, Pisula W, Hansen MR, Kirkpatrick J, Grozema F, Andrienko D, Kremer K, Müllen K (2009) Nat Mater 8:421
206. Elmahdy MM, Mondeshki M, Dou X, Butt H-J, Spiess HW, Müllen K, Floudas G (2009) J Chem Phys 131: 114704
207. Herbst W, Hunger K (2004) Industrial Organic pigments: production, properties, applications, 3rd edn. Wiley-VCH, Weinheim, p 678
208. Schmidt-Mende L, Fechtenkotter A, Müllen K, Moons E, Friend RH, MacKenzie JD (2001) Science 293:1119
209. Tasios N, Grigoriadis C, Hansen MR, Wonneberger H, Li C, Spiess HW, Müllen K, Floudas G (2010) J Am Chem Soc 132:7478
210. Percec V, Hudson SD, Peterca M, Leowanawat P, Aqad E, Graf R, Spiess HW, Zeng X, Ungar G, Heiney PA (2011) J Am Chem Soc 133:18479
211. Förster S, Konrad M (2003) J Mater Chem 13:2671
212. Yoon J, Lee W, Thomas EL (2006) Nano Lett 6:2211
213. Park M, Harrison C, Chaikin PM, Register RA, Adamson DH (1997) Science 276:1401
214. Kikuchi M, Binder K (1994) J Chem Phys 101:3367
215. Shin K, Xiang HQ, Moon SI, Kim T, McCarthy TJ, Russell TP (2004) Science 306:76
216. Ma M, Krikorian V, Yu JH, Thomas EL, Rutledge GC (2006) Nano Lett 6:2969
217. Thomas EL, Reffner JR, Bellare J (1990) J de Physique 51:C7363
218. Higuchi T, Motoyoshi K, Sugimori H, Jinnai H, Yabu H, Shimomura M (2010) Macromol Rapid Commun 31:1773
219. Hales K, Chen Z, Wooley KL, Pochan DJ (2008) Nano Lett 8:2023
220. Crespy D, Landfester K (2007) Macromol Chem Phys 208:457
221. Staff RH, Rupper P, Lieberwirth I, Landfester K, Crespy D (2011) Soft Matter 7:10219
222. Winkler A, Statt A, Virnau P, Binder K (2013) Phys Rev E 87:032307
223. Statt A, Winkler A, Virnau P, Binder K (2012) J Phys Condens Matter 24:464122
224. Reith D, Virnau P (2010) Comput Phys Commun 181:800
225. Reith D, Virnau P (2011) Comput Phys Commun 182:1945
226. Reith D, Cifra P, Stasiak A, Virnau P (2012) Nucleic Acids Res 40:5129
227. Virnau P, Rieger FC, Reith D (2013) Biochem Soc Trans 41:528
228. Howarter JA, Youngblood JP (2007) Adv Mater 19:3838
229. Ghosh B, Urban MW (2009) Science 323:1458
230. Uhlmann P, Ionov L, Houbenov N, Nitschke M, Grundke K, Motornov M, Minko S, Stamm M (2006) Prog Org Coat 55:168
231. Sui ZJ, Schlenoff JB (2003) Langmuir 19:7829
232. Zhao B, Haasch RT, MacLaren S (2004) J Am Chem Soc 126:6124
233. Julthongpiput D, Lin YH, Teng J, Zubarev ER, Tsukruk VV (2003) J Am Chem Soc 125:15912
234. Zhulina E, Balazs AC (1996) Macromolecules 29:2667
235. Lin YH, Teng J, Zubarev ER, Shulha H, Tsukruk VV (2005) Nano Lett 5:491
236. Wang Y, Zheng JX, Brittain WJ, Cheng SZD (2006) J Polym Sci A 44:5608
237. Tonhauser C, Wilms D, Wurm F, Berger-Nicoletti E, Maskos M, Löwe H, Frey H (2010) Macromolecules 43:5582

238. Tonhauser C, Obermeier B, Mangold C, Löwe H, Frey H (2011) Chem Commun 47:8964
239. Tonhauser C, Golriz AA, Moers C, Klein R, Butt HJ, Frey H (2012) Adv Mater 24:5559
240. Neto C, James M, Telford AM (2009) Macromolecules 42:4801
241. Discher DE, Eisenberg A (2002) Science 297:967
242. Lee JCM, Bermudez H, Discher BM, Sheehan MA, Won YY, Bates FS, Discher DE (2001) Biotechnol Bioeng 73:135
243. Förster S, Berton B, Hentze HP, Kramer E, Antonietti M, Lindner P (2001) Macromolecules 34:4610
244. Antonietti M, Förster S (2003) Adv Mater 15:1323
245. Jain S, Bates FS (2003) Science 300:460
246. Maskos M (2006) Polymer 47:1172
247. Caliceti P, Veronese FM (2003) Adv Drug Deliv Rev 55:1261
248. Haag R (2004) Angew Chem Int Ed 116:280
249. Bermudez H, Brannan AK, Hammer DA, Bates FS, Discher DE (2002) Macromolecules 35:8203
250. Maskos M, Harris JR (2001) Macromol Rapid Commun 22:271
251. Jofre A, Hutchison JB, Kishore R, Locascio LE, Helmerson K (2007) J Phys Chem B 111:5162
252. Checot F, Lecommandoux S, Klok HA, Gnanou Y (2003) Eur Phys J E 10:25
253. Allen C, Maysinger D, Eisenberg A (1999) Colloids Surf B 16:3
254. Kataoka K, Harada A, Nagasaki Y (2001) Adv Drug Deliv Rev 47:113
255. Choucair A, Soo PL, Eisenberg A (2005) Langmuir 21:9308
256. Borchert U, Lipprandt U, Bilang M, Kimpfler A, Rank A, Peschka-Suess R, Schubert R, Lindner P, Förster S (2006) Langmuir 22:5843
257. Lecommandoux SB, Sandre O, Checot F, Rodriguez-Hernandez J, Perzynski R (2005) Adv Mater 17:712
258. Krack M, Hohenberg H, Kornowski A, Lindner P, Weller H, Förster S (2008) J Am Chem Soc 130:7315
259. Ghoroghchian PP, Lin JJ, Brannan AK, Frail PR, Bates FS, Therien MJ, Hammer DA (2006) Soft Matter 2:973
260. Nardin C, Thoeni S, Widmer J, Winterhalter M, Meier W (2000) Chem Commun 2000:1433
261. Binder WH, Sachsenhofer R, Farnik D, Blaas D (2007) Phys Chem Chem Phys 9:6435
262. Binder WH, Sachsenhofer R (2008) Macromol Rapid Commun 29:1097
263. Lecommandoux S, Sandre O, Checot F, Perzynski R (2006) Progr Solid State Chem 34:171
264. Ghoroghchian PP, Frail PR, Susumu K, Park TH, Wu SP, Uyeda HT, Hammer DA, Therien MJ (2005) J Am Chem Soc 127:15388
265. Bockstaller MR, Lapetnikov Y, Margel S, Thomas EL (2003) J Am Chem Soc 125:5276
266. Chiu JJ, Kim BJ, Kramer EJ, Pine DJ (2005) J Am Chem Soc 127:5036
267. Ahmed F, Pakunlu RI, Brannan A, Bates F, Minko T, Discher DE (2006) J Control Release 116:150
268. Krishna MMG (1999) J Phys Chem A 103:3589
269. Hines MA, Guyot-Sionnest P (1996) J Phys Chem 100:468
270. Xie RG, Kolb U, Li JX, Basché T, Mews A (2005) J Am Chem Soc 127:7480
271. Müller W, Koynov K, Fischer K, Hartmann S, Pierrat S, Basché T, Maskos M (2009) Macromolecules 42:357
272. Goodwin AP, Mynar JL, Ma YZ, Fleming GR, Frechet JMJ (2005) J Am Chem Soc 127:9952
273. Chiu JJ, Kim BJ, Yi G-R, Bang J, Kramer EJ, Pine DJ (2007) Macromolecules 40:3361
274. Matsen MW, Thompson RB (2008) Macromolecules 41:1853
275. Kang H, Detcheverry FA, Mangham AN, Stoykovich MP, Daoulas KC, Hamers RJ, Mueller M, de Pablo JJ, Nealey PF (2008) Phys Rev Lett 100:148303
276. Rigler R, Elson E (2001) Fluorescence correlation spectroscopy: theory and applications. Springer series in chemical physics, vol 65. Springer, Heidelberg
277. Haustein E, Schwille P (2004) Curr Opin Struct Biol 14:531

278. Koynov K, Butt HJ (2012) Curr Opin Colloid Interface Sci 17:377
279. Koynov K, Mihov G, Mondeshki M, Moon C, Spiess HW, Müllen K, Butt HJ, Floudas G (2007) Biomacromolecules 8:1745
280. Schmidt M (1993) Dynamic light scattering. In: Brown W (ed) Dynamic light scattering: the method and some applications. Clarendon, Oxford, p 752
281. Whitesides GM, Mathias JP, Seto CT (1991) Science 254:1312
282. Franc G, Gourdon A (2011) Phys Chem Chem Phys 13:14283
283. Gourdon A (2008) Angew Chem Int Ed 47:6950
284. Hla SW, Bartels L, Meyer G, Rieder KH (2000) Phys Rev Lett 85:2777
285. Grill L, Dyer M, Lafferentz L, Persson M, Peters MV, Hecht S (2007) Nat Nanotechnol 2:687
286. Lipton-Duffin JA, Ivasenko O, Perepichka DF, Rosei F (2009) Small 5:592
287. Cai J, Ruffieux P, Jaafar R, Bieri M, Braun T, Blankenburg S, Muoth M, Seitsonen AP, Saleh M, Feng X, Müllen K, Fasel R (2010) Nature 466:470
288. Weigelt S, Busse C, Bombis C, Knudsen MM, Gothelf KV, Laegsgaard E, Besenbacher F, Linderoth TR (2008) Angew Chem Int Ed 47:4406
289. Rahe P, Kittelmann M, Neff JL, Nimmrich M, Reichling M, Maass P, Kühnle A (2013) Adv Mater 25:3948
290. Kittelmann M, Rahe P, Nimmrich M, Hauke CM, Gourdon A, Kühnle A (2011) ACS Nano 5:8420
291. Kittelmann M, Nimmrich M, Lindner R, Gourdon A, Kühnle A (2013) ACS Nano 7:5614-5620 ACS Nano 7:5614
292. Kunstmann T, Schlarb A, Fendrich M, Wagner T, Moller R, Hoffmann R (2005) Phys Rev B 71:121403
293. Schütte J, Bechstein R, Rohlfing M, Reichling M, Kühnle A (2009) Phys Rev B 80:205421
294. Kittelmann M, Rahe P, Kühnle A (2012) J Phys Condens Matter 24:354007
295. Rahe P, Lindner R, Kittelmann M, Nimmrich M, Kühnle A (2012) Phys Chem Chem Phys 14:6544
296. Duffy DM, Harding JH (2002) J Mater Chem 12:3419
297. Kittelmann M, Rahe P, Gourdon A, Kühnle A (2012) ACS Nano 6:7406
298. Kittelmann M, Nimmrich M, Neff JL, Rahe P, Gren W, Bouju AG, Gourdon A, Kühnle A (2013) J Phys Chem C, submitted
299. Luo Y-R (2007) Comprehensive handbook of chemical bond energies. CRC, Boca Raton
300. Lafferentz L, Eberhardt V, Dri C, Africh C, Comelli G, Esch F, Hecht S, Grill L (2012) Nat Chem 4:215